

Peering into the Heart of Thunderstorm Clouds: Insights from Cloud Radar and Spectral Polarimetry

MSc thesis in Geoscience & Remote Sensing
Ho Yi Lydia Mak

Delft University of Technology

Peering into the Heart of Thunderstorm Clouds: Insights from Cloud Radar and Spectral Polarimetry

by

Ho Yi Lydia Mak

Student number: 5540453
Project duration: November, 2022 - July, 2023
Thesis committee: Ir. Christine Unal TU Delft, Supervisor
Dr. Marc Schleiss TU Delft
Dr. Franziska Glassmeier TU Delft
Dr. José Dias Neto TU Delft

Abstract

Lightning is a natural phenomena that can be dangerous to humans. It is however challenging to study thunderstorm clouds using direct observations since it can be dangerous to fly into thunderstorm clouds. In this study, cloud radar with millimeter wavelength is used to study the properties and dynamics of thunderstorm clouds. It is based on a case of thunderstorm on 2021-06-18 from 16:10 to 17:45 UTC near Cabauw. Polarimetric radar variables are used to investigate possible hydrometeors in the clouds and look for vertical alignment of ice crystals that is expected due to electric torque. The technique of Doppler spectra analysis, which has not been used in previous studies about thunderstorms so far, is used to help understand the behaviours of different types of particles within a radar resolution volume. Due to challenges posed by Mie scattering, scattering simulations are carried out to aid the interpretation of spectral polarimetric variables. From the results, there is a high chance that supercooled liquid water and conical graupel are present in thunderstorm clouds. There is also a possibility of ice crystals arranged in chains at the cloud top. Ice crystals become vertically aligned a few seconds before lightning and return to their usual horizontal alignment afterwards. However, this phenomenon has been witnessed in only a few cases, specifically when the lightning strike is in close proximity to the radar's line of sight or when the lightning is exceptionally strong. Doppler analyses show that updrafts are found near the core of the thunderstorm cloud, while downdrafts are observed at the edges. Strong turbulence is also observed as reflected by the large Doppler spectrum width.

Nomenclature

α	Euler angle α ($^{\circ}$)
β	Euler angle β ($^{\circ}$)
δ_{co}	Differential backscatter phase ($^{\circ}$)
$\overline{v_D}$	Mean Doppler velocity (m s^{-1})
ϕ	Radar azimuth angle relative to North ($^{\circ}$)
Φ_{DP}	Differential propagation phase ($^{\circ}$)
Φ_{hh}	Propagation phase shift at horizontal polarization ($^{\circ}$)
Φ_{vv}	Propagation phase shift at vertical polarization ($^{\circ}$)
Ψ_{DP}	Differential phase shift ($^{\circ}$)
ρ_{hv}	Co-polar correlation coefficient (-)
σ	Root mean square error
σ_{vD}	Doppler spectrum width (m s^{-1})
θ	Radar elevation angle ($^{\circ}$)
ε_{eff}	Complex effective relative permittivity of scatterer (-)
ε_i	Complex relative permittivity of ice (-)
C_{wr}	Radar constant ($\text{W m}^5 \text{ mm}^{-6}$)
D	Wind direction relative to North ($^{\circ}$)
E	Electric field (V m^{-1})
f_i	Ice fraction (-)
K_{DP}	Specific differential phase ($^{\circ}/\text{km}$)
l_{DR} / L_{DR}	Linear depolarisation ratio (- / dB)
m_{eff}	Complex effective refractive index of scatterer (-)
P_r	Power received by radar (W)
r	Range (m)
s	Vertical gradient of horizontal wind speed ($\text{m s}^{-1} \text{ m}^{-1}$)
$s\Psi_{DP}$	Spectral differential phase shift ($^{\circ}$)
$S_{hh}; S_{vh}$	First column of the 2×2 scattering matrix, Equation 1.4
$S_{hv}; S_{vv}$	Second column of the 2×2 scattering matrix, Equation 1.4
SL_{DR}	Slant linear depolarisation ratio (dB)
sZ_{DR}	Spectral differential reflectivity (dB)

v_D	Doppler velocity (m s^{-1})
V_f	Particle fall velocity (m s^{-1})
V_h	Particle horizontal velocity (m s^{-1})
v_H	Horizontal wind speed (m s^{-1})
V_t	Particle terminal velocity (m s^{-1})
v_U	Eastward wind speed (m s^{-1})
V_v	Particle vertical velocity (m s^{-1})
v_V	Northward wind speed (m s^{-1})
w	Vertical wind speed (m s^{-1})
z_e / Z_e	Equivalent reflectivity factor ($\text{mm}^6 \text{ m}^{-3} / \text{dBZ}$)
z_{DR} / Z_{DR}	Differential reflectivity ($- / \text{dB}$)
z_{hh}	Equivalent reflectivity factor at horizontal polarization ($\text{mm}^6 \text{ m}^{-3}$)
z_{vv}	Equivalent reflectivity factor at vertical polarization ($\text{mm}^6 \text{ m}^{-3}$)

Contents

Abstract	i
Nomenclature	ii
1 Introduction	1
1.1 Research questions	1
1.2 Background knowledge	2
1.2.1 Rayleigh and Mie scattering	2
1.2.2 Radar variables	3
2 Literature review	5
2.1 Lightning mechanism	5
2.2 Hydrometeors in thunderstorm clouds	5
2.3 Alignment of ice crystals	8
2.4 Updraft characteristics	9
3 Instruments and data	10
3.1 Cloud radar	10
3.2 Radar variables	11
3.3 Weather data	11
4 Thunderstorm events	12
4.1 Thunderstorm event selection	12
4.2 Case study description	13
5 Methodology	22
5.1 Polarimetric variables calculation	22
5.2 Polarimetric calibration	23
5.2.1 Z_{DR} calibration	23
5.2.2 Ψ_{DP} calibration	24
5.3 Specific differential phase shift calculation	24
5.4 Variables from Doppler measurement	24
5.5 Analysing integrated variables	25
5.6 Analysing Doppler spectrum	25
5.7 Scattering simulations	27
6 Calibration results	28
6.1 Z_{DR} calibration	28
6.2 Ψ_{DP} calibration	29
6.3 Evaluation	30
6.4 Specific differential phase shift calculation	33
7 Scattering simulation results	35
7.1 Axis ratio	35
7.2 Ice fraction	36
7.3 Canting angle	37
7.4 Summary	38
8 Case analysis	39
8.1 First cloud	41
8.1.1 Alignment of particles	41
8.1.2 Supercooled liquid water	46
8.1.3 Updrafts and downdrafts	47

8.2	Fourth cloud	47
8.2.1	Evidence of graupel	50
8.2.2	Alignment of particles	53
8.2.3	Strong updraft and turbulence	55
8.2.4	Possibility of chains	57
9	Conclusion	59
9.1	Polarimetric calibration	59
9.2	Hydrometeors in thunderstorm clouds.	59
9.3	Alignment of ice crystals in thunderstorm clouds	59
9.4	Updraft and downdraft pattern in thunderstorm clouds	60
9.5	Time and distance of detectable signatures.	60
9.6	Appropriate measurement modes for studying thunderstorms.	60
9.7	Recommendations	60
	Bibliography	62
	Appendix	65
A	Thunderstorm event list	65
B	Lightning maps	66
C	Other notable cases	71
C.1	Second cloud	71

Introduction

Lightning is a natural phenomena that is dangerous to humans. Scientists began investigating atmospheric electrification and lightning several hundred years ago. Over the years, numerous charging mechanisms were proposed to account for charge separation in thunderstorm clouds. The most widely accepted theory is non-inductive charging, which involves the collisions of ice crystals with riming graupel pellet [1] (see Section 2.1 for more details). More than half a century ago, scientists started using weather radar to study the relationship between radar reflectivity and lightning rate [2]. In recent decades, polarimetric radar variables that provide information about the size and shape of hydrometeors were used to extend our understanding of thunderstorm clouds. More descriptions about these polarimetric radar variables can be found in Section 3.2. However, most research make use of S-band (2-4 GHz), C-band (4-8 GHz) and X-band (9-12 GHz) radar, while limited studies were conducted using cloud radar with millimeter wavelength. Radars at lower frequencies are common choices for investigating thunderstorms as they have larger ranges and suffer from less attenuation, but high frequency cloud radars could bring new insights given their higher spatial resolution. Moreover, existing studies have only analysed integrated radar variables that include the contribution of all particles within each radar resolution volume. There have been no attempts to utilise the Doppler spectra to disentangle the contributions of different types of particles. This study explores new ways to study thunderstorm events by using cloud radar observations and Doppler spectra. The goal is to establish links between radar observations and physical processes in thunderstorms to enhance our understanding about lightning.

1.1. Research questions

The focus of this research is to understand the evolution of thunderstorm clouds before, during and after lightning through a case study. Based on the non-inductive charging theory, it is expected that during lightning, ice crystals, graupel and supercooled liquid water can be found, ice crystals are aligned, and strong updraft is present. Therefore, we would like to analyse how these conditions change across a thunderstorm event.

The first research question is thus: From the polarimetric measurements of 35/94 GHz cloud radar and atmospheric profiles, what can be deduced about

- the hydrometeors present,
- the alignment of ice crystals, and
- the updraft/downdraft pattern

before, during and after lightning?

The second research question is: How long before and how far away from the lightning can signatures of lightning be detected by cloud radar?

Currently, there is no measurement campaign designed specifically for studying thunderstorms, thus the data available might not be sufficient or optimum for our investigation. Therefore, the third research

question is: Which measurement mode(s) is/are the most appropriate for studying signals related to thunderstorms?

1.2. Background knowledge

This research is based on backscattered radar signals measured by cloud radars. The following sections provides background information about scattering processes and radar variables.

1.2.1. Rayleigh and Mie scattering

When electromagnetic wave is incident on a scatterer, Rayleigh or Mie scattering can occur depending on the size of the scatterer relative to the wavelength. For spherical hydrometeors, Rayleigh scattering occurs when their diameters are less than approximately one-fourth of the wavelength of the incident electromagnetic wave [3], which is about 2.1 mm at 35 GHz or 0.8 mm at 94 GHz. In the Rayleigh scattering regime, the radar cross-section is proportional to the sixth power of the diameter, which means that backscattering power increases monotonically with particle size. However, when particle size increases, Mie scattering will occur, and the backscattering power will oscillate with increasing particle size as shown in Figure 1.1.

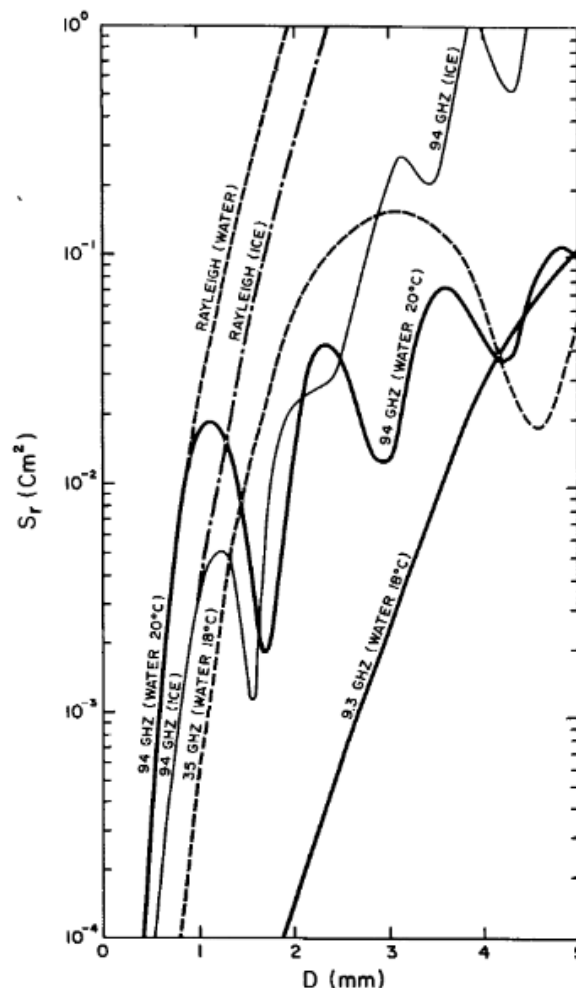


Figure 1.1: Backscattering cross-section of spherical hydrometeors as a function of their diameter at different frequencies taken from [3]

1.2.2. Radar variables

A cloud radar can provide a variety of radar variables that can probe different characteristics of the particles in the atmosphere. The following subsections will introduce the variables relevant to this study.

Equivalent reflectivity factor

Equivalent reflectivity factor z_e is defined as

$$z_e = \frac{P_r r^2}{C_{wr}}, \quad (1.1)$$

where P_r is the received power in W, r is the range in m, C_{wr} is the radar constant in $\text{W m}^5 \text{mm}^{-6}$ and the unit of z_e is $\text{mm}^6 \text{m}^{-3}$. It increases with increasing number concentration and size of scattering particles. Since the size of hydrometeors can vary over many orders of magnitude, the equivalent reflectivity factor is often expressed in decibels:

$$Z_e = 10 \log_{10} z_e \quad (1.2)$$

Here, the units of Z_e and z_e are dBZ and $\text{mm}^6 \text{m}^{-3}$ respectively. In general, Z_e measured by radar is obtained from emitting and receiving horizontal polarized waves, thus it is equivalent to Z_{hh} , the equivalent reflectivity factor at horizontal polarization. Note that capitalised radar variables denote values expressed in decibels, while lowercase variables denote values in linear scale.

Differential reflectivity

Differential reflectivity z_{DR} is defined as

$$z_{DR} = \frac{\langle |S_{hh}|^2 \rangle}{\langle |S_{vv}|^2 \rangle} = \frac{z_{hh}}{z_{vv}}. \quad (1.3)$$

z_{hh} and z_{vv} (in $\text{mm}^6 \text{m}^{-3}$) are the equivalent reflectivity factors at horizontal and vertical polarization respectively. S_{hh} and S_{vv} are terms from the scattering matrix defined by

$$\begin{bmatrix} E_h^s \\ E_v^s \end{bmatrix} = \begin{bmatrix} S_{hh} & S_{hv} \\ S_{vh} & S_{vv} \end{bmatrix} \begin{bmatrix} E_h^i \\ E_v^i \end{bmatrix}, \quad (1.4)$$

where E is the electric field, superscripts s and i stand for scattered and incident waves respectively, and h and v stand for horizontal and vertical polarizations respectively.

Differential reflectivity is often expressed in dB:

$$Z_{DR} = 10 \log_{10}(z_{DR}) = 10 \log_{10}(z_{hh}) - 10 \log_{10}(z_{vv}) = Z_{hh} - Z_{vv}. \quad (1.5)$$

Z_{DR} is affected by the shape and permittivity of the targets. For Rayleigh scatterers, Z_{DR} is positive if the major axis is aligned in the horizontal direction, and negative if the major axis is aligned in the vertical plane. Z_{DR} of spherical particles is 0 dB. Since the permittivity of water is larger than that of ice, water particles give enhanced Z_{DR} compared to ice particles with the same size and shape. Z_{DR} of ice particles with lower density is further diminished. It should also be noted that Z_{DR} is reflectivity-weighted, which means that if there are more than one type of hydrometeors in a radar resolution volume, Z_{DR} values would be biased towards that of the larger particles.

Linear depolarisation ratio

Linear depolarisation ratio (l_{DR}) is defined as

$$l_{DR} = \frac{\langle |S_{vh}|^2 \rangle}{\langle |S_{hh}|^2 \rangle} = \frac{z_{vh}}{z_{hh}}. \quad (1.6)$$

It is often expressed in dB:

$$L_{DR} = 10 \log_{10}(l_{DR}) = 10 \log_{10}(z_{vh}) - 10 \log_{10}(z_{hh}) = Z_{vh} - Z_{hh}. \quad (1.7)$$

L_{DR} depends on the permittivity, orientation and shape of scatterers. In particular, it increases with the variance in canting angle of the scatterers in a radar resolution volume. High L_{DR} values may indicate vertical alignment of ice crystals due to cloud electrification [4].

Co-polar correlation coefficient

Co-polar correlation coefficient (ρ_{hv}) is a variable that can indicate the diversity in the types, shapes, and/or orientations of the particles in a radar resolution volume. A value close to 1 indicates a homogeneous medium, while lower values would suggest a mixture of hydrometeors. The definition of ρ_{hv} is

$$|\rho_{hv}| = \left| \frac{\langle S_{hh}^* S_{vv} \rangle}{\sqrt{\langle |S_{hh}|^2 \rangle \langle |S_{vv}|^2 \rangle}} \right| \quad (1.8)$$

Differential phase shift and specific differential phase

Differential phase shift (Ψ_{DP}) is the sum of the two-way differential propagation phase (Φ_{DP}) and the differential backscatter phase (δ_{co}). Differential propagation phase arises as electromagnetic waves in horizontal and vertical polarizations acquire different amounts of phase shift when propagating through non-spherical hydrometeors. It is given by

$$\Phi_{DP} = 2(\Phi_{hh} - \Phi_{vv}), \quad (1.9)$$

where Φ_{hh} and Φ_{vv} are the propagation phase shifts at horizontal and vertical polarizations respectively. The phase shifts are commonly given in degrees. δ_{co} is zero in the Rayleigh scattering regime and non-zero in the Mie scattering regime.

A useful variable that can be derived from differential propagation phase is the specific differential phase (K_{DP}), which is defined by

$$\Phi_{DP} \equiv 2K_{DP}r. \quad (1.10)$$

The common unit of K_{DP} is degrees/km. K_{DP} is inversely proportional to wavelength, thus the values are larger at 94 GHz than at 35 GHz. Similar to Z_{DR} , K_{DP} is positive when the major axis of the particle is aligned in the horizontal direction, and negative if the major axis is aligned in the vertical plane. However, unlike Z_{DR} , K_{DP} is not reflectivity-weighted, but increases with the number concentration of particles. Also, K_{DP} represents non-spherical particles only. Therefore, if there are large spherical particles and small oblate particles in a radar resolution volume, the K_{DP} measurement will provide information on the small oblate particles only, giving positive or negative K_{DP} while Z_{DR} is nearly 0 dB.

2

Literature review

In this chapter, literature related to characteristics of thunderstorms and observations of thunderstorms using radar is reviewed. First, general information about thunderstorms and how they are formed are discussed in Section 2.1. Then, Section 2.2 gives an overview of the different types of hydrometeors that may be present in thunderstorm clouds. Section 2.3 discusses the alignment of ice crystals in electric fields and previous studies about this phenomenon using radar. Finally, Section 2.4 highlights the importance of updrafts in thunderstorm clouds.

2.1. Lightning mechanism

Lightning is the electric discharge caused by an electrical breakdown of charges built up in a cloud. Many studies have shown that the charge distribution in most thunderclouds follow a tripole structure, with positive charges in the upper and lower levels and negative charges in the middle level [5]. The positive charge center near the cloud base is relatively small, thus is sometimes ignored. Typically, a breakdown can occur when the environmental electric field established by the charges is around $100\text{-}300\text{ V m}^{-1}$, though the critical field at the point of breakdown is likely much higher [5]. During a thunderstorm, the electric field builds up and breaks down continuously. The time needed to accumulate large enough electric fields for lightning to occur ranges from less than a minute to several minutes [6, 7]. For active thunderstorm clouds with tens of kV m^{-1} in the interior, the magnitude of the electric field decreases to 3 kV m^{-1} within 5 km away from the cloud edge on average [8].

Multiple mechanisms have been suggested to explain how such large electric field is set up in thunderclouds. The most widely accepted mechanism is the non-inductive charging theory. The non-inductive charging theory involves the collisions of ice crystals with riming graupel pellet, which was first studied in the laboratory by Reynolds et al. [1]. They found that graupel pellets that are growing by the accretion of supercooled droplets acquires negative charges as they collide with ice crystals. Takahashi [9] further investigated this phenomenon and found that the magnitude and sign of the electrification depend largely on temperature and cloud water content. The optimal cloud water content for graupel to become highly charged is $1\text{-}2\text{ g m}^{-3}$, and they will become positively charged if the temperature is above -10°C and negatively charged otherwise [9]. Within the updraft column in a thundercloud where temperature is low, negatively charged graupel and positively charged ice crystals will be formed. The negatively charged graupel will fall at the periphery of the column where the updraft is weak, while the positively charged ice crystals will be thrown upwards. As the graupel reach a region warmer than -10°C , they become positively charged. This explains the tripole structure of most thunderclouds.

2.2. Hydrometeors in thunderstorm clouds

A wide variety of ice particles can be found in the atmosphere. Bailey and Hallett [10] derived a comprehensive ice crystal habit diagram (Figure 2.1) based on laboratory experiments and in situ observations. Plates are formed from 0 to -4°C , columns are formed from -4 to -8°C , and plates are also formed from -8 to -22°C . Polycrystals are formed at lower temperatures, with platelike crystals from -20 to -40°C and columnar crystals from -40 to -70°C .

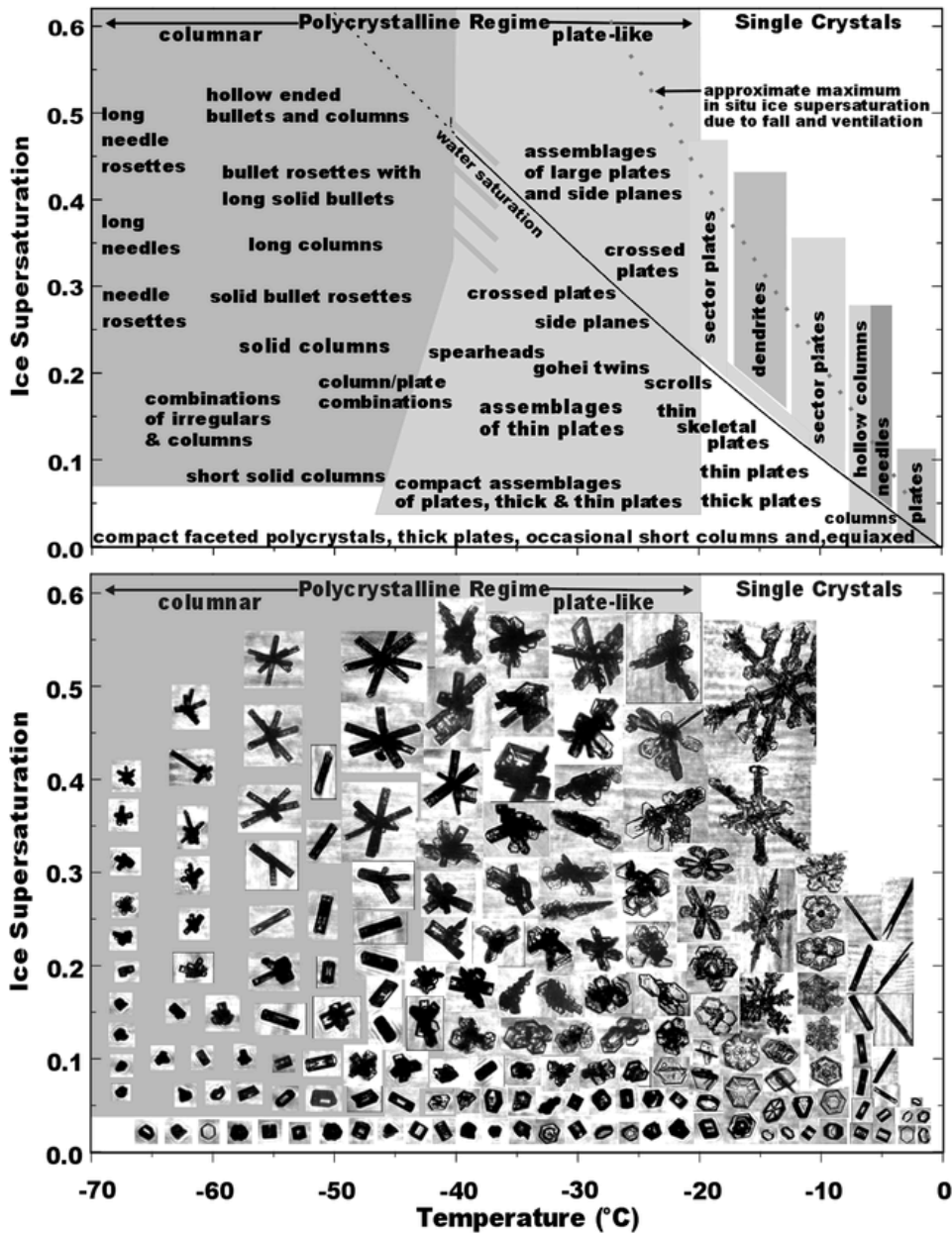


Figure 2.1: Ice crystal habit diagram taken from [10]

Ice crystals can grow within clouds through three major processes [11, 12]: riming, water vapor diffusional growth and aggregation. Riming occurs when supercooled water droplets collide with ice crystals and freeze on them, forming large, dense and near spherical particles. Conical graupel (Figure 2.2) can be formed if riming occurs while particles fall through strong updrafts containing water droplets. Since the bottom windward side of the particle grows faster than the top leeward side, the particle develops a conical shape [13]. Scattering simulations carried out by Oue et al. [14] and Lu et al. [15] showed that conical graupel can produce negative Z_{DR} values at X-, Ka- and W-band. Figure 2.3 shows the simulated differential reflectivity of conical graupel with density 0.55 g cm^{-3} versus equal-volume-sphere radius at Ka- and W-band from the polarimetric scattering database of [15]. The axis ratios of the graupel, defined as the ratio of the maximum vertical dimension to maximum horizontal dimension, are 1.83, 1.44, 1.19, 1.02, 0.89 and 0.79 respectively for cone angles ranging from 30° to 80° in 10° increments. A laboratory study has shown that cone angles of conical graupel are larger when the relative velocity between the graupel and water droplets that collide and rim on them increases, or when the droplet median volume diameter is larger, or when surface temperature is lower [16]. From Figure 2.3, differ-

ential reflectivity is negative in the Rayleigh scattering regime when the cone angle is less than 50° . The fluctuations in Z_{DR} values for large particle sizes are due to Mie scattering.

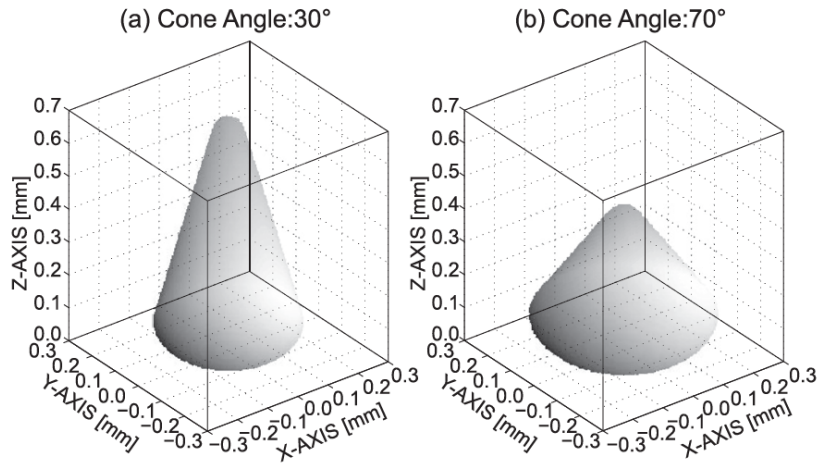


Figure 2.2: Examples of modelled conical graupel taken from [14]

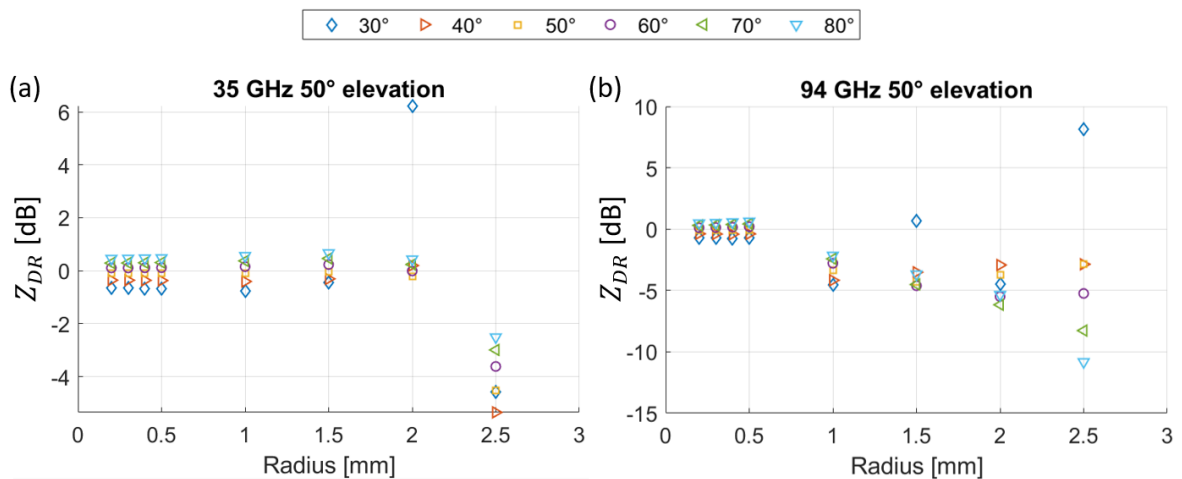


Figure 2.3: Simulated differential reflectivity of conical graupel with density 0.55 g cm^{-3} versus equal-volume-sphere radius at (a) 35 GHz and (b) 94 GHz for 50° elevation angle from polarimetric scattering database of Lu et al. [15]. The different symbols denote different cone angles for the conical graupel

Diffusional growth takes place when water vapor diffuses towards ice crystals from gas phase. During this process, crystals keep their characteristic shape [12].

Aggregation occurs when ice crystals collide with each other and form larger crystals that are more spherical in shape. When an electric field of more than 50 kV m^{-1} is present, aggregation of ice crystals may be enhanced due to attractive electrical forces induced between neighbouring conducting crystals [17], forming elongated chains rather than spherical clusters. Figure 2.4(a) shows some examples of plate crystals arranged into chains in anvil clouds, i.e. the region of convective cloud detraining from the main cell of the thunderstorm cloud, captured by a cloud particle imager taken by [17] at an altitude of around 12 km where the temperature is below -40°C . Chain-like aggregates can also be formed from frozen droplets, such as those observed by Gayet et al. [18] near the top of an overshooting convective cloud at 11080 m where the temperature is -58°C as shown in Figure 2.4(b). The enhancement of aggregation starts to decrease when the electric field exceeds 150 kV m^{-1} since the strong electric field would fragment the ice particle [17]. Meanwhile, laboratory experiments have found that electric

field enhanced aggregation does not occur when ice particle number concentration is below 2 cm^{-3} [19]. High concentration of ice particles could be present in convective clouds if strong updrafts carry supercooled droplets to a level of -37°C where they freeze rapidly by the process of homogeneous nucleation [18].

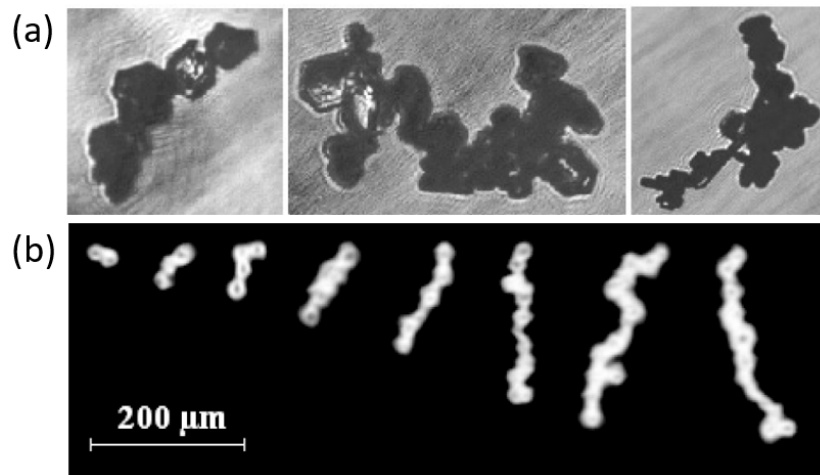


Figure 2.4: Examples of (a) plate crystals arranged into chains in anvil clouds taken from [17] (chain lengths from left to right are 381, 632 and 721 μm respectively) and (b) frozen drops arranged into chains near the top of an overshooting convective cloud taken from [18]

According to the non-inductive charging theory, the separation of charges within thunderclouds require the presence of graupel and ice crystals. Some studies found evidence of this using polarimetric and Doppler measurements.

Mattos et al. [20] used X-band radar to compare storms with and without lightning activities and analysed the vertical distribution of hydrometeors within thunderclouds. They found that in the lower layer of thunderclouds (from 0 to -15°C), there is an enhanced positive K_{DP} probably associated with supercooled oblate raindrops lofted by updraft; in the middle layer (from -15 to -40°C), there is negative Z_{DR} and K_{DP} and moderate horizontal reflectivity, which are possibly associated with the presence of conical graupel; in the upper layer (above -40°C), K_{DP} becomes more negative with increasing lightning density, which suggests vertical alignment of ice particles by the cloud electric field. With Ka-band cloud radar, Sokol et al. [4] identified a mixture of hydrometeors at an elevation of 4–7 km with a predominance of ice and snow particles and graupel based on the terminal velocities of different hydrometeors. The coexistence of different types of hydrometeors is supported by the high Doppler spectrum width, which also implies the existence of collisions of hydrometeors.

2.3. Alignment of ice crystals

The alignment of ice crystals under strong electric field in thunderstorm clouds was first suggested by Vonnegut [21] based on changes in cloud brightness observed during lightning. Weinheimer and Few [22] studied the magnitude of electric field needed to align particles of different sizes and shapes. They compared the magnitudes of electrical torques that try to align particles' long axis with the electric field, and aerodynamic torques that attempt to align particles with their long axes perpendicular to their direction of motion. They estimated that for an electric field of 100 kV m^{-1} , plates with a major dimension of less than 0.6 mm can be aligned, while the threshold is 1 mm for dendrites and 0.2 mm for thick plates. Columns of all sizes can be aligned by such a field. Meanwhile, only particles smaller than 0.05 mm can be aligned by an electric field of 10 kV m^{-1} .

The alignment of ice crystals during thunderstorms is observed in various case studies using polarimetric radar measurements. For example, Lund et al. [23] observed negative Z_{DR} in or near clusters of lightning initiations using S-band radar, which is likely due to ice particles being aligned vertically by a large vertical electric field. Also using S-band radar, Melnikov et al. [24] compared polarimetric

radar measurements obtained using simultaneous H/V mode and alternative H/V mode. In simultaneous H/V mode, areas with canted crystals show well-pronounced negative K_{DP} but featureless ρ_{hv} . In alternative H/V mode, areas with canted crystals show high L_{DR} and cross-polar correlation coefficient ρ_{xh} , as well as uniform differential phase Φ_{XP} defined as $\Phi_{XP} = \arg(\langle S_{hh}^* S_{vh} \rangle)$, where S_{hh} and S_{vh} are elements of the scattering matrix in Equation 1.4. All these variables are more sensitive to canted crystals than those obtained using simultaneous H/V mode. Meanwhile, only one study that used cloud radar to study the alignment of ice crystals during thunderstorms is found. Using a Ka-band radar, Sokol et al. [4] observed high L_{DR} in clouds that produce lightning in the vicinity, which is likely caused by the alignment of ice crystals in an electric field.

Other causes of ice particle alignment are also studied in the literature. Cho et al. [25] found that turbulence is unable to destroy the preferred orientation of falling ice crystals in cumulonimbus clouds. Brussaard [26] derived the canting angle of particles due to vertical wind shear, i.e. difference in horizontal wind speed in vertical direction, by assuming that the mean orientation of their rotational symmetric axes are always parallel to the direction of the airflow around them. If there is no updraft and the particle is falling at its terminal velocity, for a linear wind profile, the canting angle (γ) of the particle is given by

$$\tan \gamma = -\frac{sV_t}{g} \quad (2.1)$$

where $s = \frac{dv_H}{dz}$ is the vertical gradient of horizontal wind speed, V_t is the terminal velocity of the particle that depends on its size, and g is the gravitational acceleration.

2.4. Updraft characteristics

Lightning frequency is highly dependent on updraft speed. Using a simple one-dimensional model, Baker et al. [27] showed that lightning frequency f (s^{-1}) can be written as

$$f \approx R w^6 \bar{V}_i, \quad (2.2)$$

where R (m) is the cloud radius, w (m s^{-1}) is the updraft speed, and \bar{V}_i (m^3) is the volume of ice in the cloud. The sixth power of w shows that strong updraft is crucial in producing frequent lightning. According to Zipser and Lutz [28], lightning is highly unlikely if the mean updraft speed is less than around $6\text{-}7 \text{ m s}^{-1}$, or the peak updraft speed is less than around $10\text{-}12 \text{ m s}^{-1}$. It is common to find updrafts of more than 10 m s^{-1} and up to 30 m s^{-1} in thunderstorms [29, 30].

Several studies have investigated how updraft volume and location associate with lightning activities. Using dual-polarimetric Doppler radar data from S-band radar, Deierling et al. [31] performed hydrometeor classification and 3D wind field estimation in thunderstorm clouds and found that lightning frequency is proportional to the downward mass flux of solid precipitation (i.e. graupel) and upward mass flux of ice crystals. In another study [32] using S-band dual Doppler radar data, it was found that the volume of charged regions with temperatures lower than -5°C and vertical velocities larger than 5 or 10 m s^{-1} correlates well with total lightning activity. In a case study conducted by Lund et al. [23] using S-band polarimetric radar and C-band dual-Doppler radar, the evolution of a thunderstorm was investigated in detail. It was found that during the initial stage of lightning activity, lightning is initiated just outside the strongest updrafts and near the boundary of mixed hydrometeors. On the other hand, during the weakening stage, lightning is initiated mainly in the lower level near the boundary of regions that probably contained graupel before.

3

Instruments and data

This chapter gives an overview of the instruments and data available for this study. Section 3.1 introduces the cloud radars available, then Section 3.2 and Section 3.3 describe the radar variables and weather data provided by the radars respectively.

3.1. Cloud radar

There are three cloud radars available in the Netherlands. The first one located at Cabauw (51.968°N 4.929°E) is a dual-frequency scanning polarimetric frequency-modulated continuous-wave (FMCW) radar by Radiometer Physics GmbH. It emits and measures electromagnetic waves at 35 GHz (Ka-band) and 94 GHz (W-band). The other two cloud radars only operate at 94 GHz. One is located at Lutfjewad (53.404°N 6.353°E), while the other is based in Delft (51.996°N 4.379°E), but was occasionally moved to Cabauw and Rotterdam (51.912°N 4.470°E) for campaigns. A photo of the Cabauw radar is shown in Figure 3.1.

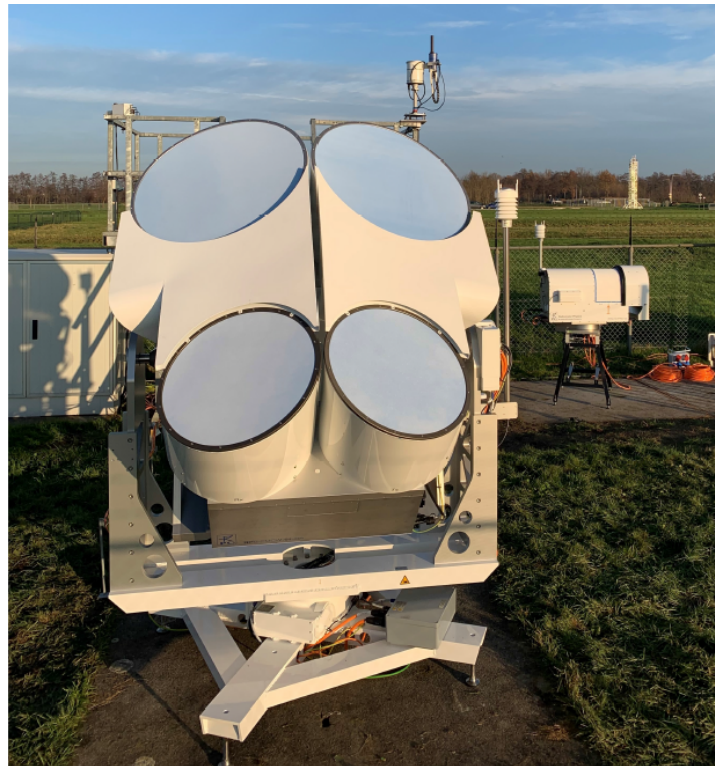


Figure 3.1: Dual-frequency scanning polarimetric frequency-modulated continuous-wave (FMCW) cloud radar at Cabauw

All three radars operate in Simultaneous Transmission Simultaneous Reception (STSR) mode, which means they transmit horizontal and vertical components of electromagnetic waves simultaneously. The radars can perform different types of measurements, including zenith observation (ZEN), constant elevation and azimuth (CEL), and azimuth scan with constant elevation (PPI). Table 3.1 compares the specifications and settings of the three radars. Each radar has three range intervals, or chirps, that can have different settings for variables such as Doppler velocity resolution, Nyquist velocity and range resolution. The table gives the ranges of these variables for the three chirps, while detailed chirp settings of the radars used in this study are given in Tables 4.1, 4.2 and 4.3.

Table 3.1: Technical specifications and settings of cloud radars

Specifications	Cabauw 35 GHz	Cabauw 94 GHz	Delft 94 GHz	Lutjewad 94 GHz
Half power beam width ($^{\circ}$)	0.84	0.55	0.56	0.56
Doppler velocity resolution (m s^{-1})	0.13-0.17	0.05-0.06	0.02-0.04	0.04-0.07
Nyquist velocity ($\pm \text{m s}^{-1}$)	10.7-19.7	4.0-7.4	5.1-10.2	5.1-10.5
Range resolution (m)	29.8-55.0	29.8-55.0	22.4-37.7	29.8-32.5
Temporal sampling (s)	3.59	3.59	1.06	2.86
Minimum/maximum range (m)	119-14970	119-14970	112-11975	119-9984

3.2. Radar variables

The cloud radars provide two types of output data. The Level 0 dataset contains the raw data, which includes the Doppler spectrum at horizontal and vertical polarizations (sZ_{hh} and sZ_{vv}), as well as the real and imaginary parts of the correlation between horizontal and vertical polarizations ($sC_{hh,vv}$). The Level 1 dataset contains processed data, including the equivalent radar reflectivity factor (Z_e , or Z_{hh}), mean Doppler velocity, spectrum width and skewness, differential reflectivity (Z_{DR}), co-polar correlation coefficient (ρ_{hv}), differential phase shift (Ψ_{DP}), specific differential phase shift (K_{DP}), differential attenuation, and slanted linear depolarization ratio (SL_{DR}). SL_{DR} is a proxy for L_{DR} , which can only be computed when the radar transmits horizontally and vertically polarized electromagnetic waves alternately. Since the radar used in this study transmits them simultaneously, only SL_{DR} is available.

3.3. Weather data

A weather station is attached to the cloud radar to provide weather information such as temperature and relative humidity profiles along the zenith and rain rate. The 35 and 94 GHz radars also have a passive broad band channel operated at a centre frequency of 35 and 89 GHz respectively that provides information about the integrated liquid water path (LWP). The weather station of the radar also provides surface wind speed and wind direction, but does not provide the wind profile. Wind profile is obtained instead from European Centre for Medium-Range Weather Forecasting (ECMWF) Integrated Forecast System output over Cabauw [33] available at <https://cloudnet.fmi.fi/>. This model provides hourly forecast of zonal (eastward) and meridional (northward) wind up to 80000 m with a horizontal resolution of 9 km. The vertical resolution of the first 10000 m ranges from around 20 m at the surface to around 300 m at the top.

4

Thunderstorm events

In this chapter, the method to select suitable thunderstorm events for case study is described in Section 4.1. Then, an overview of the selected case is given in Section 4.2.

4.1. Thunderstorm event selection

The first step to gather suitable events is to find out when thunderstorm occurred near the radar locations in Cabauw, Delft and Rotterdam. A first search was carried out using the online database weatherspark.com, which provides a record of hourly observed weather. The search was done from 2021-01-01 to 2022-12-31 for the cities Utrecht, Delft and Rotterdam, which are the nearest cities to the radars where weather history records are available. For hours labeled with ‘thunderstorm’, the online lightning map from meteologix.com was used to locate the lightning strokes. The lightning data from this site is provided by Siemens BLIDS. Clicking on the lightning stroke gives its location, time, type, charge (positive or negative) and power.

Thunderstorm events with lightning within 10 km from the radar were shortlisted. Not all of these thunderstorms were well-captured by the nearest cloud radar with the preferred measurement mode. Therefore, the shortlisted cases were further filtered based on the following criteria:

1. The radar should be present and normally operating during the thunderstorm. The cloud radars stationed at Cabauw and Lutjewad have missing data on some days. The Delft radar was moved to Cabauw and Rotterdam for campaigns, so it did not provide measurements for Delft during those periods. However, when it was moved to Cabauw, it carried out different types of measurement than the radar at Cabauw, thus could provide additional data for analysis.
2. The radar should be looking obliquely so that polarimetric variables can be analysed. Observations of zenith-looking radar, if available, can be used as a supplement to retrieve vertical velocities.
3. The thunderstorm cloud should cross the line of sight of the radar. This criteria was checked against the radar images of the weather radar at Herwijnen.
4. There should not be significant rainfall during the thunderstorm. This is because we are interested in the characteristics of the thunderstorm cloud, but if rainfall rate is high, the cloud radar especially at 94 GHz would suffer from significant attenuation and cannot receive backscatter signals from the cloud. This criteria was checked by plotting the profile of radar reflectivity factor during the event. Events where most parts of the cloud cannot be observed were excluded.

A list of all 36 thunderstorm events found and the properties of the radar that might have recorded them can be found in Appendix A. Priority was given to cases with continuous measurement for the ease of analysis. For the campaign in Rotterdam, the elevation angle of the cloud radar alternated between 30°, 45° and 90° and 85° for PPI.

4.2. Case study description

The case that was chosen for in-depth study is the thunderstorm on 2021-06-18 at around 16:15 to 17:45 UTC near Cabauw. The Delft radar was present at Cabauw in addition to the Cabauw radar during this period. The Cabauw radar was looking with 45° elevation towards the azimuth angle of 282°, while the Delft radar was looking towards the zenith. The configuration parameters of the two radars for each chirp are summarised in Tables 4.1, 4.2 and 4.3.

Table 4.1: Configuration parameters of Cabauw radar at 35 GHz for each chirp sequence

Attributes	1	2	3
Integration time (s)	1.20	0.96	0.82
Range interval (m)	119.2-1192.5	1222.3-4889.1	4953.3-14969.9
Range resolution (m)	29.8	29.8	55.0
Nyquist velocity (\pm m s ⁻¹)	19.7	16.1	10.7
Doppler velocity resolution (m s ⁻¹)	0.15	0.13	0.17

Table 4.2: Configuration parameters of Cabauw radar at 94 GHz for each chirp sequence

Attributes	1	2	3
Integration time (s)	1.20	0.96	0.82
Range interval (m)	119.2-1192.5	1222.3-4889.1	4953.3-14969.9
Range resolution (m)	29.8	29.8	55.0
Nyquist velocity (\pm m s ⁻¹)	7.4	6.0	4.0
Doppler velocity resolution (m s ⁻¹)	0.06	0.05	0.06

Table 4.3: Configuration parameters of Delft radar for each chirp sequence

Attributes	1	2	3
Integration time (s)	0.03	0.14	0.27
Range interval (m)	111.8-581.3	621.0-1999.0	2033.5 - 11974.8
Range resolution (m)	22.4	27.0	37.7
Nyquist velocity (\pm m s ⁻¹)	10.2	7.2	5.1
Doppler velocity resolution (m s ⁻¹)	0.04	0.03	0.02

From 16:15 to 17:45 UTC, four major thunderstorm clouds (numbered in Figure 4.1(a) and Figures 4.5, 4.6 and 4.7) crossed the line of sight of the radar from southwest to northeast. The equivalent reflectivity factor, Z_e , and rain rate from 16:00 to 17:59 UTC are shown in Figure 4.1, while Z_{DR} , K_{DP} , SL_{DR} and ρ_{hv} are shown in Figure 4.2 and Figure 4.3. Note that Z_e , SL_{DR} and ρ_{hv} are taken directly from the Level 1 files, while Z_{DR} and K_{DP} are re-calculated from Level 0 files and calibrated (see Chapter 5).

From Figure 4.1(a), due to significant attenuation, the top part of the second and fourth clouds which produced precipitation that reached the ground are missing at 35 GHz. Larger parts of the clouds are missing at 94 GHz as shown in Figure 4.1(b). The zenith looking radar (Figure 4.1(c)) could not see the first cloud from 16:10 to 16:30 UTC since the cloud was far away from the radar. Some artefacts are observed in all three radars, such as the noise from ground level to 2500 m over the entire period. For the radars looking at 45° elevation, there are also 'ghost' signals between 2500 m and 3500 m at 16:10 to 16:25 UTC and at 17:30 to 17:40 UTC, which are likely due to signals from the top of the cloud being folded into the second chirp. These artefacts are also present in other variables, thus the data in the second chirp might not be reliable. From Figure 4.1, no melting layer with high Z_e is visible although the temperature was about 0°C at around 4000 m, which is likely due to convective mixing.

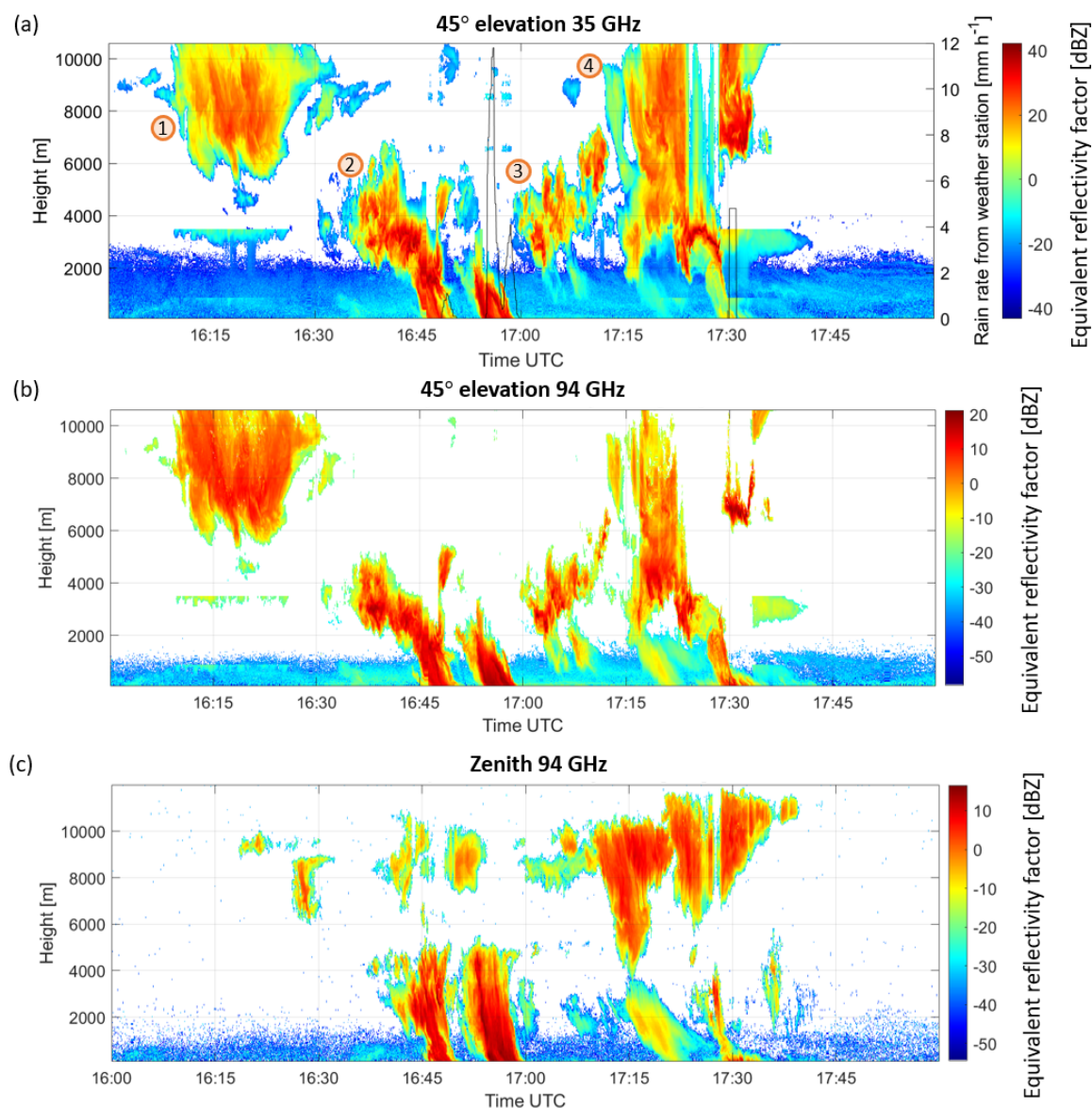


Figure 4.1: Equivalent reflectivity factor on 2021-06-18 16:00 - 17:59 UTC measured by radar at (a) 35 GHz with 45° elevation angle, (b) 94 GHz with 45° elevation angle and (c) 94 GHz looking towards the zenith. Black line in (a) shows the rain rate

From Figure 4.2(a) and Figure 4.3(a), negative Z_{DR} and high SL_{DR} values are observed at 16:42 to 16:48 UTC and 17:24 to 17:30 UTC, which could be associated to the alignment of particles near lightning. Comparing Figure 4.2(a) and (b), Z_{DR} and K_{DP} show different patterns in some areas, such as in the first high cloud and in the top part of the cloud at 17:20 to 17:25 UTC. These will be further investigated. From Figure 4.3(b), low ρ_{hv} values are found also at 16:42 to 16:48 UTC and 17:24 to 17:30 UTC, which suggests that there may be a mixture of hydrometeors in the cloud.

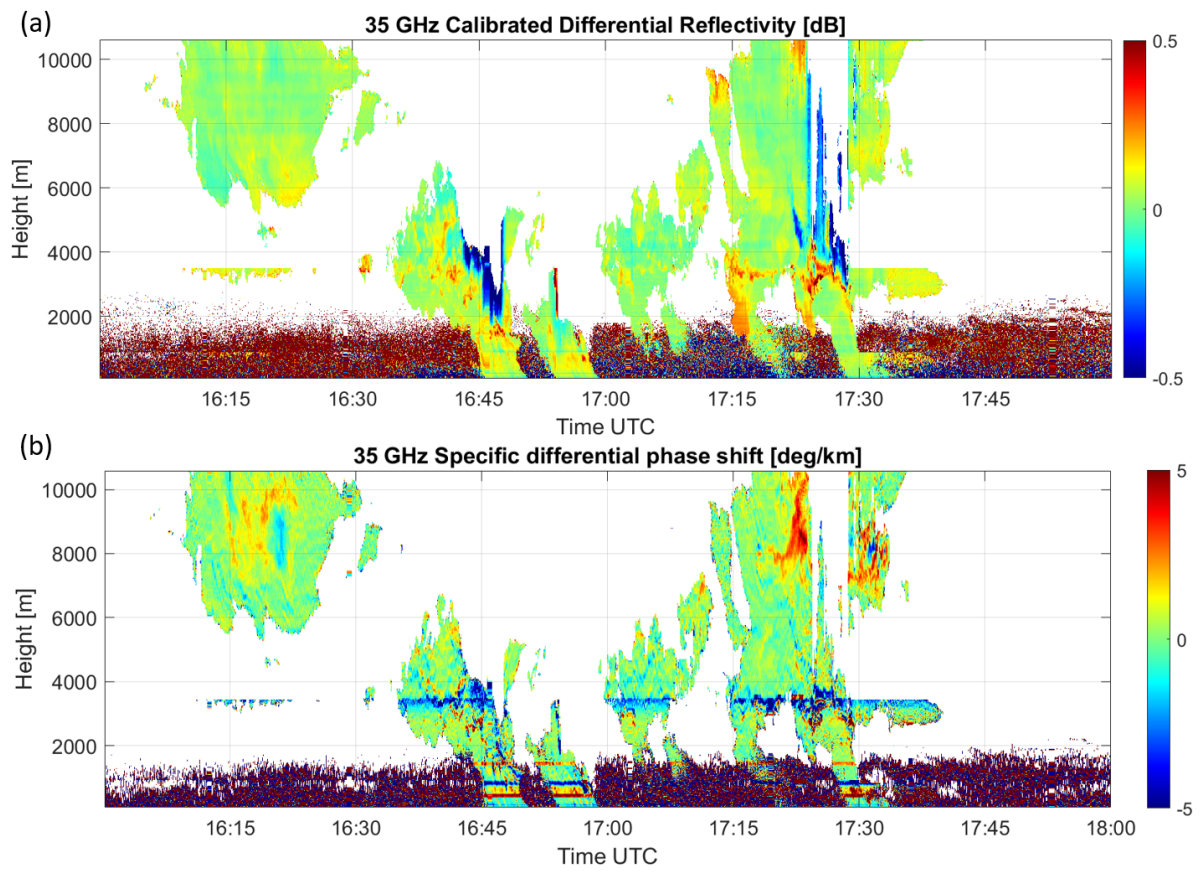


Figure 4.2: (a) Z_{DR} and (b) K_{DP} on 2021-06-18 16:00 - 17:59 UTC at 35 GHz with 45° elevation

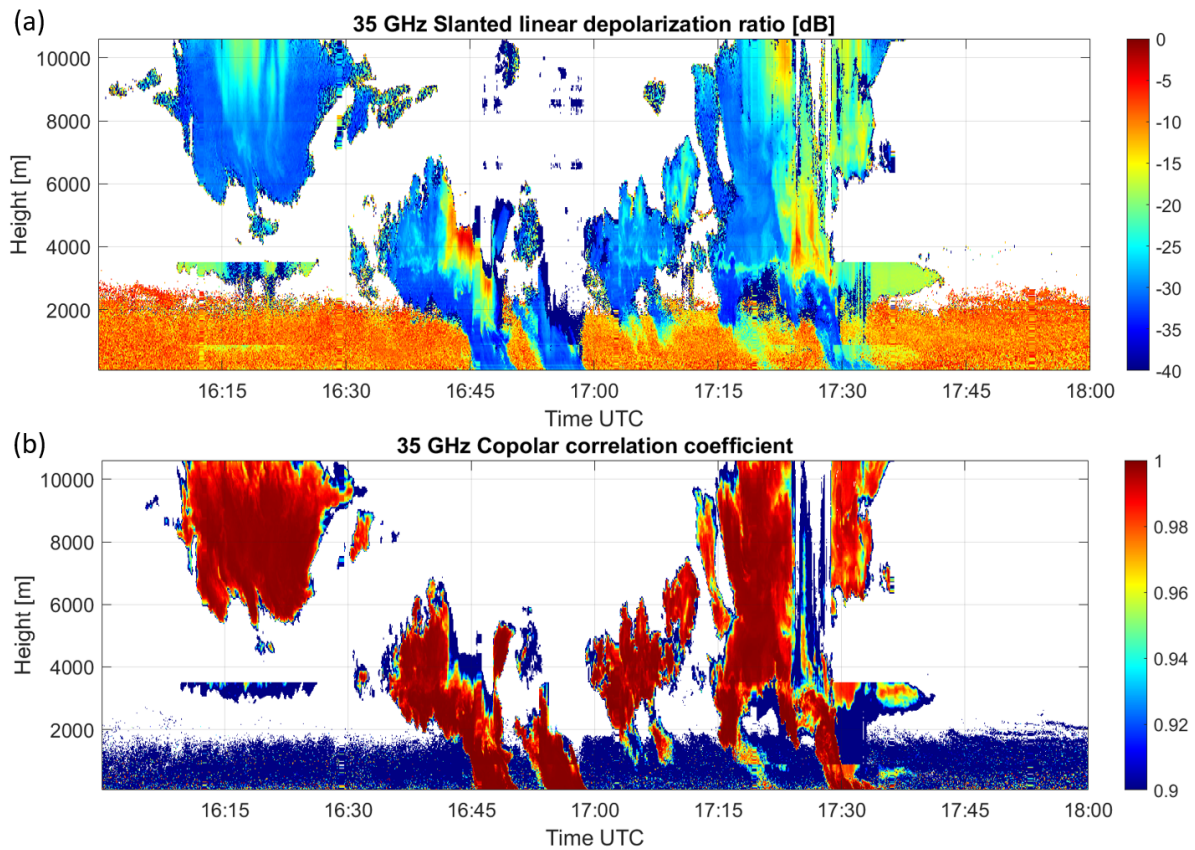


Figure 4.3: (a) SL_{DR} and (b) ρ_{hv} on 2021-06-18 16:00 - 17:59 UTC at 35 GHz with 45° elevation

Figure 4.4 shows the mean Doppler velocity, mean vertical velocity, vertical air velocity and Doppler spectrum width during the thunderstorm. Negative (Positive) Doppler velocities correspond to movement towards (away from) the radar, while negative (positive) vertical velocities correspond to downward (upward) movement. The mean Doppler velocity shown in Figure 4.4(a) reflects the contributions of particle fall velocity as well as horizontal and vertical air velocity along the line of sight of the radar. The mean vertical velocity in Figure 4.4(b) eliminates the contribution of horizontal wind and reflects the mean vertical motion of hydrometeors. In the first cloud from 16:10 to 16:30 UTC, particles are mainly falling, while in the other clouds, there are alternate regions where particles are falling and rising. From Figure 4.4(c), vertical air velocity varies a lot within the clouds. There are regions with upward velocity exceeding 20 m s^{-1} , which shows there may be strong updrafts in the thunderstorm clouds. There are also adjacent regions with upward and downward motion, such as near 16:22 and 17:20 UTC. These may represent convective motion in the clouds. Figure 4.4(d) shows that some regions in the clouds have high Doppler spectrum width, such as within the first cloud and near the top of the fourth cloud. This could mean that there is a wide variety of particles within the radar resolution volume or the Doppler spectrum is broadened by turbulence.

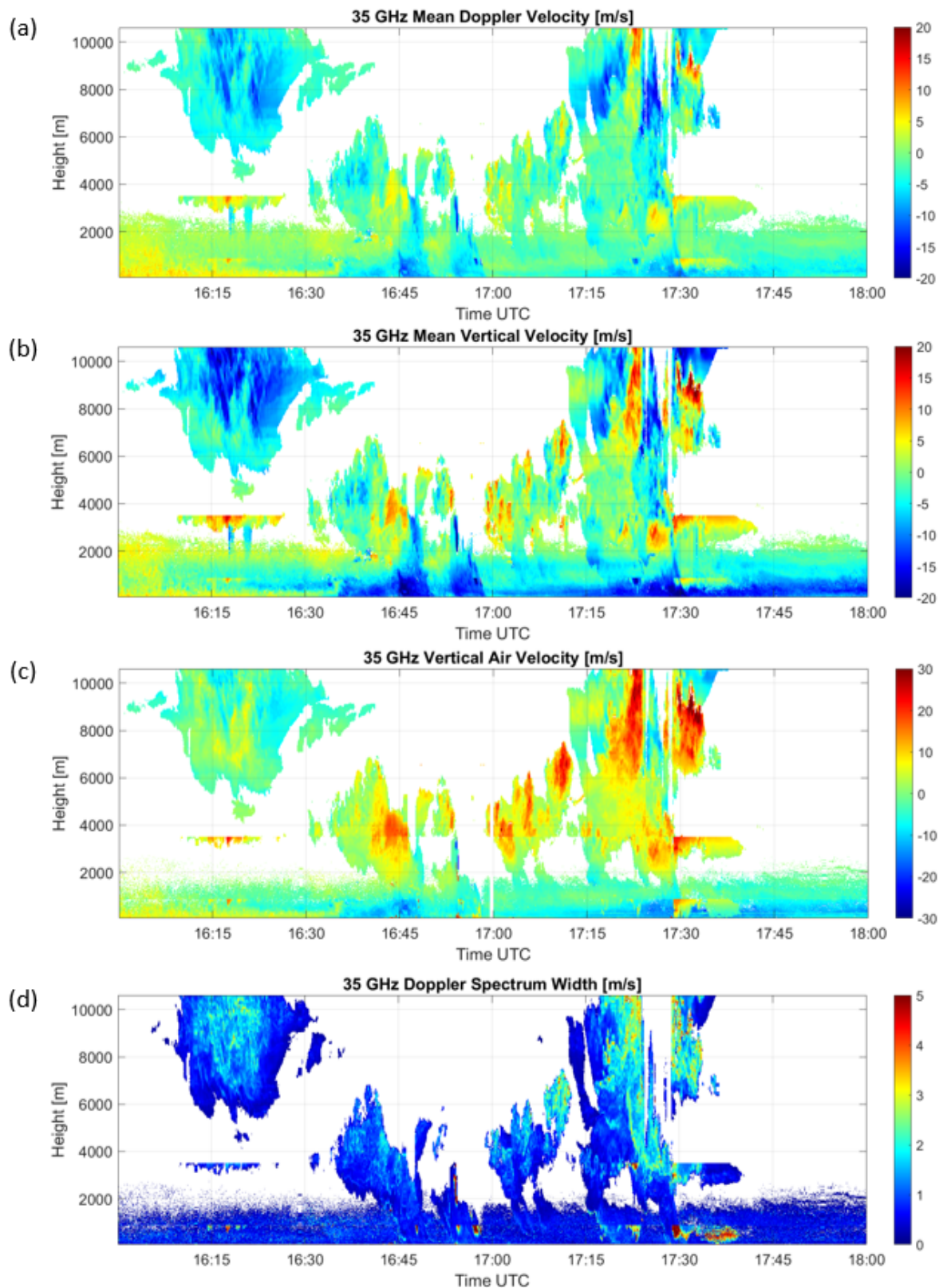


Figure 4.4: (a) Mean Doppler velocity, (b) mean vertical velocity, (c) vertical air velocity and (d) Doppler spectrum width on 2021-06-18 16:00 - 17:59 UTC from 35 GHz radar with 45° elevation

The radar images from 16:15 to 17:40 UTC are shown in Figures 4.5, 4.6 and 4.7 [34]. Lightning strikes

within the 5 minutes prior to the labelled time are marked by yellow asterisks. The red triangle shows the radar location and the red ruler shows the line of sight of the radar with each mark equal to 1 km. Lightning occurred in all four major clouds labelled in Figure 4.1. For the first cloud, lightning occurred at least 10 km away from the radar. For the second cloud, lightning occurred at a perpendicular distance of around 3 to 8 km from the radar. The third cloud only produced two lightning strikes after passing through the line of sight of the radar. The strikes were at a perpendicular distance of around 6 to 7 km from the radar. The fourth cloud produced a large number of lightning strikes from less than 1 km to more than 15 km away from the radar. Lightning was most active from 17:15 to 17:25 UTC, and became less active as the cloud passed through the line of sight of the radar and moved away.

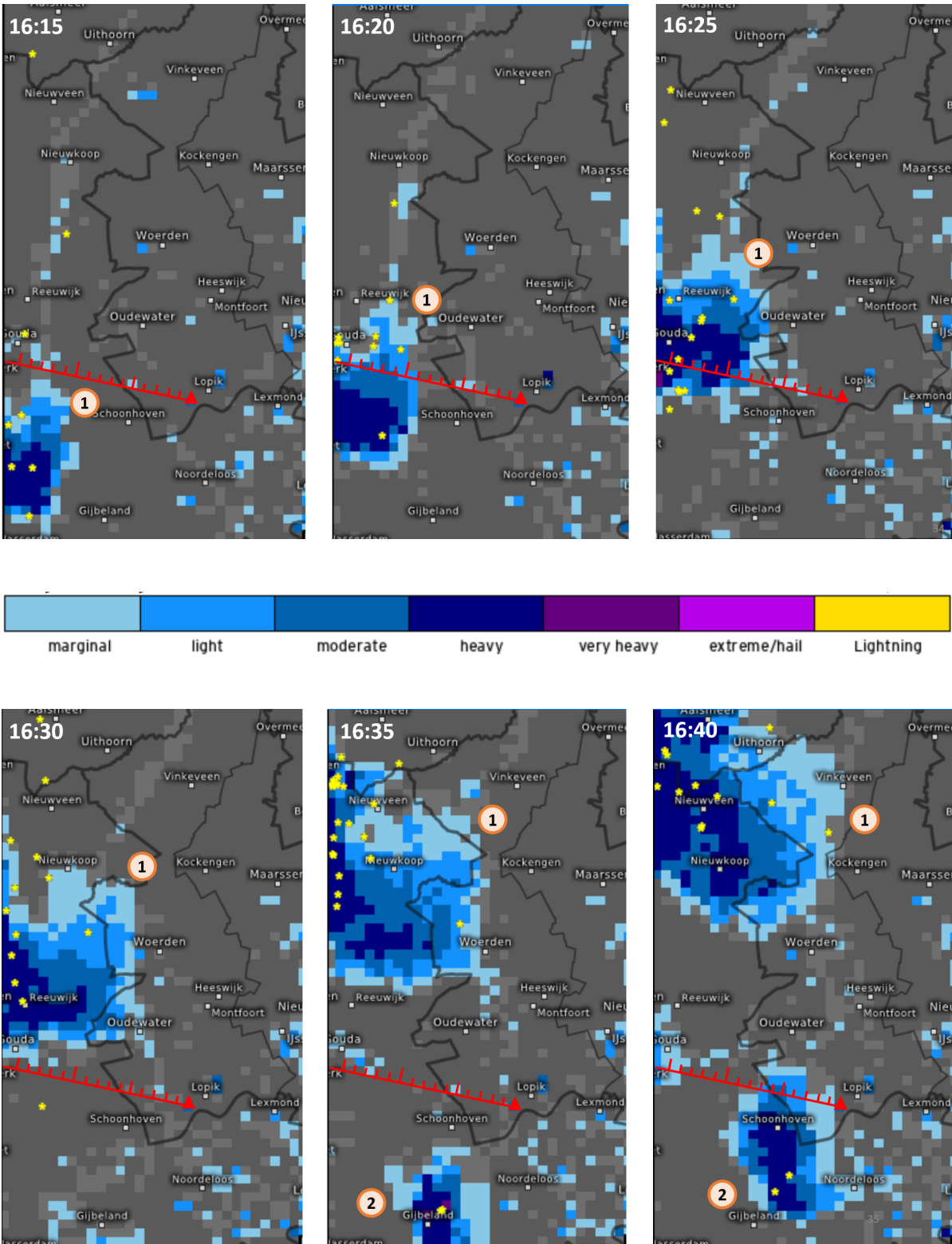


Figure 4.5: Radar images and location of lightning strokes (yellow asterisks) from 2021-06-18 16:10 to 16:40 UTC [34]. Red triangle shows radar location, red ruler shows line of sight of radar with each mark equal to 1 km

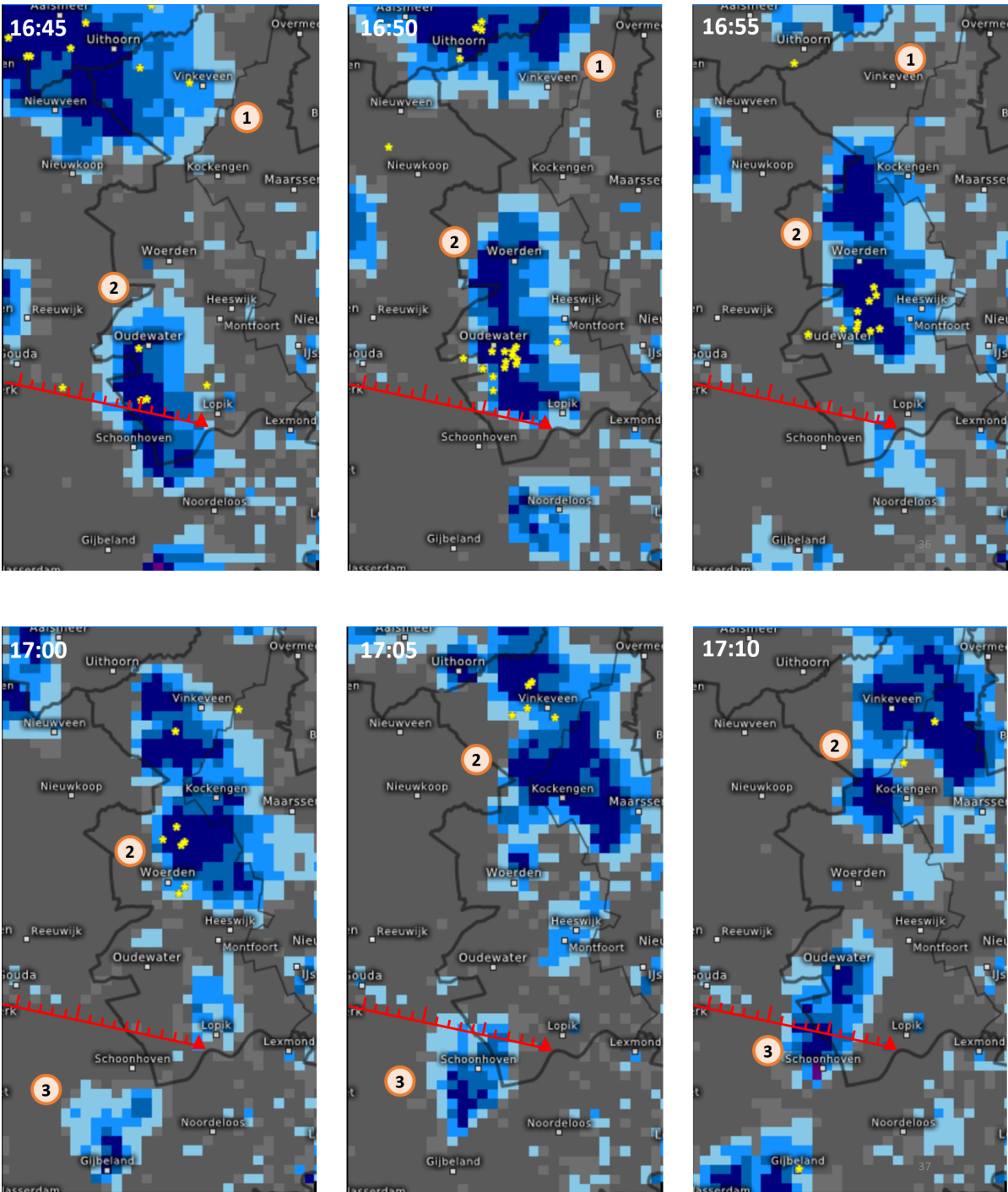


Figure 4.6: Radar images and location of lightning strokes from 2021-06-18 16:45 to 17:10 UTC [34]. Legend same as Figure 4.5

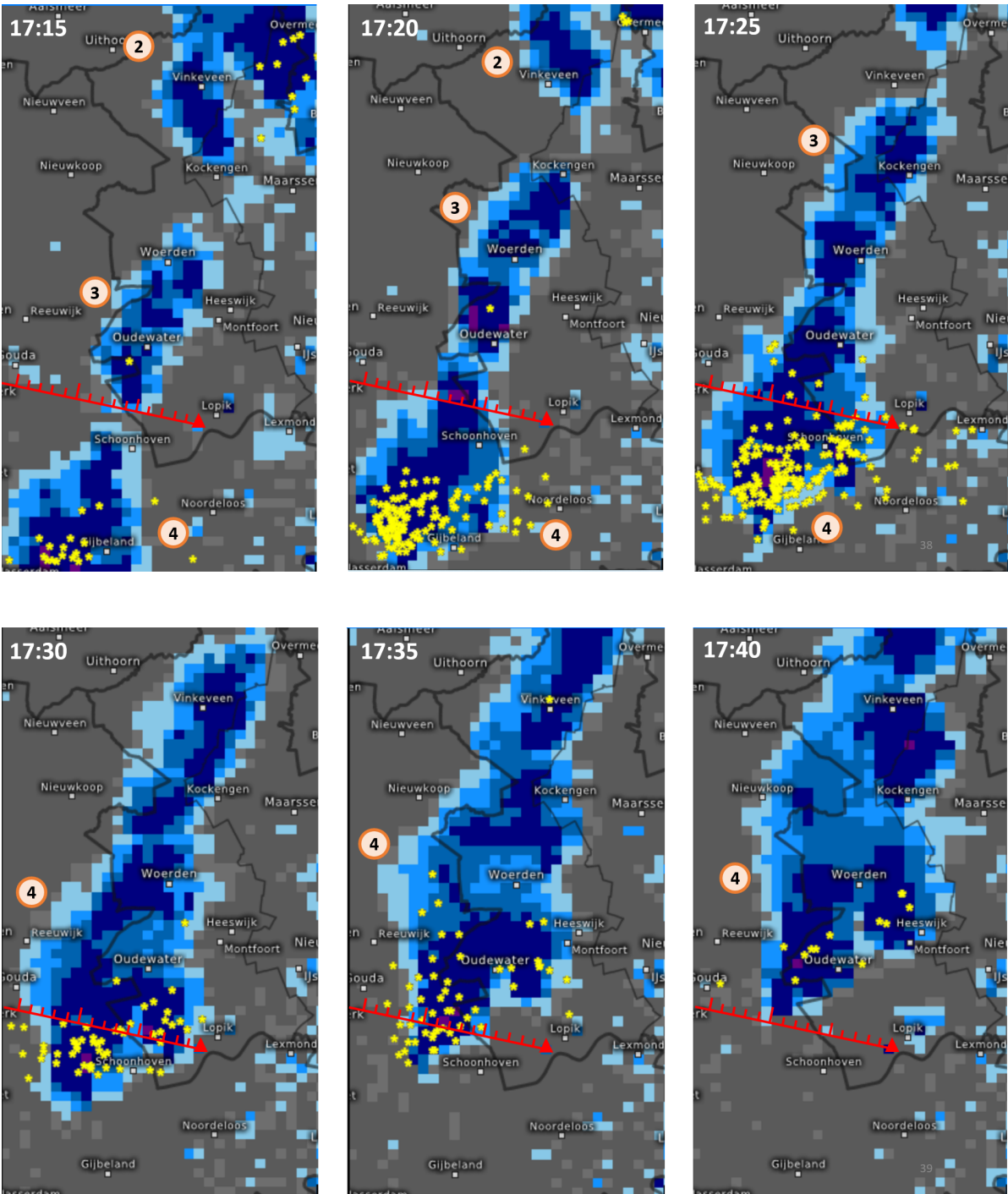


Figure 4.7: Radar images and location of lightning strokes from 2021-06-18 17:15 to 17:40 UTC [34]. Legend same as Figure 4.5

5

Methodology

This chapter explains the steps required to analyse radar data to investigate thunderstorm events. First, the way to compute polarimetric variables from raw data is explained in Section 5.1. Then, the steps to calibrate these variables is explained in Section 5.2. After that, methods to derive the specific differential phase shift and variables related to the Doppler spectrum are introduced in Sections 5.3 and 5.4. Then, Sections 5.5 and 5.6 explain how integrated variables and Doppler spectra were used to investigate properties of the thunderstorm cloud. Finally, Section 5.7 explains the motivation and method of performing scattering simulations.

5.1. Polarimetric variables calculation

The Level 1 dataset contains integrated polarimetric variables computed by the software of the radar. However, the software is a black box to users, thus it is more reliable to compute the integrated variables from the raw data (Level 0). In addition, spectral polarimetric radar variables, which require the raw data for their estimation, were used in this research.

From the Level 0 data, the integrated Z_{DR} and Ψ_{DP} can be computed by:

$$Z_{DR}(r) = 10 \log_{10} \left(\frac{\sum_v sZ_{hh}(r, v)}{\sum_v sZ_{vv}(r, v)} \right) \quad (5.1)$$

$$\Psi_{DP}(r) = \arctan \left(\frac{\sum_v \Im(-sC_{hh,vv}(r, v))}{\sum_v \Re(sC_{hh,vv}(r, v))} \right) \quad (5.2)$$

Here, r is the range and v is the Doppler velocity. Only data with signal-to-noise ratio above 10 dB were included in the summations.

The spectral differential reflectivity (sZ_{DR}) and spectral differential phase shift ($s\Psi_{DP}$) can be computed by:

$$sZ_{DR}(r, v) = 10 \log_{10} \left(\frac{sZ_{hh}(r, v)}{sZ_{vv}(r, v)} \right) \quad (5.3)$$

$$s\Psi_{DP}(r, v) = \arctan \left(\frac{-\Im(sC_{hh,vv}(r, v))}{\Re(sC_{hh,vv}(r, v))} \right) \quad (5.4)$$

Only the part of the spectra with signal-to-noise ratio above 10 dB were used to exclude the noisy edges of the spectra where values often fluctuate significantly. In addition, the spectra were smoothed using a 5-point moving average in Doppler bin to reduce noise.

The SL_{DR} and ρ_{hv} values presented in this report were taken from the Level 1 dataset.

5.2. Polarimetric calibration

An important part of this study is to look for the alignment of hydrometeors before or during lightning. This can be detected using polarimetric measurements such as Z_{DR} and K_{DP} . Negative values of these variables may suggest the vertical alignment of hydrometeors, thus it is important to calibrate these variables to make sure that their values are reliable.

The calibration of polarimetric variables was performed based on the knowledge that during light stratiform rain, small hydrometeors present in the rain and the cloud are approximately spherical. When the radar is looking towards the zenith, $Z_{DR} \approx 0$ dB and $\Psi_{DP} \approx 0^\circ$ [35]. The time period for calibration was chosen by looking for light stratiform rain with rainfall rate less than 10 mm/h. The cloud should reach as high as possible so that the calibration profile can reach as high as possible. The time period should be as close as possible to the thunderstorm cases to be analysed since calibration error may drift with time, and the radar should be looking towards the zenith.

5.2.1. Z_{DR} calibration

Multiplicative bias was assumed in the linear values of differential reflectivity, which means

$$z_{DR,true}(r) = C_1(r)z_{DR,raw}(r), \quad (5.5)$$

where $C_1(r)$ is the calibration parameter as a function of range to be determined, which is a function of the range r . A multiplicative bias for linear values was chosen since it is equivalent to an additive bias in decibels. If the radar is perfectly calibrated, $C_1(r)$ would be equal to one.

The calibration of Z_{DR} was performed using Z_{DR} computed from Level 0 data with a signal-to-noise (SNR) threshold of 10 dB. The calibration steps were as follows:

1. Mask bins with noisy values using the following criteria:

$$\begin{aligned} Z_{hh} &> -15 \text{ dBZ}, \\ \rho_{hv} &\text{ not NaN}, \\ |Z_{DR} [\text{dB}]| &< 1 \end{aligned}$$

2. Convert Z_{DR} from dB to linear values
3. Compute the 1-hour mean for each range bin to obtain the linear calibration profile

The SNR threshold and masking criteria were chosen empirically to remove noise to obtain a reliable calibration profile. Using higher SNR threshold and stricter masking criteria could give more reliable results, but more data will be removed especially near the cloud top, which means the calibration profile might not be high enough. Therefore, there is a trade-off when choosing the SNR threshold and masking criteria.

The cloud radar performs internal calibration every 1000 seconds for both 35 GHz and 94 GHz. At 94 GHz, Z_{DR} values are generally smaller shortly after internal calibration, which means they would be over-corrected if the same calibration profile is used for times shortly after internal calibration. Therefore, another calibration profile was computed with and applied to only data 30 timesteps (32 seconds) after internal calibrations. This phenomenon was not observed at 35 GHz, thus the same calibration profile was used at all times.

Within the melting layer, Z_{DR} deviates from 0 dB, creating a sharp increase in the calibration profile. To correct for this error, the melting layer throughout the hour was identified visually, and the values of the calibration profile within the melting layer was computed by linear interpolation.

The linear differential reflectivity value during light stratiform rain measured by a vertically pointing radar should be equal to 1 if the radar is perfectly calibrated. To correct for the multiplicative bias, the calibrated z_{DR} can be calculated by dividing the raw z_{DR} values by the mean z_{DR} profile obtained in step 3:

$$z_{DR,cal}(r) = z_{DR,raw}(r) \times \frac{1}{z_{DR,step\ 3}}, \quad (5.6)$$

The linear z_{DR} can be converted into dB scale afterwards.

5.2.2. Ψ_{DP} calibration

Additive bias was assumed for Ψ_{DP} , which means

$$\Psi_{DP,true}(r) = \Psi_{DP,raw}(r) + C_2(r), \quad (5.7)$$

where $C_2(r)$ is the calibration parameter as a function of range to be determined. If the radar is perfectly calibrated, $C_2(r)$ would be equal to zero.

The steps to calibrate Ψ_{DP} are similar to that of calibrating Z_{DR} . The only difference is the masking criteria in step 1, where the following criteria was used:

$$\begin{aligned} Z_{hh} &> -12 \text{ dBZ}, \\ \rho_{hv} &\text{ not NaN}, \\ |\Psi_{DP}| &< 5^\circ \end{aligned}$$

Correction for range bins within the melting layer was performed as for Z_{DR} calibration. At 94 GHz, correction for the timesteps shortly after internal calibration was also carried out.

Ψ_{DP} values during light stratiform rain measured by a vertically pointing radar should be equal to 0 if the radar is perfectly calibrated. To correct for the additive bias, the calibrated linear Ψ_{DP} can be calculated by subtracting the raw Ψ_{DP} values by the mean Ψ_{DP} profile obtained in step 3:

$$\Psi_{DP,cal}(r) = \Psi_{DP,raw}(r) - \Psi_{DP,step\ 3}(r), \quad (5.8)$$

5.3. Specific differential phase shift calculation

The specific differential phase shift (K_{DP}) was approximated from the calibrated Ψ_{DP} in degrees in two steps. First, Ψ_{DP} was smoothed using a 5-point moving average in range to reduce noise. Then, K_{DP} was computed by

$$K_{DP} = \frac{\Delta\Psi_{DP}}{2\Delta r} [^\circ/\text{km}], \quad (5.9)$$

where Δr is distance between adjacent range bins in km.

5.4. Variables from Doppler measurement

The measured Doppler velocity v_D of a particle is given by

$$v_D = (w + V_f) \sin \theta + v_H \cos \theta \cos(D - \pi - \phi), \quad (5.10)$$

where w is the vertical air velocity, v_H is the horizontal wind speed, V_f is the fall velocity of the particle, θ is the elevation angle of the radar, D is the wind direction relative to North and ϕ is the azimuth angle of the radar relative to North. The mean Doppler velocity can reflect the average motion of particles in a radar resolution volume along the line of sight of the radar. To extract it from Level 0 data, the first step is to unfold and dealias each Doppler spectra, which was done using the code from Peiyuan Wang [36]. Then, the mean Doppler velocity ($\overline{v_D}$) can be computed by

$$\overline{v_D} = \frac{1}{Z_{hh}} \sum_{v_{\text{SNR}>10 \text{ dB}}} v_D \times sZ_{hh}(r, v). \quad (5.11)$$

The Doppler spectrum width (σ_{v_D}) can also be computed by

$$\sigma_{v_D} = \sqrt{\frac{1}{Z_{hh}} \sum_{v_{\text{SNR}>10 \text{ dB}}} (v_D - \overline{v_D})^2 \times sZ_{hh}(r, v)}. \quad (5.12)$$

The mean vertical velocity ($\overline{w + V_f}$) can give information about the vertical motion of hydrometeors in thunderstorm clouds. It can be estimated by solving Equation 5.10 using the mean Doppler velocity

$(\overline{v_D})$ together with v_H and D estimated from the ECMWF model data.

It is also useful to extract the vertical air velocity, which can give information about the updraft and downdraft pattern in thunderstorm clouds. It can be estimated by assuming that the smallest particles in the Doppler spectra are so light that their fall velocity is very close to zero, thus their vertical velocity is equal to the vertical air velocity. Therefore, the first step is to identify the Doppler velocity of the rightmost valid bin of the Doppler spectra with a 10 dB SNR threshold. Then, the vertical air velocity w can be estimated by solving Equation 5.10 with $V_f = 0$ and v_H and D estimated from the ECMWF model data.

5.5. Analysing integrated variables

Integrated variables were used in this study to identify time instants and ranges where signals related to lightning activities are found. During lightning, the electric field in clouds would align ice crystals vertically, causing Z_{DR} and K_{DP} to become negative. When negative Z_{DR} or K_{DP} is observed in the integrated profile, more in depth analyses were carried out by plotting the spectral reflectivity, Z_{DR} and Ψ_{DP} at those time instances to understand the causes of those negative values.

Another useful variable is the linear depolarisation ratio (L_{DR}). High L_{DR} values may indicate vertical alignment of ice crystals due to cloud electrification [4]. However, the SL_{DR} values presented in this report were taken from the Level 1 dataset and have not been verified, thus should be treated with caution. Also, when SNR is low, SL_{DR} values may become large regardless of the characteristics of the particles.

Regions with low ρ_{hv} may be worth investigating as well as they could be regions where graupel and ice crystals co-exist, and they may collide with each other to produce an electric field. Nonetheless, same as SL_{DR} , the values of ρ_{hv} were taken from the Level 1 dataset and have not been verified. Also, when SNR is low, ρ_{hv} values may reduce regardless of the characteristics of the particles present. Therefore, comparisons were made between the sensitivity limit of the radar and the measured reflectivity to guarantee sufficient SNR for the analysis of the results.

5.6. Analysing Doppler spectrum

While integrated variables contain information about all particles within a radar resolution volume, Doppler spectra separate the contributions of particles with different Doppler velocities, hence different sizes or densities. With spectral Z_{DR} , it would be possible to identify whether negative Z_{DR} is contributed by small particles that would appear on the right part of the Doppler spectrum, or by large particles that would appear on the left part of the Doppler spectrum. If negative Z_{DR} is observed for small particles, it is likely that an electric field is present that aligns the small particles. On the other hand, negative Z_{DR} for large particles only may indicate the presence of conical graupel [37]. However, the possible transition from Rayleigh to Mie scattering regime may complicate these interpretations of spectral Z_{DR} .

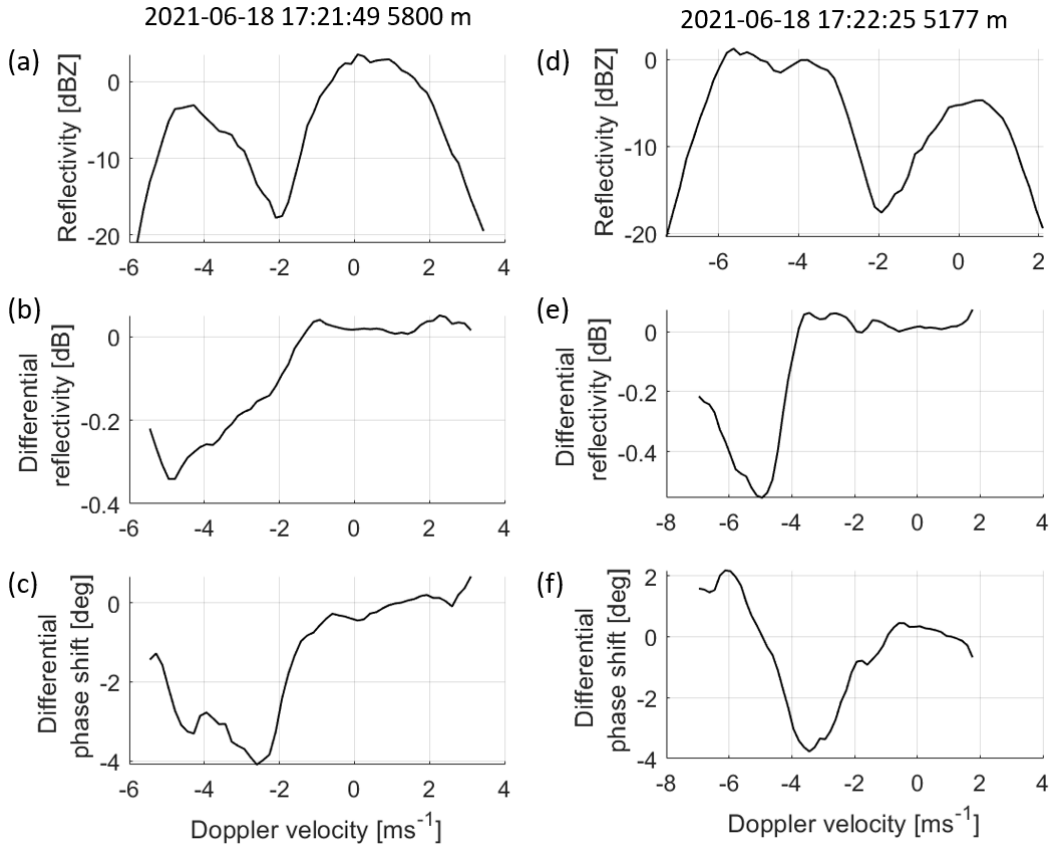


Figure 5.1: Two examples of Doppler spectra of Z_e , Z_{DR} and Ψ_{DP} at 35 GHz showing Mie scattering

The vertical gradient of the spectral differential phase shift ($s\Psi_{DP}$) is related to K_{DP} . A positive gradient indicates positive K_{DP} and vice versa. Another important use of $s\Psi_{DP}$ is to identify the Mie scattering regime. As mentioned before, fluctuations in Z_{DR} values in the Mie scattering regime makes it difficult to interpret those values. It is therefore crucial to identify when the Mie scattering regime begins. To do this, one can make use of the fact that the differential phase shift (Ψ_{DP}) is the sum of the two-way differential propagation phase (Φ_{DP}) and the differential backscatter phase (δ_{co}). In the Rayleigh scattering regime, spectral differential phase shift should be constant since the electromagnetic wave that scatters from particles at a particular range has propagated through the same set of particles in all previous ranges, and δ_{co} is zero. This part of the spectrum is often referred to as the Rayleigh plateau. In the Mie scattering regime, δ_{co} is non-zero and depends on the particle properties, thus the differential phase shift spectrum is no longer flat. Therefore, the Mie scattering regime begins when the left part of the differential phase shift spectrum starts to increase or decrease. The effect of noise may sometimes affect the identification of the Mie scattering regime. It is useful to know that the maximum or minimum of spectral Ψ_{DP} are often aligned with the maximum or minimum of spectral Z_{DR} . Thus, if the maxima or minima of $s\Psi_{DP}$ and sZ_{DR} are aligned, one can be more confident that the fluctuations observed are due to Mie scattering instead of noise.

The left column of Figure 5.1 shows an example where the Mie scattering regime can be clearly identified using $s\Psi_{DP}$. The Rayleigh plateau is found from -1 to 3 m s^{-1} , while Mie scattering occurs at Doppler velocity smaller than -1 m s^{-1} since δ_{co} becomes non-zero. sZ_{DR} follows a similar trend, which strengthens the proof that Mie scattering occurs. However, some cases can be more tricky, such as the one shown in the right column of Figure 5.1. Here, the Rayleigh plateau ends at about -0.5 m s^{-1} , while Z_{DR} only begins to decrease at about -4 m s^{-1} . To understand this better, scattering simulations are needed, which is discussed next.

5.7. Scattering simulations

Studying the Doppler spectrum of Z_{DR} is challenging when Mie scattering is involved. This is because Z_{DR} values fluctuate in the Mie scattering regime, which means that it will become difficult to determine whether the fluctuations in the observed Z_{DR} spectrum are due to changes in properties of hydrometeors or Mie scattering. Therefore, scattering simulations were carried out to understand how Mie scattering affects the Z_{DR} spectrum using the python code pyTmatrix [38]. The code is based on the T-matrix method [38], which is a numerical model of electromagnetic and light scattering by non-spherical particles with sizes comparable to the wavelength of the incident radiation. The code supports simulations of spheroids or cylinders. The scattering matrix of a scatterer depends on several parameters, including the axis ratio, ice fraction and canting angle. The axis ratio is defined as the length along its rotational axis to its width perpendicular to this axis. It is smaller than one for oblate particles and larger than one for prolate particles. Ice fraction (f_i) characterizes how much ice and air a scatterer is composed of, which affects the density of the particle. A value of 1 means pure ice, while a value of 0 means pure air. Ice fraction affects the complex effective relative permittivity of the scatterer (ε_{eff}). One approximation is given by the Maxwell-Garnett formula:

$$\frac{\varepsilon_{eff} - 1}{\varepsilon_{eff} + 2} = f_i \cdot \frac{\varepsilon_i - 1}{\varepsilon_i + 2}, \quad (5.13)$$

where ε_i is the complex relative permittivity of ice. The value of ε_i is $3.19015 + 0.00285i$ at 35 GHz and $3.19098 + 0.00750i$ at 94 GHz [39]. The complex effective refractive index of the scatterer (m_{eff}), which is a parameter that can be specified in the simulation code, can then be determined using

$$\varepsilon_{eff} = m_{eff}^2. \quad (5.14)$$

The canting angle refers to the Euler angle β of the scatterer defined in Figure 5.2.

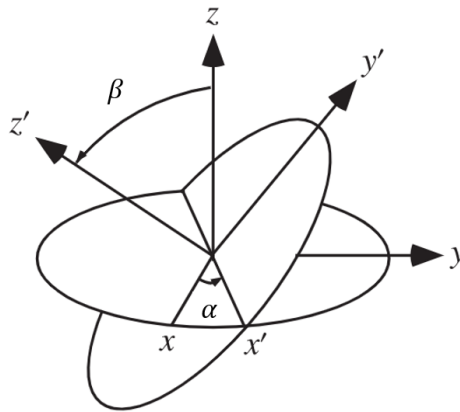


Figure 5.2: Definition of Euler angles α and β

In the simulation, a scatterer object in the shape of a spheroid was defined, and the backscatter radar reflectivity (Z_e), differential reflectivity (Z_{DR}) and differential backscatter phase (δ_{co}) at the selected frequency, 35 or 94 GHz, with 45° looking angle were retrieved. In the first experiment, the axis ratio of scatterers with zero mean canting angle was varied from 0.1 to 1.2, which covers the axis ratio range of plates, dendrites, aggregates and graupel. The ice fraction was fixed at 0.6, which is the average ice fraction of different types of particles. In the second experiment, the ice fraction of scatterers with zero mean canting was varied from 0.2 to 1, which covers the ice fraction range of plates, dendrites, aggregates and graupel. Simulations for both oblate and prolate particles were carried out, with an axis ratio of 0.8 or 1.2. In the third experiment, the canting angle was varied from 0° to 90° . Three sets of simulations were carried out to simulate different types of particles, including plates (axis ratio = 0.1, ice fraction = 0.98), aggregates (axis ratio = 0.8, ice fraction = 0.3) and graupel (axis ratio = 1.2, ice fraction = 0.6). For all simulations, the orientation of the scatterer follows a Gaussian distribution with a standard deviation of 0.1° . The Euler angle α of the scatterers (see Figure 5.2) follows a uniform distribution from 0 to 360° .

Calibration results

6.1. Z_{DR} calibration

The time for calibration is chosen to be 2021-05-19 11:00 - 11:59 UTC, which has a maximum rainfall rate of 2.4 mm/h. Figure 6.1(a) and (b) show the Z_{DR} profile near the cloud top before and after masking. The noisiest pixels near the edges of the cloud are removed, while the height of the profile is not reduced significantly.

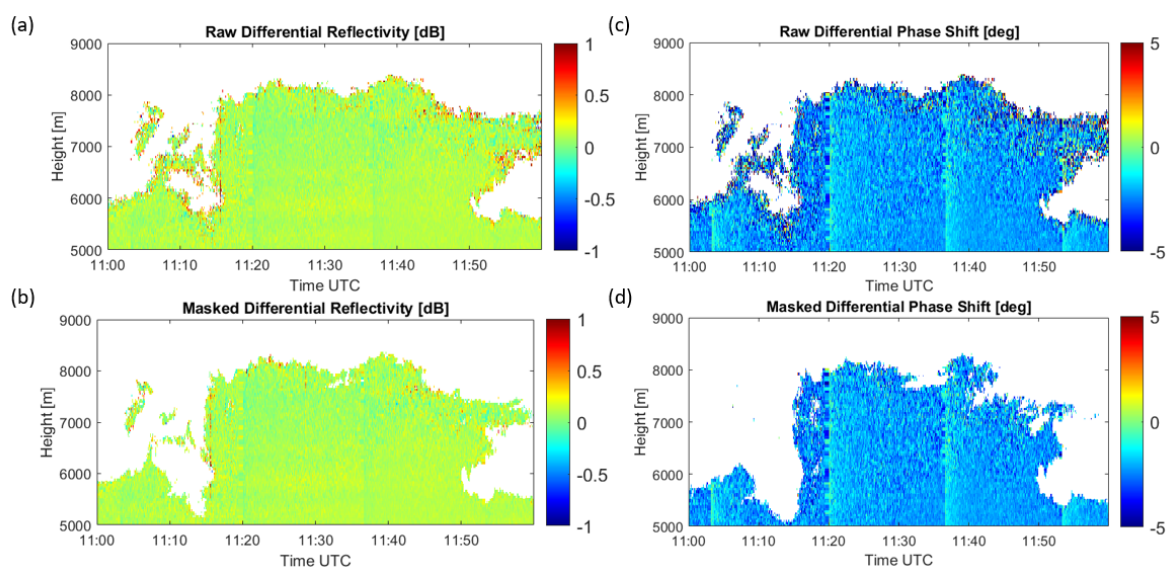


Figure 6.1: Raw and masked Z_{DR} (a-b) and Ψ_{DP} (c-d) at 94 GHz for the calibration time 2021-05-19 11:00 - 11:59 UTC

The calibration profiles obtained at 35 and 94 GHz are displayed in Figure 6.2. They are equivalent to $C_1(r)$ in Equation 5.5 or $z_{DR,step\ 3}$ in Equation 5.6. They can be applied to the same radar looking with a different elevation angle, but linear interpolation has to be carried out to compute the calibration profile if the range bins are different. In addition, the maximum available range of the calibration profile is only 8322 m and 8360 m at 35 GHz and 94 GHz respectively as there are no hydrometeors above this height during the calibration period. For ranges beyond the maximum available range, assumptions have to be made. For both frequencies, the calibration profile above 8000 m is taken to be the median of the calibration profile between 7000 m and 8000 m. The calibration profile for times right after internal calibration at 94 GHz is also shown in Figure 6.2(b). It generally follows the same trend as the original profile, but is slightly noisier as less data are being averaged. It is about 0.04 dB (or 0.01 in linear value) smaller than the calibration profile for other times.

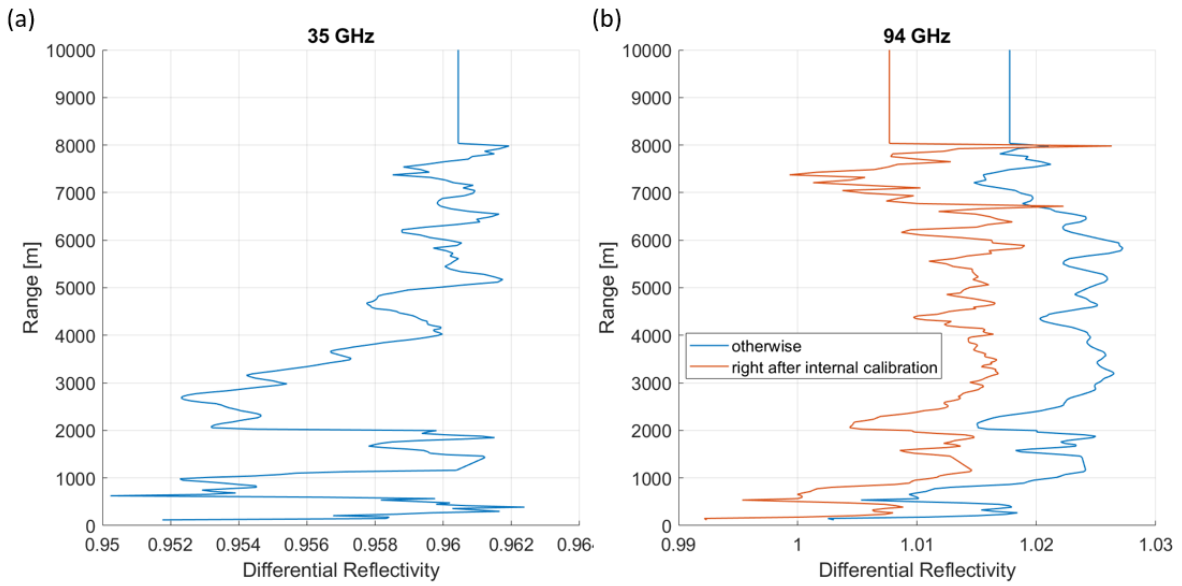


Figure 6.2: Z_{DR} calibration curves using 2021-05-19 11:00 - 11:59 UTC at (a) 35 GHz and (b) 94 GHz extrapolated to 10000 m

6.2. Ψ_{DP} calibration

The Ψ_{DP} profile of the calibration period before and after masking is shown in Figure 6.1(c) and (d). More pixels are masked out compared to Z_{DR} . For range bins beyond the maximum available range of the calibration profile, a different set of assumptions are applied as opposed to Z_{DR} since the trend of the calibration profiles are different. At 35 GHz, a 7-point moving average of the profile is computed, which is then extrapolated from 7000 m onward. At 94 GHz, the calibration profile above 8000 m is taken to be the median of the calibration profile between 7000 m and 8000 m. The resulting calibration profiles are displayed in Figure 6.3. At 94 GHz, correction for the timesteps shortly after internal calibration is also carried out, and the average difference between the two calibration profiles is 0.92° .

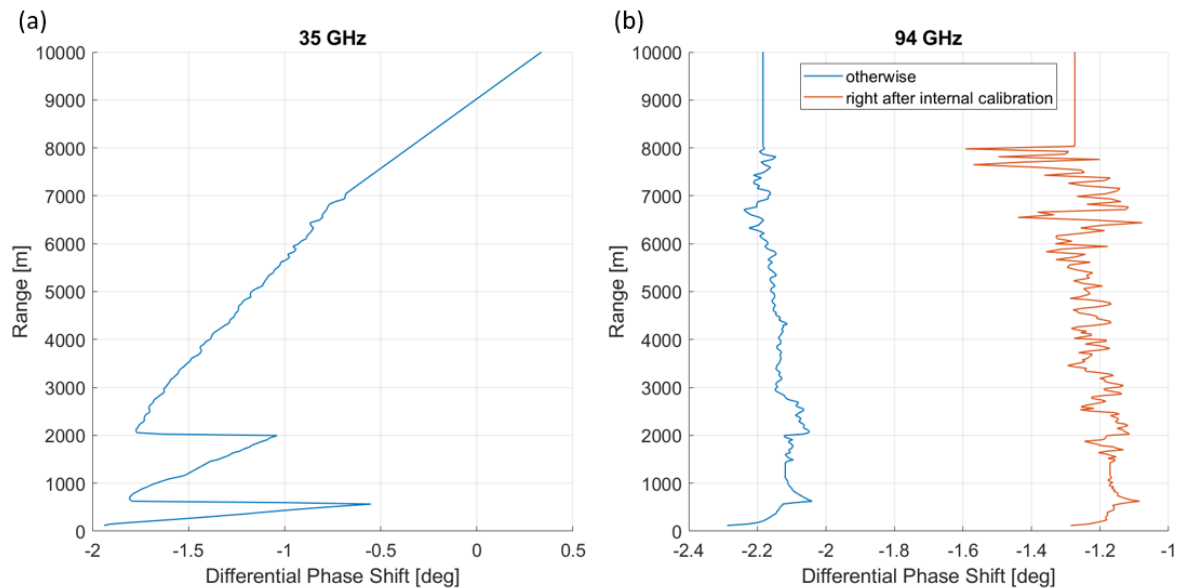


Figure 6.3: Ψ_{DP} calibration curves using 2021-05-19 11:00 - 11:59 UTC at (a) 35 GHz and (b) 94 GHz extrapolated to 10000 m

6.3. Evaluation

The calibration profiles are tested on the hour 2021-05-24 05:00 - 05:59 UTC, which has a maximum rainfall rate of 0.3 mm/h. Figure 6.4 and Figure 6.5 show the Z_{DR} and Ψ_{DP} values before and after calibration. It is evident that after calibration, the Z_{DR} and Ψ_{DP} values become closer to the expected value of 0 dB and 0 degree respectively. The raw Ψ_{DP} at 35 GHz shows clear discontinuities at around 500 m and 2000 m, which correspond to the change of chirps. These discontinuities disappear after calibration. However, the calibrated Ψ_{DP} at 94 GHz still shows traces of internal calibration. Nonetheless, the Ψ_{DP} values will only be used to calculate specific differential phase shift, which depends on the relative values of Ψ_{DP} of adjacent range bins only (see Section 5.3), so the current result is acceptable.

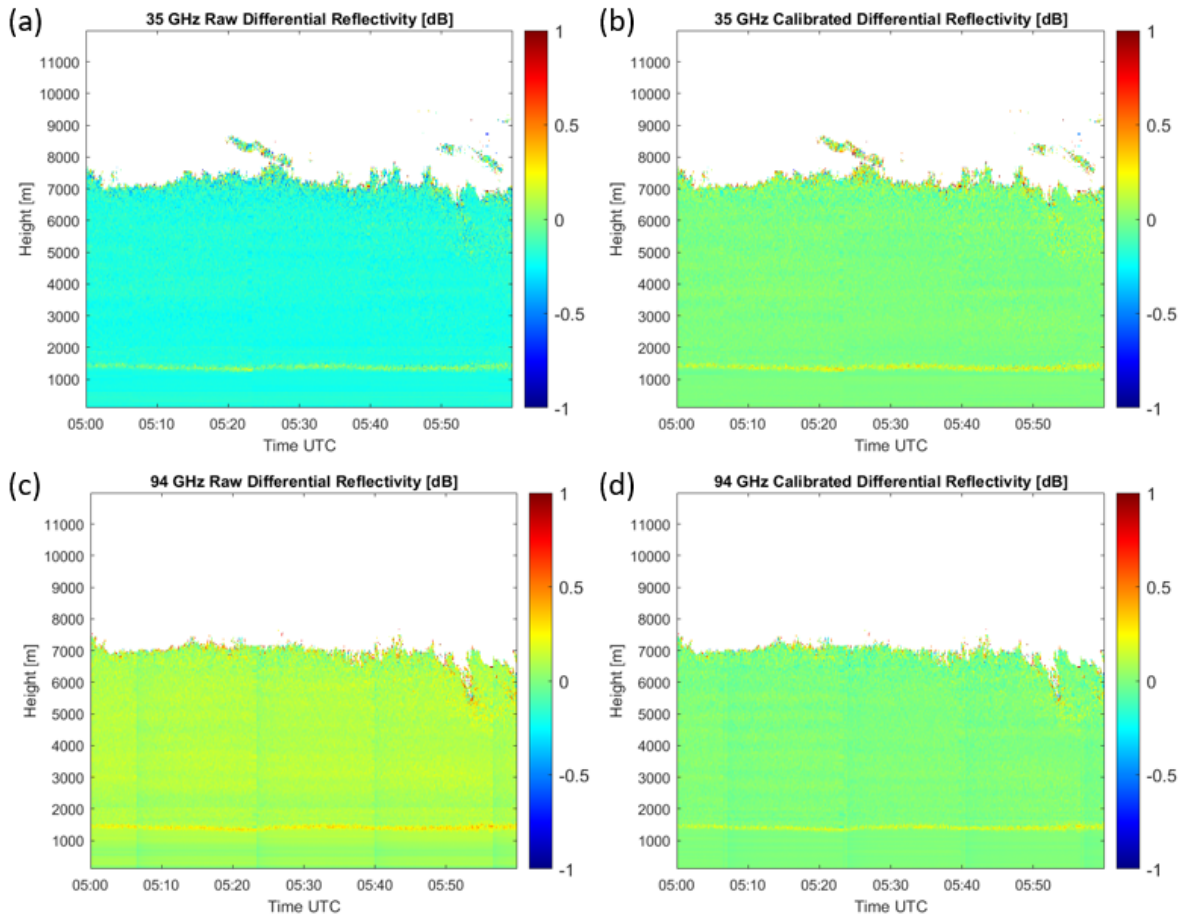


Figure 6.4: Raw and calibrated Z_{DR} on 2021-05-24 05:00 - 05:59 UTC at 35 GHz (a-b) and 94 GHz (c-d)

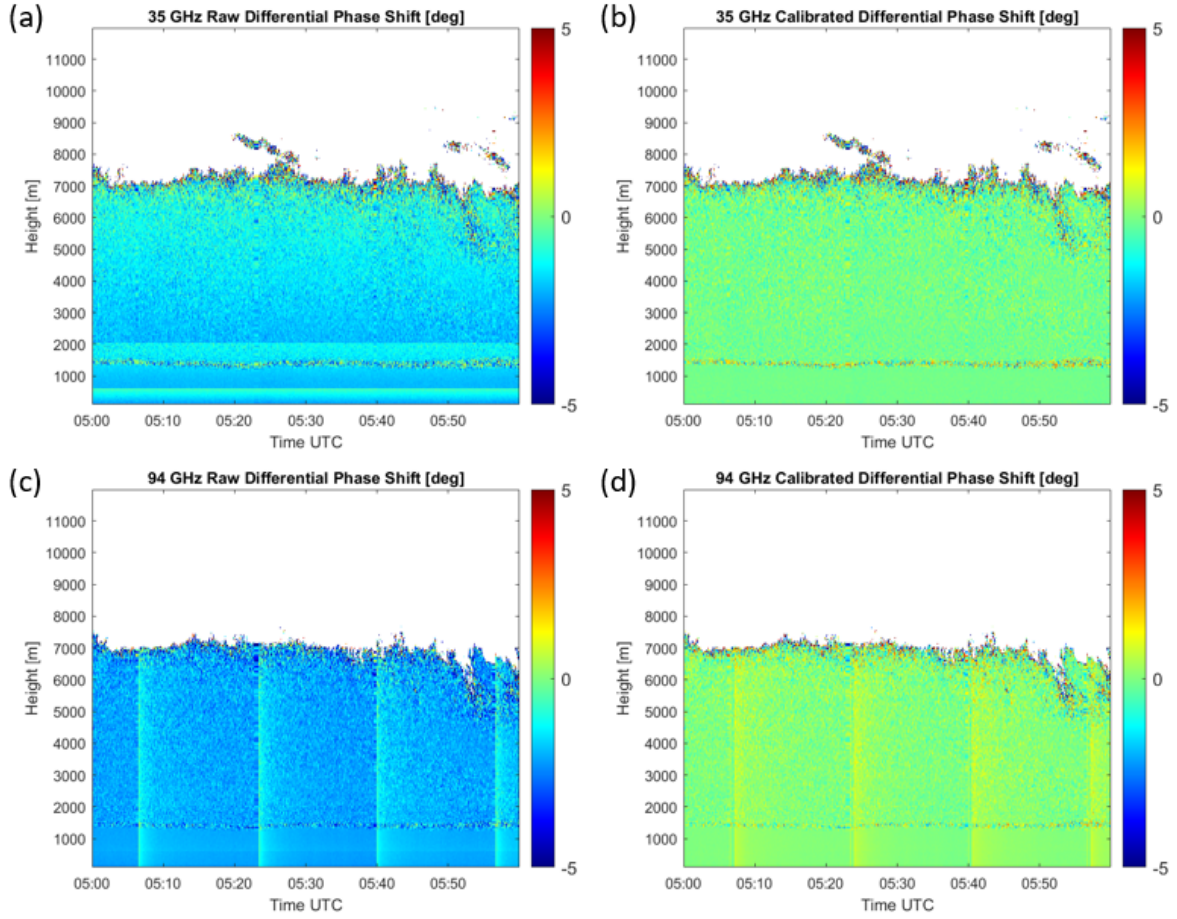


Figure 6.5: Raw and calibrated Ψ_{DP} on 2021-05-24 05:00 - 05:59 UTC at 35 GHz (a-b) and 94 GHz (c-d)

To evaluate the performance of the calibration quantitatively, the root mean square error is computed over the data after applying the mask in step 1 of the calibration procedure. The root mean square error of linear z_{DR} and Ψ_{DP} is given by

$$\sigma(z_{DR}) = \sqrt{\frac{\sum (z_{DR} - 1)^2}{n}} \quad (6.1)$$

$$\sigma(\Psi_{DP}) = \sqrt{\frac{\sum (\Psi_{DP})^2}{n}}, \quad (6.2)$$

where n is the number of samples.

The following formula can be used to convert a small value ΔZ_{DR} from linear scale to dB scale:

$$\Delta[Z_{DR} \text{ (dB)}] \approx 10 \log_{10} \left[1 + \frac{\Delta z_{DR}}{\text{mean}(z_{DR})} \right]. \quad (6.3)$$

Using this and taking $\text{mean}(z_{DR}) = 1$, the root mean square error of z_{DR} can be converted into dB scale, and the results are summarised in Table 6.1. It can be seen that the root mean square errors of both variables at 35 GHz and 94 GHz reduce significantly after calibration.

To see how sensitive the calibration profiles are to the choice of SNR threshold and calibration time period, calibration profiles are also computed with no SNR threshold and during another time of 2021-05-08 09:00 - 09:59 UTC. The resulting calibration profiles are shown in Figure 6.6 and Figure 6.7. The calibration profiles with and without SNR threshold are almost identical except for ranges near the

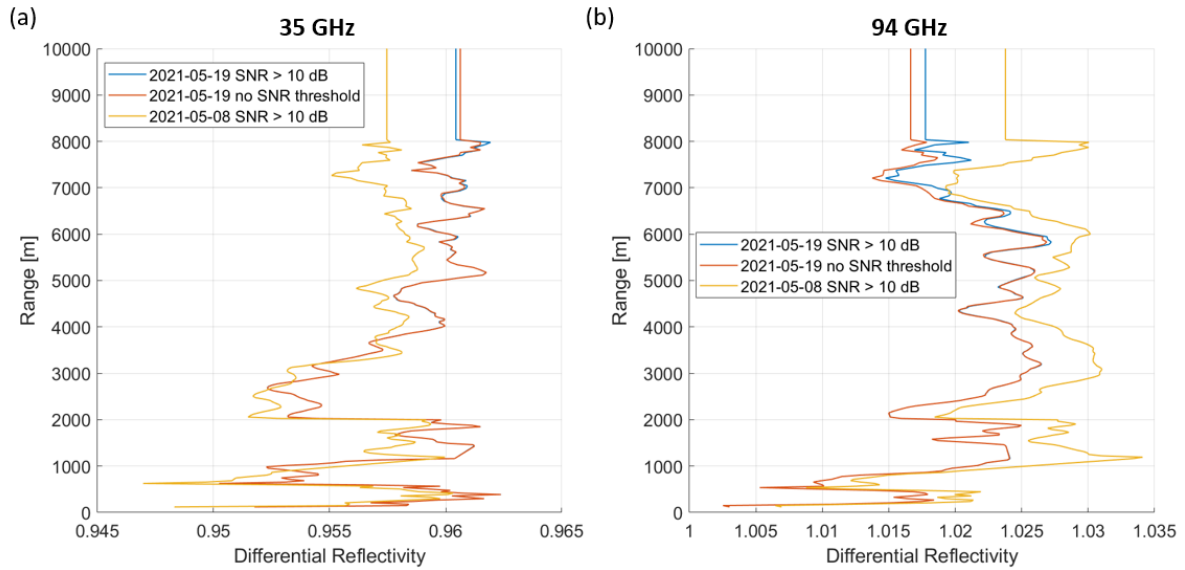
Table 6.1: Root mean square errors of Z_{DR} and Ψ_{DP} on 2021-05-24 05:00 - 05:59 UTC before and after calibration using calibration profile from 2021-05-19 11:00 - 11:59 UTC

	35 GHz raw	35 GHz calibrated	94 GHz raw	94 GHz calibrated
$\sigma[Z_{DR} \text{ (dB)}]$	0.1862	0.0501	0.1112	0.0468
$\sigma[\Psi_{DP} \text{ (}^\circ\text{)}]$	1.5752	0.534	2.080	0.492

cloud top. This is because Z_{DR} is reflectivity weighted, thus removing the part of the spectrum with low reflectivity only changes the integrated Z_{DR} value by negligible amount. An exception is when the remaining part of the spectrum also has low values, which is often the case near the cloud top. The profiles obtained using a different calibration time period show similar trend as the original profile with a small offset. The mean differences between the different calibration profiles with the one computed by 2021-05-19 11:00 - 11:59 UTC are summarised in Table 6.2.

Table 6.2: Mean difference between different calibration profiles and the profile calibrated by 2021-05-19 11:00 - 11:59 UTC with SNR > 10 dB

	35 GHz Z_{DR} [dB]	Ψ_{DP} [°]	94 GHz Z_{DR} [dB]	Ψ_{DP} [°]
Right after internal calibration	-	-	0.04	0.92
No SNR threshold	3e-4	0.01	0.002	0.02
2021-05-08 09:00 - 09:59 UTC	0.009	0.20	0.02	0.03

**Figure 6.6:** Z_{DR} calibration curves at (a) 35 GHz and (b) 94 GHz for 2021-05-19 11:00 - 11:59 UTC with and without 10 dB SNR threshold and for 2021-05-08 09:00 - 09:59 UTC with 10 dB SNR threshold

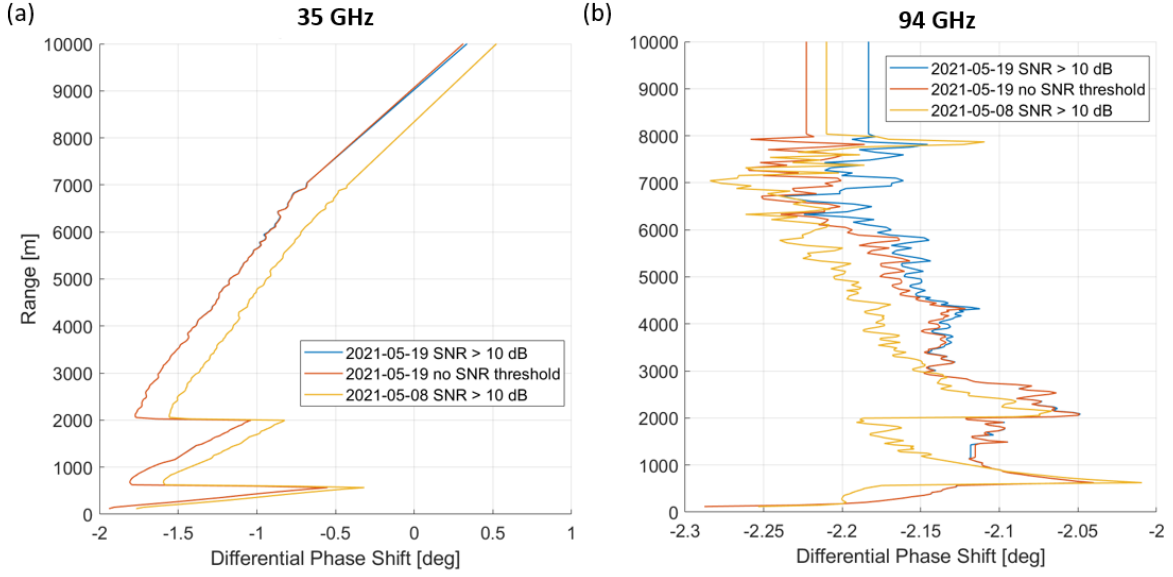


Figure 6.7: Ψ_{DP} calibration curves at (a) 35 GHz and (b) 94 GHz for 2021-05-19 11:00 - 11:59 UTC with and without 10 dB SNR threshold and for 2021-05-08 09:00 - 09:59 UTC with 10 dB SNR threshold

The total expected error of the calibration curve can be approximated by the sum of the root mean square error (σ in Table 6.1) and the error due to the choice of calibration period (Δ , third row of Table 6.2). It can be approximated by:

$$\text{Total expected error} = \sqrt{\sigma^2 + \Delta^2} \quad (6.4)$$

The total expected error of the calibration curve for Z_{DR} is 0.051 dB at both 35 and 94 GHz. This is smaller than the error of the instrument, which is 0.1 dB. The total expected error of the Ψ_{DP} calibration curve is 0.57° at 35 GHz and 0.49° at 94 GHz.

6.4. Specific differential phase shift calculation

An example of a Ψ_{DP} profile without calibration, after calibration, after smoothing and the corresponding K_{DP} profile at 35 GHz during light stratiform rain is shown in Figure 6.8. The calibrated Ψ_{DP} is close to zero as expected except at the melting layer at around 1400 m, but it contains some noise. Therefore, K_{DP} shows the right trends but is still noisy. The specific signature of the melting layer, which is a clear negative and positive slope of the differential phase at the bottom and top of the melting layer respectively, can be used for automatic detection of the melting layer. Because of the expected decrease in signal-to-noise ratio at the top of the cloud, the variance in range of the differential phase significantly increases, limiting therefore the calibration profile in range and microphysical studies based on polarimetry at the top of the cloud.

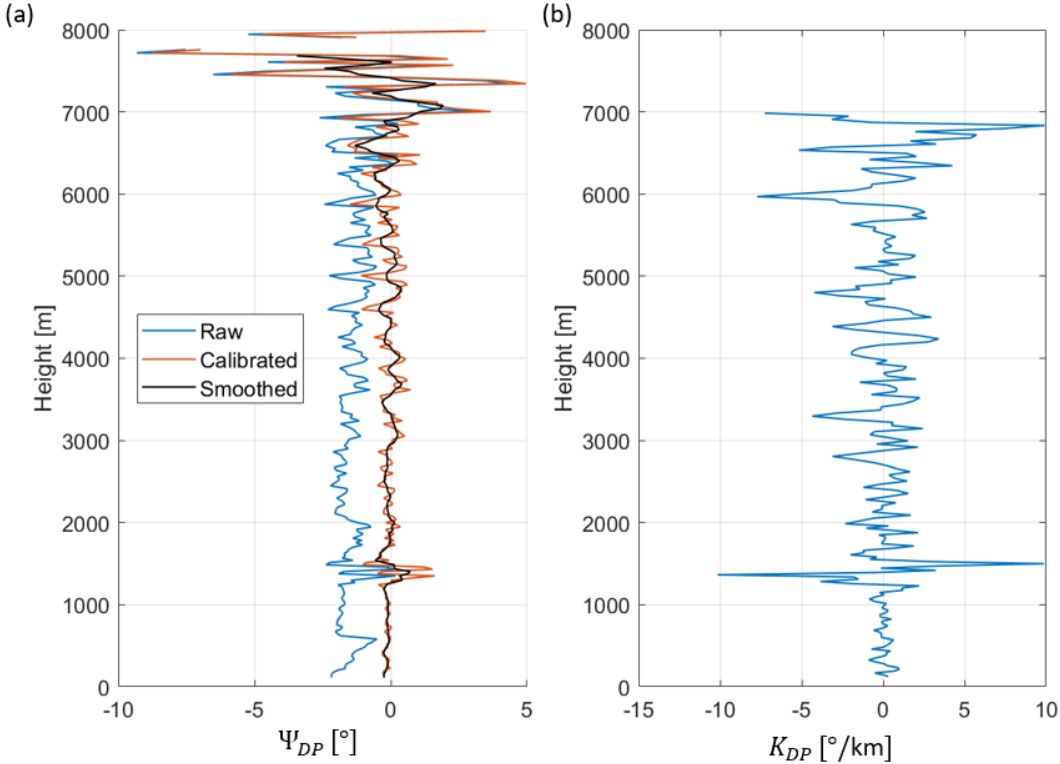


Figure 6.8: (a) Ψ_{DP} profiles before calibration, after calibration and after smoothing and (b) the corresponding K_{DP} profile at 35 GHz during light stratiform rain at 2021-05-24 05:27:29 UTC

7

Scattering simulation results

This chapter gives an overview of the dependencies of spectral polarimetric radar variables of particles versus axis ratio, ice fraction and canting angle in the Rayleigh and Mie scattering regimes based on scattering simulations.

7.1. Axis ratio

Figure 7.1 shows the simulation results for horizontally aligned scatterers with ice fraction 0.6 with different axis ratios at 35 GHz and 94 GHz. The radius refers to the maximum radius of the spheroid, i.e. half the length of its long axis. From Figure 7.1(a), at 35 GHz, the first Mie minimum occurs at a maximum radius of around 2 mm for axis ratio 1.2, 2.6 mm for axis ratio 0.8, and 3.2 for axis ratio 0.4. Mie scattering occurs for smaller particles at 94 GHz than at 35 GHz. From Figure 7.1(d), at 94 GHz, the first Mie minimum occurs at a maximum radius of around 1.2, 1 and 0.8 mm for axis ratio 0.4, 0.8 and 1.2 respectively. More Mie minima are observed at 94 GHz within the same range of sizes, which increases the complexity of the interpretation of the spectral polarimetric radar variables. Therefore, attention will be put on understanding scattering behaviours at 35 GHz first.

In the Rayleigh scattering regime, Z_{DR} decreases with increasing axis ratio, with positive values for oblate spheroids (axis ratio < 1) and negative values for prolate spheroids (axis ratio > 1). When entering the Mie scattering regime, Z_{DR} of oblate particles increases slightly, while that of prolate particles decreases. At the first Mie minimum, particles with axis ratio 0.1, 0.4 and 1.2 give a trough in Z_{DR} , but those with axis ratio 0.8 give a peak. In addition, the lines for different axis ratios cross over each other in the graph of Z_{DR} , meaning that the trend between Z_{DR} and axis ratio depends on particle size. δ_{co} of oblate particles increases when entering the Mie scattering regime and gives a peak at the first Mie minimum, while that of prolate particles decreases and gives a trough.

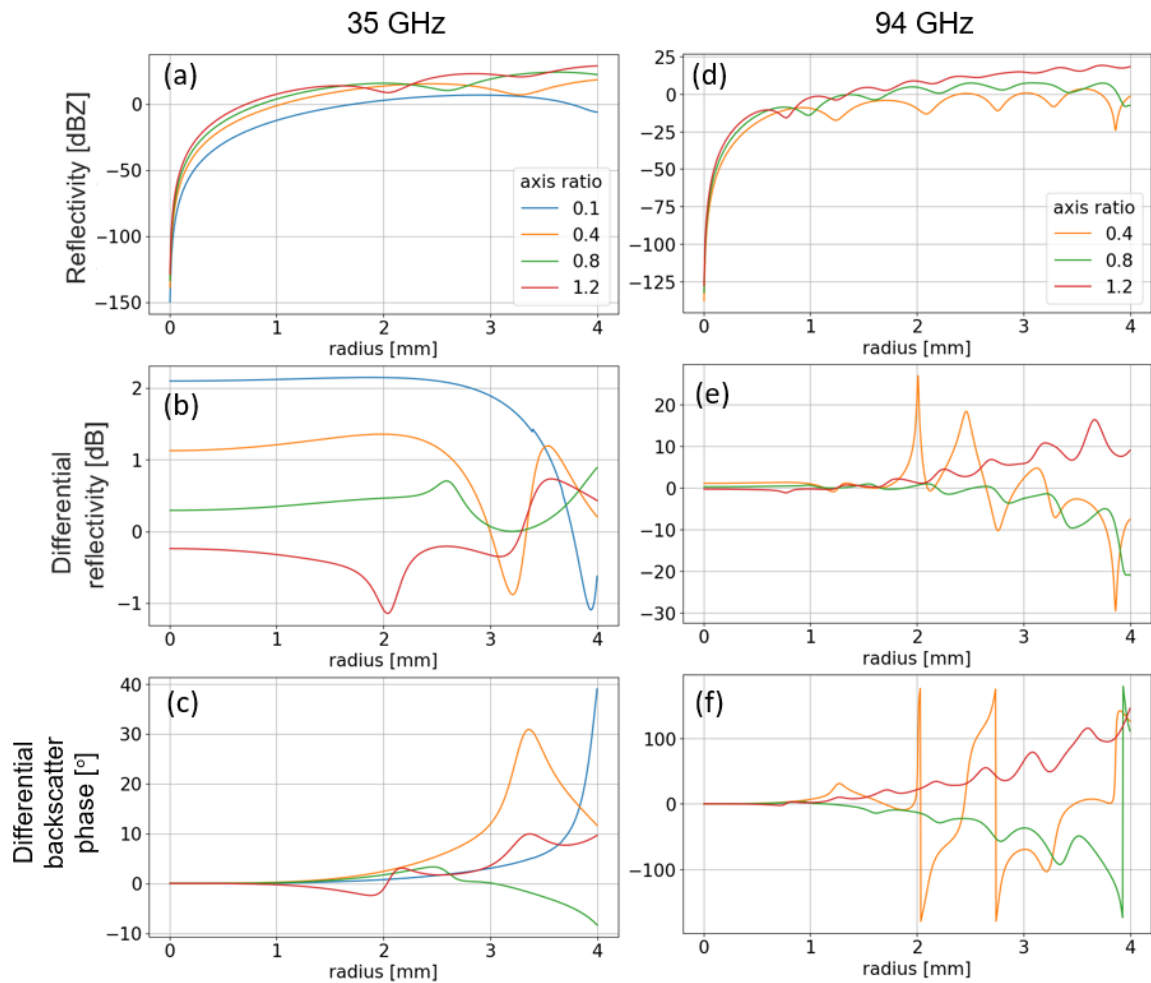


Figure 7.1: Simulated (a) radar reflectivity, (b) differential reflectivity and (c) differential backscatter phase for horizontally aligned scatterers with different axis ratios as a function of maximum radius at 35 GHz with 45° looking angle. (d-f) show the same at 94 GHz (axis ratio 0.1 is not shown as the simulation could not converge). All scatterers have ice fraction of 0.6.

7.2. Ice fraction

Figure 7.2 shows two sets of simulations for horizontally aligned scatterers with different ice fractions. In the Rayleigh scattering regime, the magnitude of Z_{DR} increases with increasing ice fraction. The first optimum of Z_{DR} is reached at a smaller size for scatterers with higher ice fraction. For low ice fraction (0.2, 0.4 and 0.6), Z_{DR} keeps the same sign after entering the Mie scattering regime (except for radius larger than 3.2 mm for scatterers with axis ratio 0.8 and ice fraction 0.6). When ice fraction is large (0.8 and 1), the sign of Z_{DR} is flipped soon after reaching the first optimum, and the trend is rather unpredictable. The differential backscatter phase initially increases (decreases) for oblate (prolate) particles when entering the Mie scattering regime. The sign reverses afterwards, and the trend after that is less predictable especially for high ice fraction.

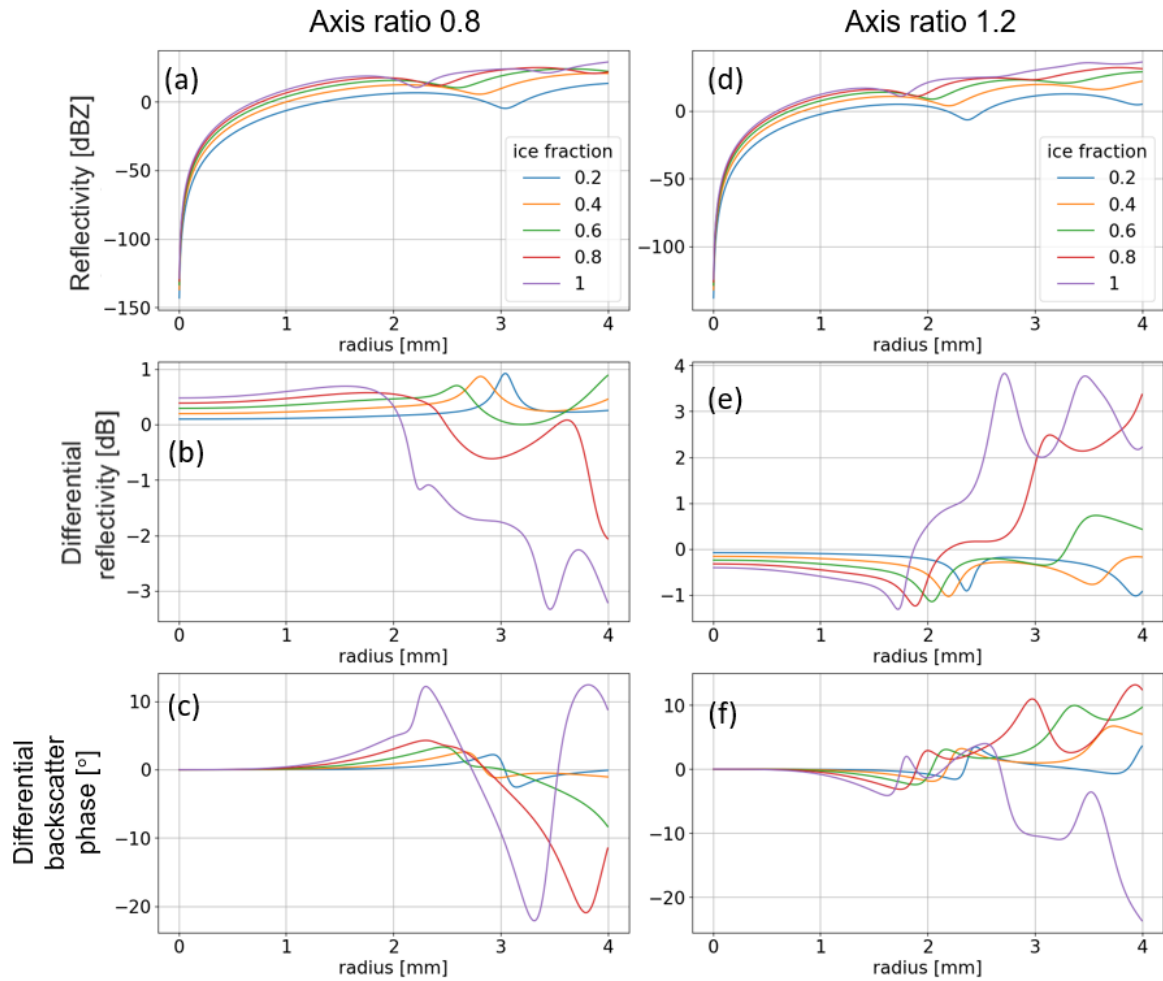


Figure 7.2: Simulated radar variables for horizontally aligned scatterers with different ice fractions as a function of maximum radius at 35 GHz with 45° looking angle. (a-c) show the radar reflectivity, differential reflectivity and differential backscatter phase for scatterers with fixed axis ratio of 0.8. (d-f) show the same for scatterers with fixed axis ratio of 1.2

7.3. Canting angle

Figure 7.3 shows three sets of simulations for scatterers with different canting angles. For oblate particles (left and middle columns), Z_{DR} in the Rayleigh scattering regime is negative when the canting angle becomes larger than 45°. One can understand this as the effective axis ratio of an oblate scatterer getting larger than one when it becomes vertically aligned. The opposite is true for prolate particles. However, in the Mie scattering regime, the relationship between the sign of Z_{DR} and the canting angle is not trivial. For scatterers similar to plates with axis ratio 0.1 and ice fraction 0.98, the first optima of Z_{DR} is positive for $\beta = 90^\circ$ but negative for $\beta = 0^\circ$. There is no sharp optima for $\beta = 30^\circ$ or 60° . For scatterers similar to conical graupel with axis ratio 1.2 and ice fraction 0.6, the sign of Z_{DR} also changes when particle size becomes larger. The differential backscatter phase does not have a trend that can be easily summarised for different canting angles for all three cases.

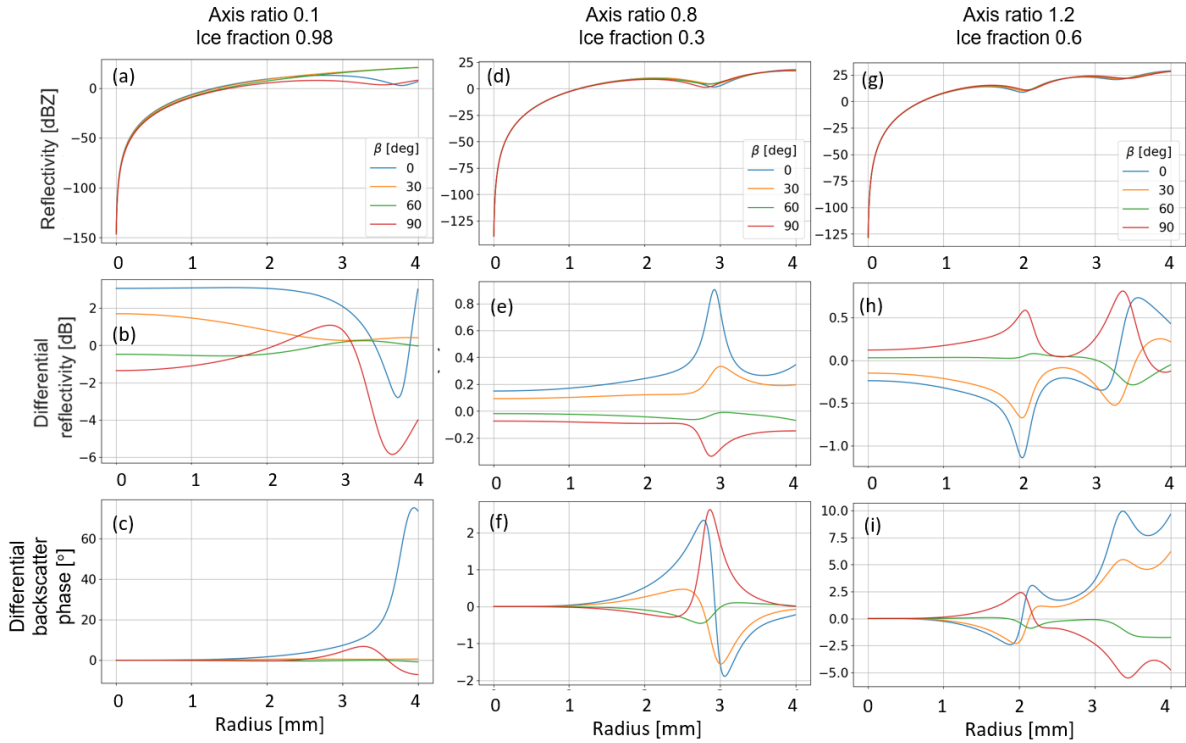


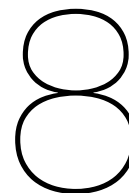
Figure 7.3: Simulated radar variables for horizontally aligned scatterers with different canting angles as a function of maximum radius at 35 GHz with 45° looking angle. (a-c) show the radar reflectivity, differential reflectivity and differential backscatter phase for scatterers similar to plates with fixed axis ratio of 0.1 and ice fraction of 0.98. (d-f) show the same for scatterers similar to aggregates with fixed axis ratio of 0.8 and ice fraction of 0.3. (g-i) show the same for scatterers similar to conical graupel with fixed axis ratio of 1.2 and ice fraction of 0.6

7.4. Summary

Table 7.1: Z_{DR} characteristics in Rayleigh scattering regime and trend of δ_{co} before first Mie minimum

	Z_{DR} in Rayleigh scattering regime	δ_{co} trend before first Mie minimum for horizontally aligned scatterers
Axis ratio < 1	positive, increase with decreasing axis ratio	increase
Axis ratio > 1	negative, more negative with increasing axis ratio	decrease
Ice fraction	magnitude increases with increasing ice fraction	same trend as Z_{DR} except for large ice fraction

In this chapter, the effects of axis ratio, ice fraction and canting angle of scatterers on Z_{DR} and δ_{co} are investigated. Table 7.1 summarises the key trends of Z_{DR} in the Rayleigh scattering regime and the trend of δ_{co} before the first Mie minimum for horizontally aligned scatterers with different axis ratios and ice fractions. Changing the canting angle has similar effect as altering the axis ratio of the scatterers in terms of the initial trend of Z_{DR} . In general, the sign of Z_{DR} is the same as the sign of δ_{co} before the first Mie minimum. However in some cases, δ_{co} shows a sign inversion at the first Mie minimum. The fluctuations of Z_{DR} and δ_{co} after the first Mie minimum are difficult to predict and often involve sign changes. The most unpredictable behaviours are found when ice fraction is high.



Case analysis

The original plan of this case study is to make use of both 35 GHz and 94 GHz cloud radar. However, it is found that the 94 GHz radar is not that useful due to several problems. First, electromagnetic waves at higher frequency suffer from larger attenuation. This means that the 94 GHz radar often cannot penetrate through tall thunderstorm clouds. Figure 8.1 shows two spectograms of Z_{DR} in a thunderstorm cloud at 35 and 94 GHz. The spectogram at 35 GHz reaches more than 10 km, but the spectogram at 94 GHz ends much lower.

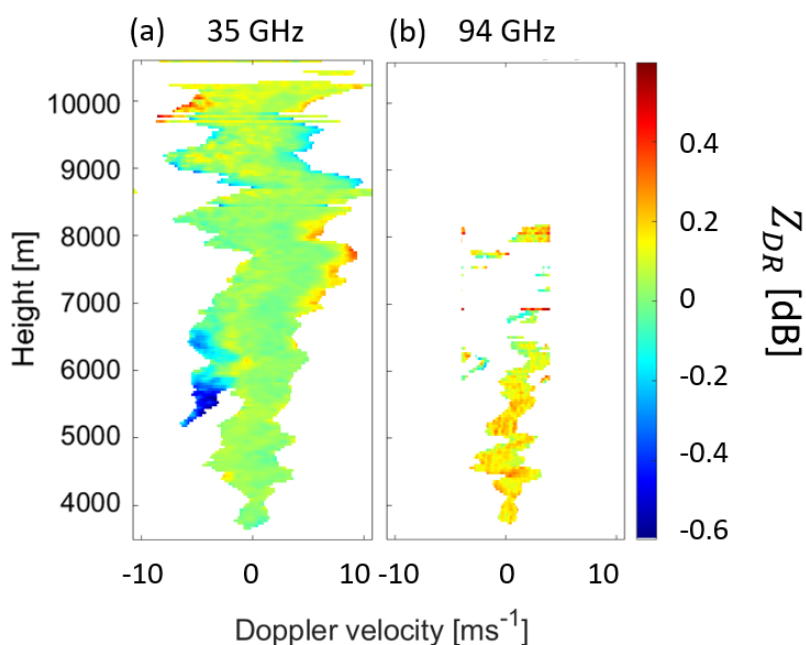


Figure 8.1: Spectrogram of Z_{DR} at 35 GHz (a) and 94 GHz (b) at 2021-06-18 17:21:49 UTC showing that part of the spectrum is missed at 94 GHz

Second, the spectra at 94 GHz are often more noisy. After applying a 10 dB SNR threshold, the remaining spectra are less broad. As a result, the 94 GHz radar misses out some interesting signals detected at 35 GHz. For example in Figure 8.1, negative Z_{DR} values are observed in the left part of the spectogram at 35 GHz from 5000 m to 6500 m. However, this part of the spectrum is missed out at 94 GHz. Figure 8.3(a) shows a spectrum of reflectivity at another time instant. The right peak at 35 GHz is missed out at 94 GHz.

Another issue is that the Nyquist velocity at 94 GHz is only 4 m s⁻¹, which is about 3 times smaller

than that at 35 GHz. When the true Doppler spectrum is wider than 8 m s^{-1} , the spectrum at 94 GHz is aliased and cannot be recovered. An example is shown in Figure 8.2. The spectrum width at 35 GHz is about 10 m s^{-1} . Comparing Figure 8.2(a) at 35 GHz and Figure 8.2(b) at 94 GHz, the spectrum below 3800 m at both frequencies should correspond to the same medium. From the shape of the spectrum, the right spectral peak from 3900 m to 4200 m at 35 GHz should be the same medium as the left spectral peak at the same height at 94 GHz. At 35 GHz, the right spectral peak from 4200 m to 4400 m has lower reflectivity than the right spectral peak from 3900 m to 4200 m, but at 94 GHz, the spectral peak from 4200 m to 4400 m has comparable reflectivity as the left spectral peak from 3900 m to 4200 m. This suggests that the spectral peak from 4200 m to 4400 m at 94 GHz is not the same medium as the right spectral peak at the same height at 35 GHz that is connected to the lower right part of the spectrum. Instead, the spectral peak from 4200 m to 4400 m and the right spectral peak from 3800 m to 4200 m at 94 GHz could be the aliased spectrum of the left spectral peak at the same height at 35 GHz. Therefore, the red part on the right of the spectral Z_{DR} at 94 GHz (Figure 8.2(c)) between 3800 m and 4500 m could be the result of Doppler aliasing of the left part of the true spectrum.

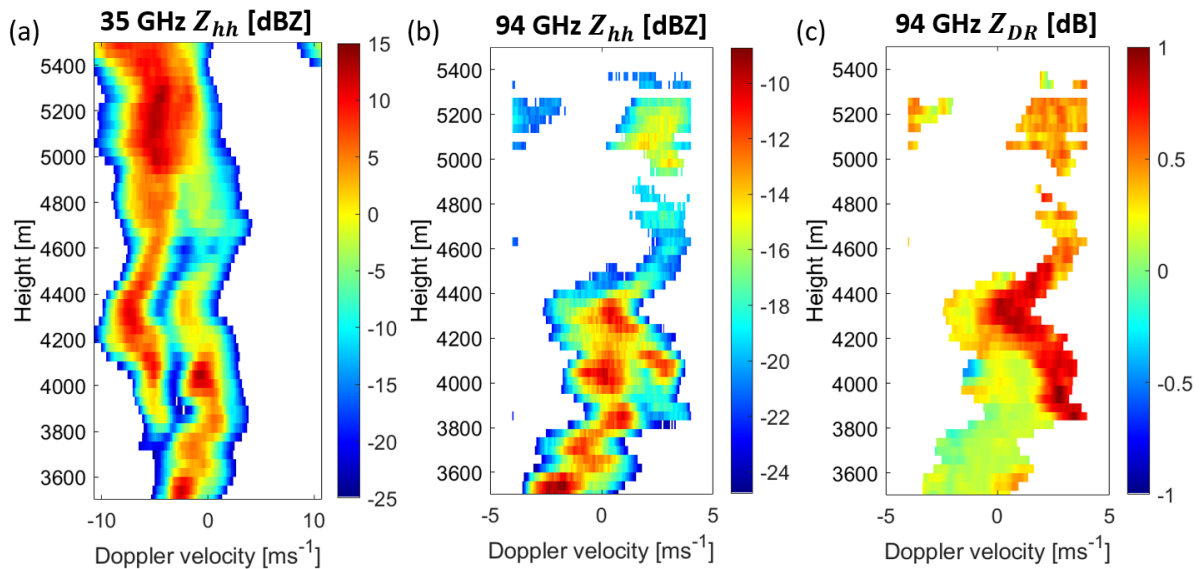


Figure 8.2: Equivalent reflectivity at (a) 35 GHz and (b) 94 GHz and (c) differential reflectivity at 94 GHz at 2021-06-18 17:23:04 UTC showing that part of the spectrum is alias at 94 GHz

In addition, the Mie scattering regime is reached when the particle diameter is larger than 0.8 mm at 94 GHz, while it only occurs for particles larger than 2.1 mm at 35 GHz. In Figure 8.3, the differential phase shift is almost constant over the entire Doppler spectrum, which indicates that all particles scatter in the Rayleigh scattering regime. However, the differential phase shift fluctuates at 94 GHz, showing that Mie scattering occurs. Mie scattering at 94 GHz would increase the difficulty in interpreting spectral polarimetric variables.

Due to the issues identified above, data from the 94 GHz radar were not be investigated in this study. In the following sections, the first and fourth cloud introduced in Chapter 4 are studied in depth since most parts of the clouds are visible to the radar at 35 GHz.

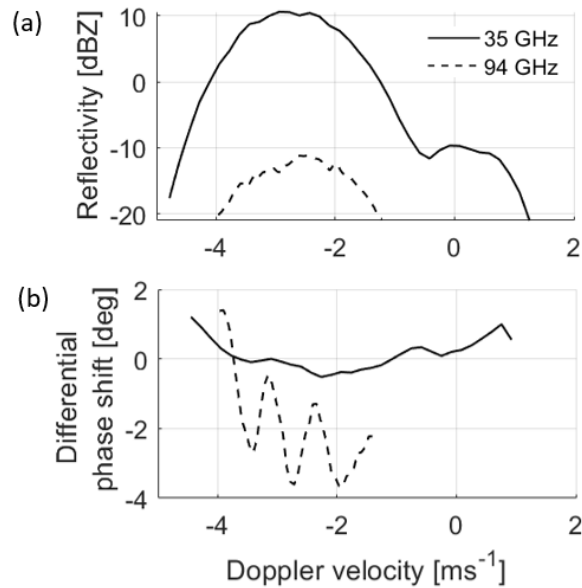


Figure 8.3: A spectrum of (a) reflectivity and (b) differential phase shift at 35 and 94 GHz at 2021-06-18 17:17:43 UTC at 5761 m showing that part of the spectrum is missed at 94 GHz and that Mie scattering is reached at 94 GHz but not at 35 GHz

8.1. First cloud

The first cloud came within the sight of the radar from 16:10 - 16:30 UTC. The centre of the cloud that contained lightning activities was more than 10 km away from the radar, thus the radar could only see the edge of the cloud. For an overview of the cloud including the radar images showing its motion, see Section 4.2.

8.1.1. Alignment of particles

From Figure 8.4(a) and (b), interesting polarimetric signatures can be found in the cloud. As shown in Figure 8.4(a), the Z_{DR} values in the cloud is close to zero and do not show much variations. However, from Figure 8.4(b), there is a cluster of negative K_{DP} values between 7600 m and 9300 m, which may indicate the alignment of non-spherical small ice particles but not large ones. If the small ice particles have sufficient number concentration, K_{DP} would become negative. However, since Z_{DR} carries reflectivity weighting, large ice particles that do not align with the electric field influence Z_{DR} strongly. This could explain why Z_{DR} does not show significant negative values.

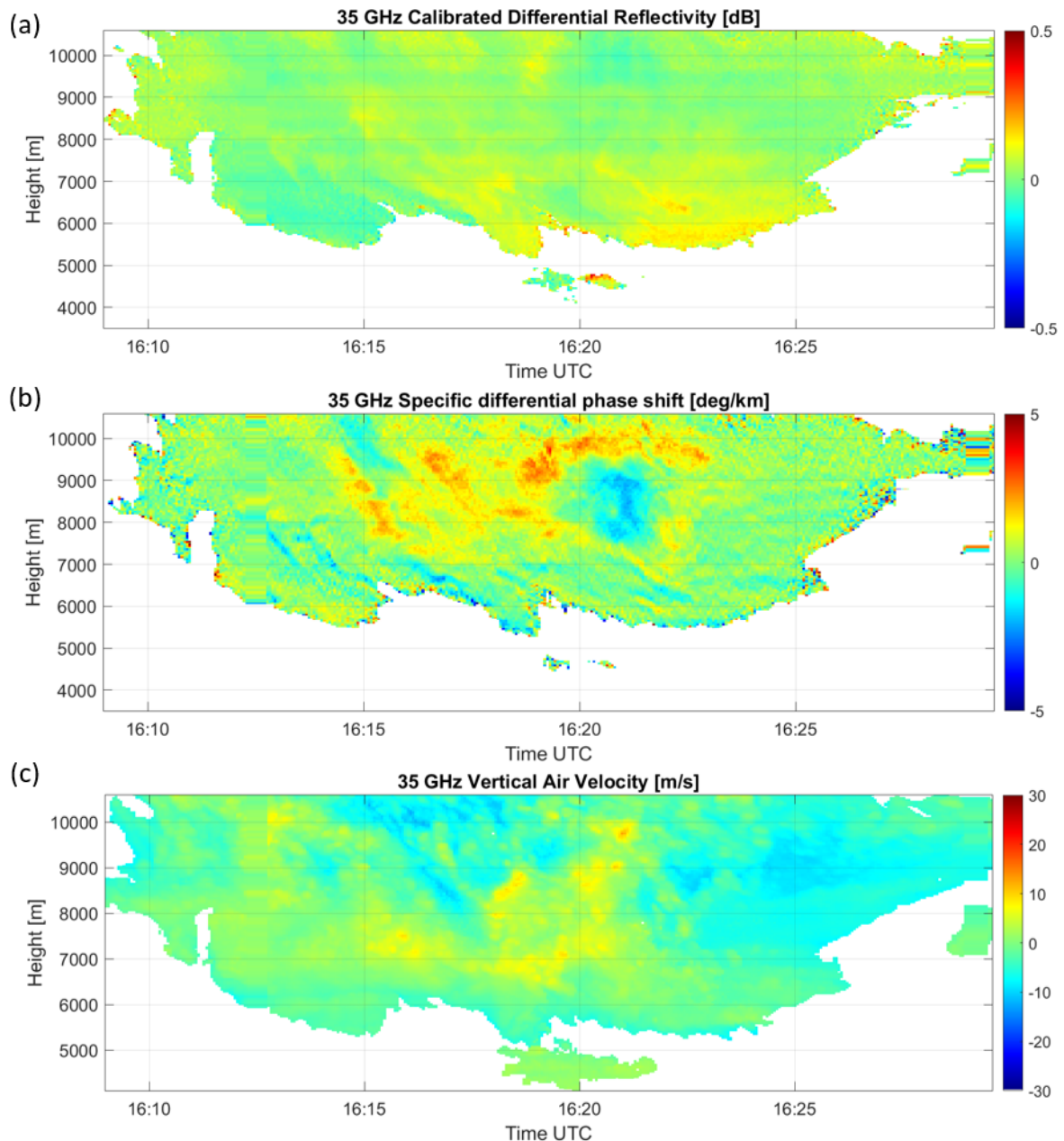


Figure 8.4: (a) Differential reflectivity, (b) specific differential phase shift and (c) vertical air velocity at 35 GHz of the first thunderstorm cloud on 2021-06-18 from 16:09 to 16:30 UTC

Figure 8.5 shows the spectral Z_{DR} across the period when negative K_{DP} is observed. At 16:18:59 UTC, the right part of the spectrum, which corresponds to small ice particles, has positive Z_{DR} , suggesting that the particles are horizontally aligned. However, at 16:21:05 UTC, the right part of the spectrum becomes slightly negative, suggesting that small ice particles are vertically aligned. At 16:22:34 UTC, Z_{DR} of the right part of the spectrum becomes positive again, which suggests that the particles return to being horizontally aligned. Figure 8.6 shows the mean Z_{DR} of the lightest 10% of the particles in each radar resolution volume at the three time instants. It is clear that from 7000 m to 9000 m, Z_{DR} of the lightest 10% particles are positive at 16:18:59 UTC and 16:22:34 UTC, and is negative at 16:21:05 UTC. The question is: are these negative Z_{DR} values associated with cloud electrification before lightning?

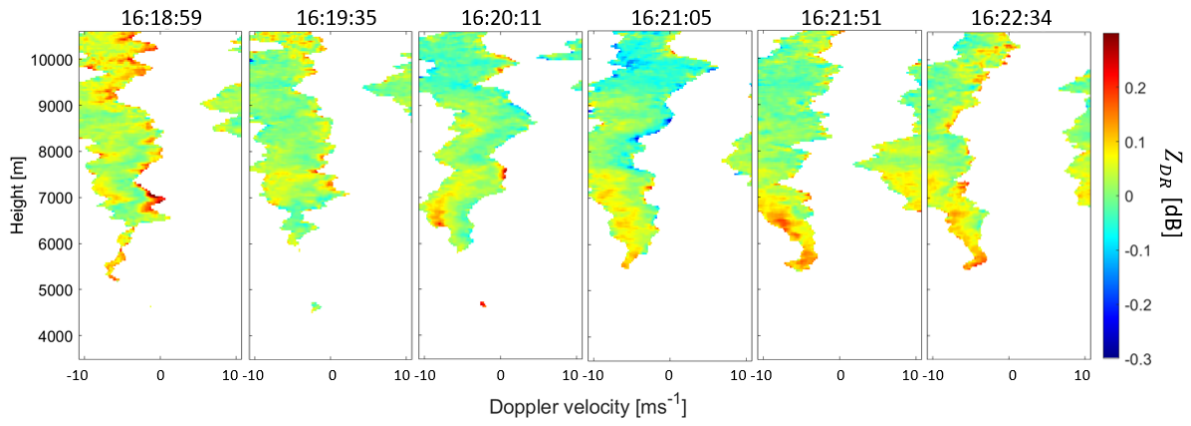


Figure 8.5: Spectral Z_{DR} on 2021-06-18 from 16:18:59 to 16:22:34 UTC at 35 GHz

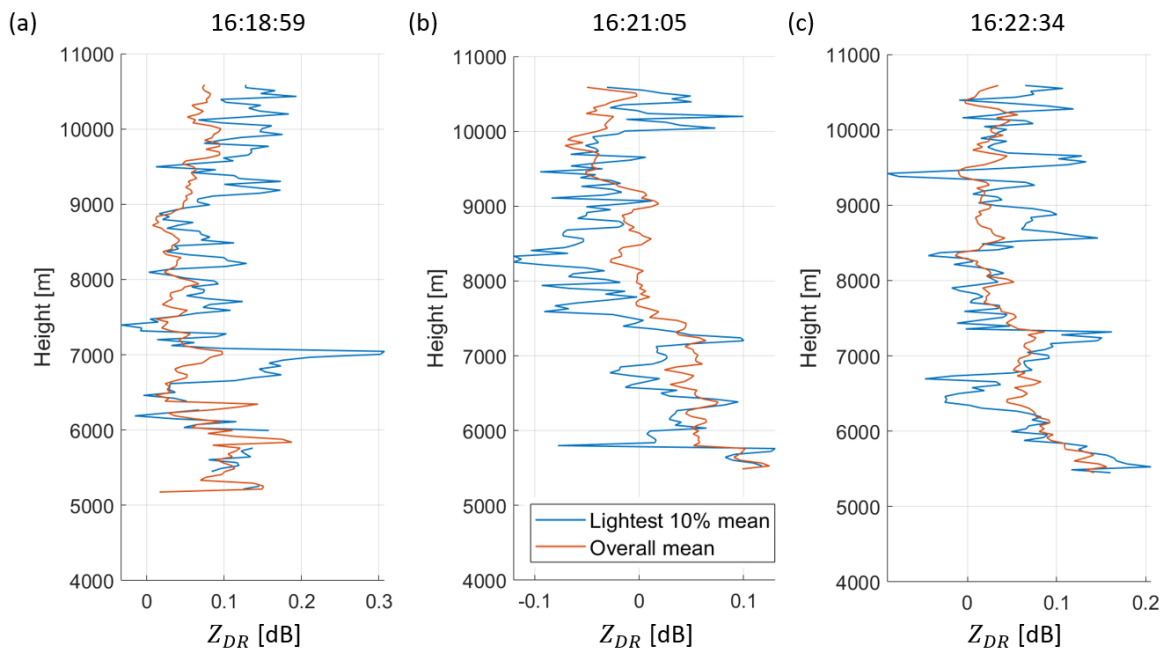


Figure 8.6: Mean Z_{DR} of all particles and the lightest 10% of the particles in a radar resolution volume at (a) 2021-06-18 16:18:59 UTC, (b) 16:21:05 UTC and (c) 16:22:34 UTC at 35 GHz

Our expectation is that particles align vertically before a lightning stroke, and return to horizontal alignment afterwards. However, the lightning strokes closest to the line of sight of the radar occurred at 16:20:17, 16:21:50 and 16:22:20 UTC (strokes number 9, 11, 14-17 in Figure 3 in Appendix B), but negative K_{DP} is observed continuously from 16:20:11 to 16:21:37 UTC. Negative K_{DP} appears at a distance of 7600 m to 9300 m away from the radar, but the lightning strokes occurred at least 13 km away from the radar. If the electric field that caused these lightning strokes is responsible for the alignment of particles observed, one would expect to observe negative K_{DP} also for ranges beyond 9000 m. Making a closer inspection with spectral Z_{DR} , negative Z_{DR} smaller than -0.1 dB are found beyond 9000 m from 16:20:21 to 16:21:15 UTC (Figure 8.9(b)), though more negative Z_{DR} are found on the left side of the spectrum that corresponds to large particles instead of the right side as expected (e.g. 16:21:01 UTC in Figure 8.9(b)).

The first inquiry is whether this could be caused by wind shear flipping the Doppler spectrum such that lighter particles appear on the left side. The horizontal and vertical velocities (V_h and V_v) of particles

are given by [40]:

$$V_h = v_H + \frac{sV_t^2}{g}, \quad (8.1)$$

$$V_v = -V_t, \quad (8.2)$$

where v_H is the horizontal wind speed, $s = \frac{dv_H}{dz}$ is the constant vertical wind shear, g is gravitational acceleration and V_t is the terminal velocity of the particle which depends on its size. For a radar looking at an elevation angle θ , the Doppler velocity is $V_v \sin \theta + V_h \cos \theta$. Without vertical wind shear, the Doppler spectrum will be shifted as a whole by v_H , with light particles remaining on the right side of the spectrum. If s is negative, since V_t increases with particle size, the left side of the spectrum would shift to the left more than the right side of the spectrum, thus the spectrum widens (Figure 8.7(b)). On the other hand, if s is positive, the left side of the spectrum would shift to the right more than the right side of the spectrum (Figure 8.7(c)). If the right shift of the left side of the spectrum due to the term $\frac{sV_t^2}{g}$ is larger than the original spectrum width, the spectrum would be flipped (Figure 8.7(d)). Assuming a spectrum width of 10 m s^{-1} and taking the upper bound of the terminal velocity of plates, i.e. $V_t = 2 \text{ m s}^{-1}$ [41], for a radar looking at 45° , the vertical wind shear required to flip the Doppler spectrum is approximately $35 \text{ m s}^{-1} \text{ m}^{-1}$. However, according to the ECMWF Integrated Forecast System output over Cabauw [33] shown in Figure 8.8(c), this is much larger than the strongest vertical wind shear of $4 \text{ m s}^{-1} \text{ km}^{-1}$ from 7500 m to 10000 m. Therefore, it is unlikely that the negative Z_{DR} on the left side of the spectrum is due to flipping of the spectrum caused by wind shear.

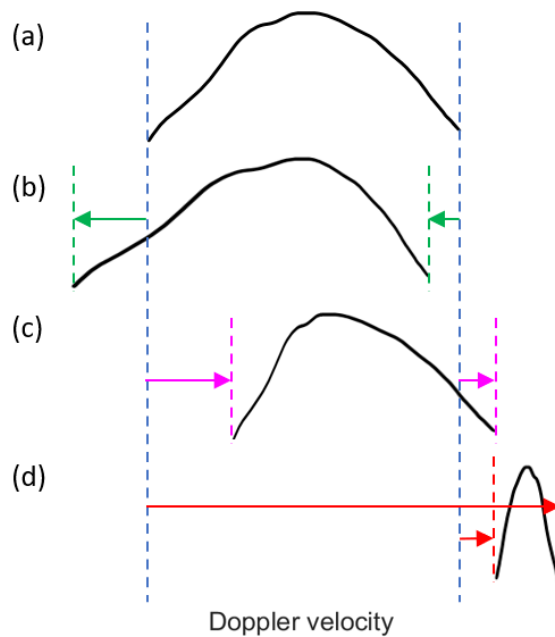


Figure 8.7: A figure to illustrate effects of the sign of vertical wind shear s on the Doppler spectrum: (a) Doppler spectrum when there is no shear (b) Doppler spectrum widens when s is negative (c) Doppler spectrum may become narrow when s is positive (d) Doppler spectrum may flip when s is positive and $\frac{sV_t^2}{g}$ is larger than the original spectrum width

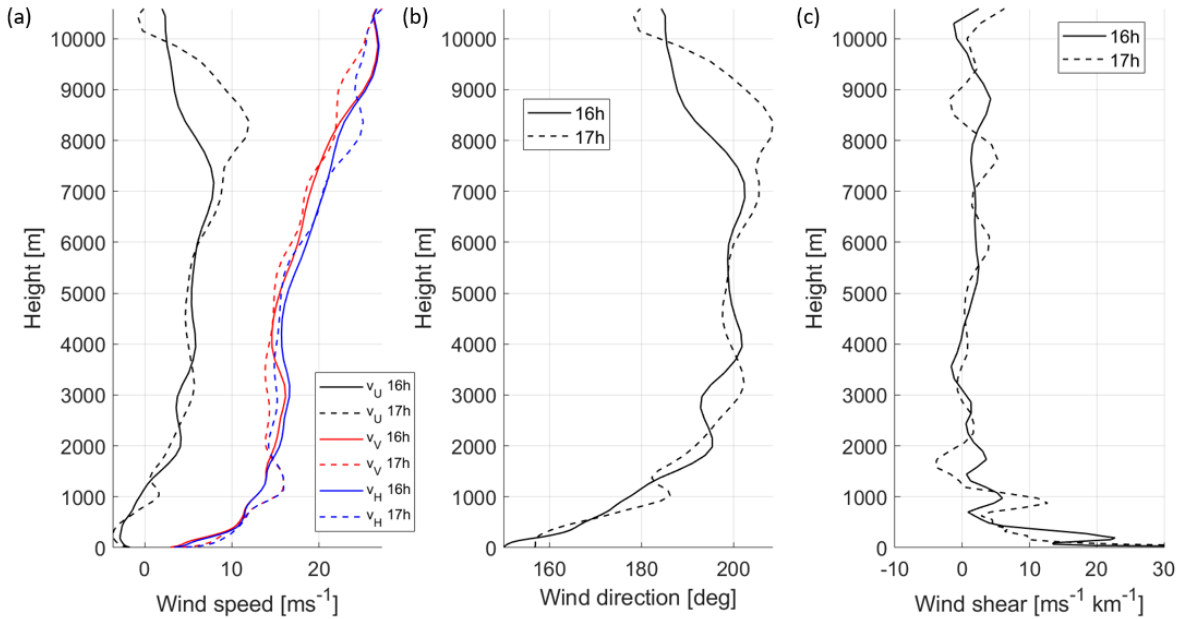


Figure 8.8: (a) Mean horizontal wind, (b) horizontal wind direction relative to North and (c) vertical wind shear at 2021-06-18 16:00 and 17:00 UTC

If the negative Z_{DR} values are caused by vertical alignment of particles by the electric fields, one possible explanation for this is that the axis ratios of small particles are close to one, thus their Z_{DR} is close to zero. Meanwhile, large ice chains may be formed under an electric field [17] as mentioned in Section 2.2. Z_{DR} could become negative if these chains are vertically aligned. Nonetheless, the most negative Z_{DR} is found at 16:21:01 UTC, which is not exactly the moment before any lightning strokes. This could be because the region with chains and sufficiently strong electric field had moved away from the line of sight of the radar when lightning occurred, or that the electric field was not strong enough to trigger lightning.

The negative Z_{DR} values on the right edge of the spectra at around 7500 m to 9000 m also do not occur right before any lightning strokes. Although there is a lightning at a perpendicular distance of 13 km away from the radar at 16:21:09 UTC (stroke number 5 in Figure 3 in Appendix B), from the literature, electric field in thunderstorm clouds reduces significantly over 5 km [8], thus it is unlikely that the alignment of particles observed is caused by the build up of electric field that generated the lightning stroke. There is another lightning at a perpendicular distance of around 11 km away from the radar at 16:21:50 UTC (stroke number 7 in Figure 3 in Appendix B). It is possible that the electric field associated with this stroke caused the vertical alignment of particles observed, but the relationship is hard to prove since the spatial and temporal variation of the electric field is unknown. The next lightning at 16:29:08 UTC at a perpendicular distance of around 11.5 km (stroke number 8 in Figure 4 in Appendix B) occurred 8 minutes after negative Z_{DR} is observed. This is a rather long period of time compared to common durations of charging cycles [6, 7], thus it is unlikely that it is associated with the observed negative Z_{DR} .

Meanwhile, one should not rule out other possible causes of vertical alignment of particles. As suggested by Brussaard [26], canting of particles may occur when there is vertical wind shear. To estimate the largest possible canting angle, terminal velocity V_t is taken to be 2 m s⁻¹ [41] and $s = \frac{dv_H}{dz} = 4$ m s⁻¹ according to the ECMWF Integrated Forecast System output [33] shown in Figure 8.8(c). Using Equation 2.1, the corresponding canting angle is 0.05°, which is insignificant. Therefore, wind shear is not likely the cause of negative Z_{DR} in this case.

In conclusion, the vertical alignment of particles observed in the first cloud could be due to electric field, though the electric field may not be strong enough to trigger lightning, or there are lightnings that are not measured by the lightning sensor.

8.1.2. Supercooled liquid water

Another interesting feature observed in this cloud is the possibility of supercooled liquid water. From 16:20:21 to 16:21:15 UTC, spectograms of reflectivity show a separate mode of particles on the right side of the spectrum at around 6000 m (see Figure 8.9(a)). From Figure 8.9(b), Z_{DR} of this mode of particles is close to zero. Figure 8.10 shows the time series of spectral reflectivity and spectral Z_{DR} at 5916 m. A small peak at Doppler velocity of around -4 to -3 m s^{-1} is consistently present. The Z_{DR} of this mode of particles is lower than the left part of the spectrum, with values of around -1 to 0 dB. By manually identifying the part of the Doppler spectrum that may contain supercooled liquid water for 139 range bins over 16 time steps, it was found that the average Z_{DR} is -0.0370 dB. Recall that the error of Z_{DR} after calibration is 0.051 dB and knowing that small supercooled liquid water droplets are nearly spherical and have a differential reflectivity of 0 dB, there is a high chance that there is indeed supercooled liquid water present in the cloud. This is further supported by the liquid water path measured by the cloud radar. Although the liquid water paths measured at 35 GHz and 94 GHz have unknown bias, it can be seen from Figure 8.11 that the trend at both frequencies agree with each other. From 16:20:21 to 16:21:15 UTC (marked by the red lines in Figure 8.11), there is indeed a peak in liquid water path, which agrees with the conclusion that supercooled liquid water is present in the cloud. Supercooled liquid water plays a role in the non-inductive charging mechanism as it is needed for riming to occur, which in turn forms graupel that collide with ice crystals to produce charges. Nonetheless, the radar was not able to look at the lower part of the cloud, thus it is unknown whether graupel is formed in this case.

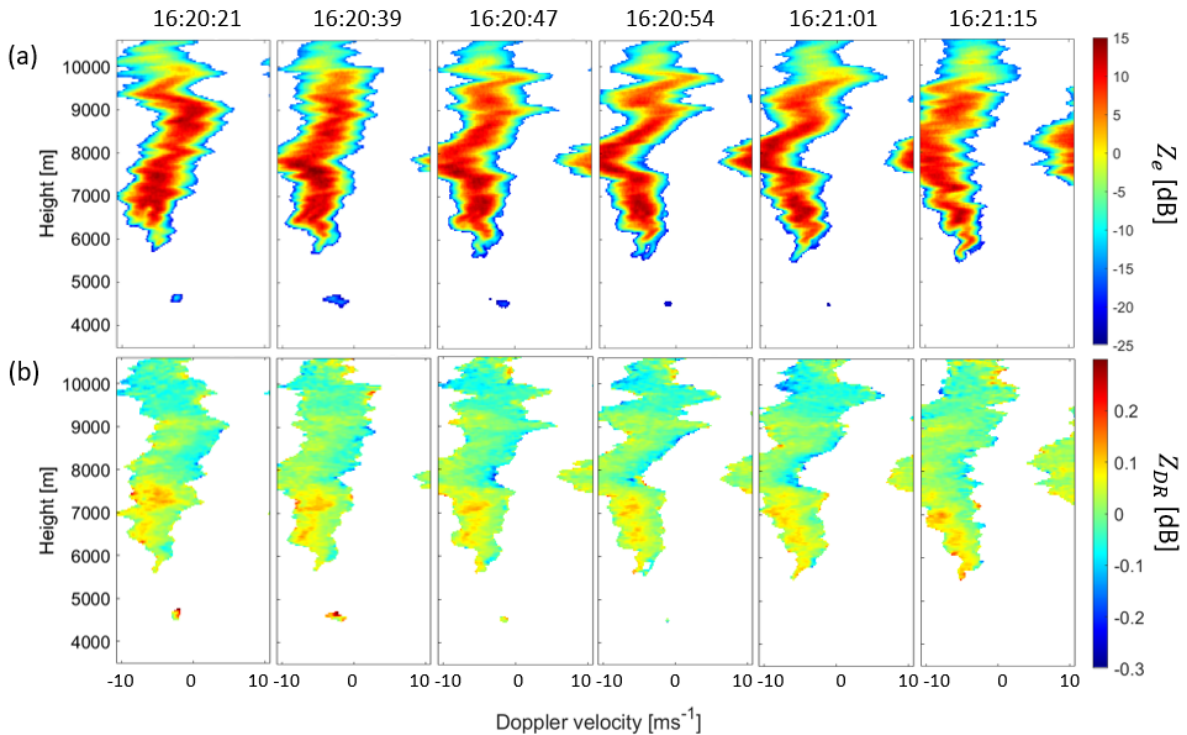


Figure 8.9: (a) Spectral reflectivity and (b) spectral Z_{DR} on 2021-06-18 from 16:20:21 to 16:21:15 UTC at 35 GHz showing presence of supercooled liquid water near 6000 m

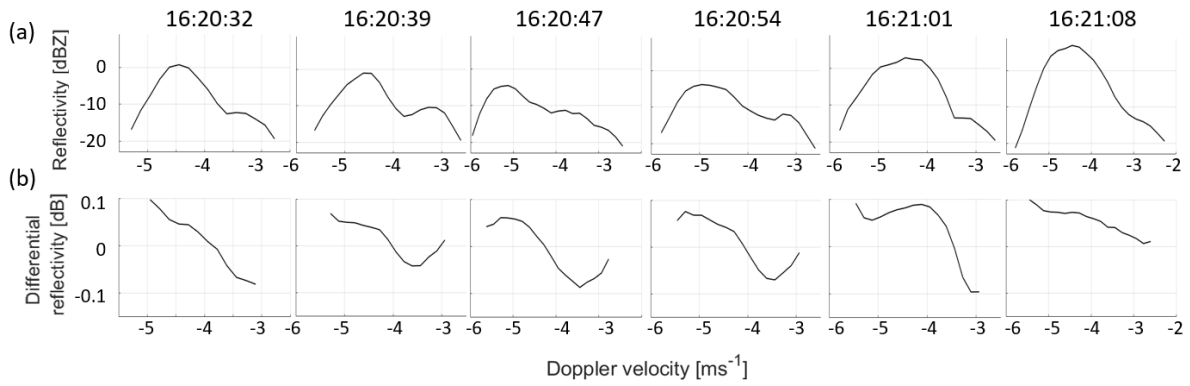


Figure 8.10: (a) Spectral reflectivity and (b) spectral Z_{DR} on 2021-06-18 from 16:20:32 to 16:21:08 UTC at 35 GHz at 5916 m

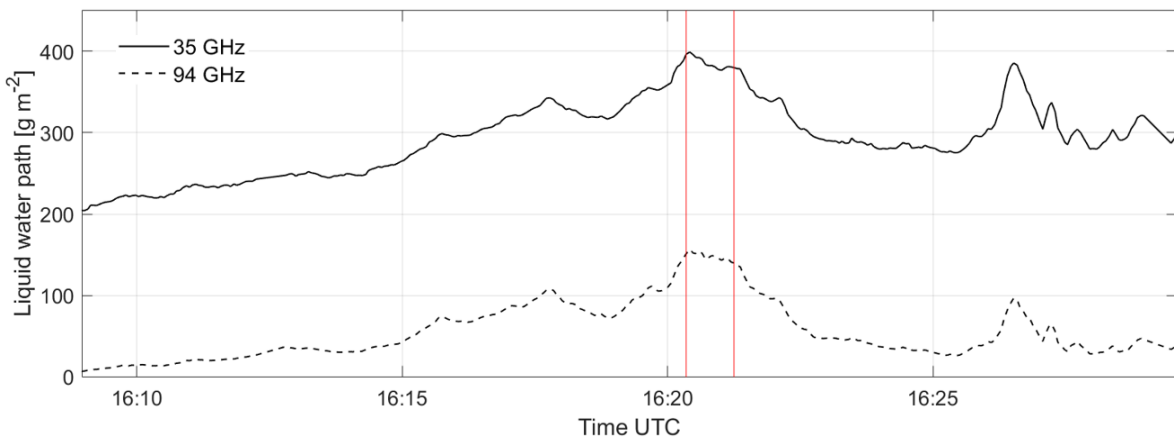


Figure 8.11: Liquid water path of the first cloud measured at 35 GHz (solid line) and 94 GHz (dashed line). Time interval from 16:20:21 to 16:21:15 UTC is marked by red lines

8.1.3. Updrafts and downdrafts

Although the Delft radar was located at Cabauw and made measurements looking towards the zenith during this thunderstorm, since the thunderstorm clouds did not pass directly above the radar, the data from the Delft radar cannot be used to investigate the updraft and downdraft patterns in the clouds. Instead, the mean vertical velocity in the cloud is derived by combining mean Doppler velocity measured by the Cabauw radar and the mean horizontal wind estimated by the ECMWF Integrated Forecast System as described in Section 5.4.

From Figure 4.4(c), the first cloud mainly shows downdrafts from 16:15 to 16:18 UTC and after 16:22 UTC. Referring to Figure 4.5, in these periods, the radar was looking at the edge of the thunderstorm cloud. Therefore, the radar did not see regions with strong updrafts which is normally found in the core of thunderstorm clouds, but observed downdrafts outside the core instead. From 16:18 to 16:22 UTC, updrafts of up to 12 m s^{-1} are observed, which could be because the core of the thunderstorm cloud is closer to the line of sight of the radar. The mean vertical velocity is not uniform within the cloud, which suggests that there might be a lot of turbulence.

8.2. Fourth cloud

The fourth cloud came within the sight of the radar from 17:15 to 17:40 UTC. The part of the cloud that passed through the line of sight of the radar from 17:15 to 17:20 UTC did not contain active lightning activities. From 17:20 to 17:35 UTC, the part of the cloud with the most active lightning activities passed through the line of sight of the radar. Afterwards, lightning activities ceased and the cloud moved away

from the line of sight of the radar. For an overview of the cloud including the radar images showing its motion, see Section 4.2.

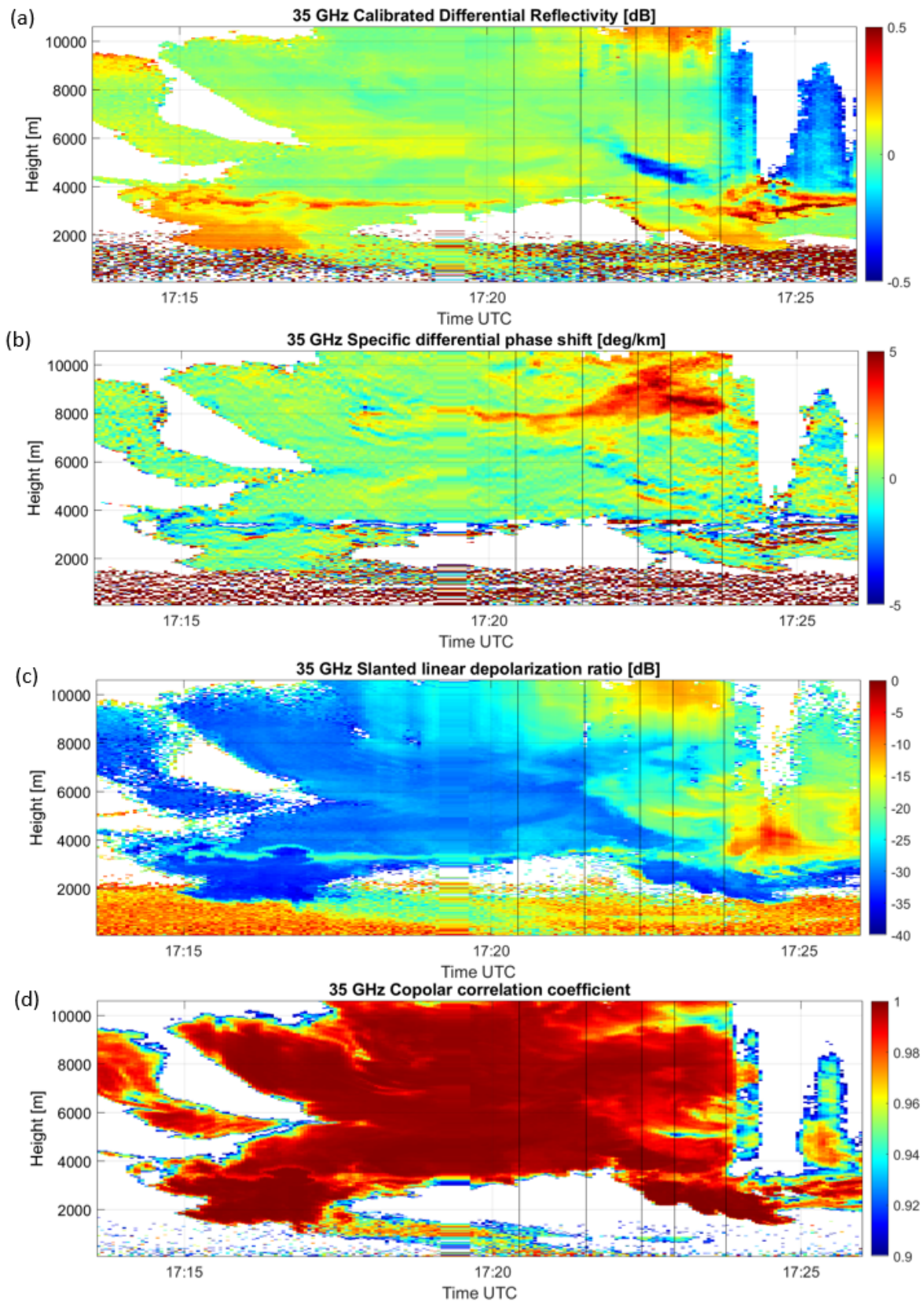


Figure 8.12: (a) Differential reflectivity, (b) specific differential phase shift, (c) slanted linear depolarisation ratio and (d) co-polar correlation coefficient at 35 GHz of the fourth thunderstorm cloud on 2021-06-18 from 17:14 to 16:26 UTC. Vertical black lines indicate time instants 17:20:26, 17:21:31, 17:22:25, 17:22:57 and 17:23:47 UTC

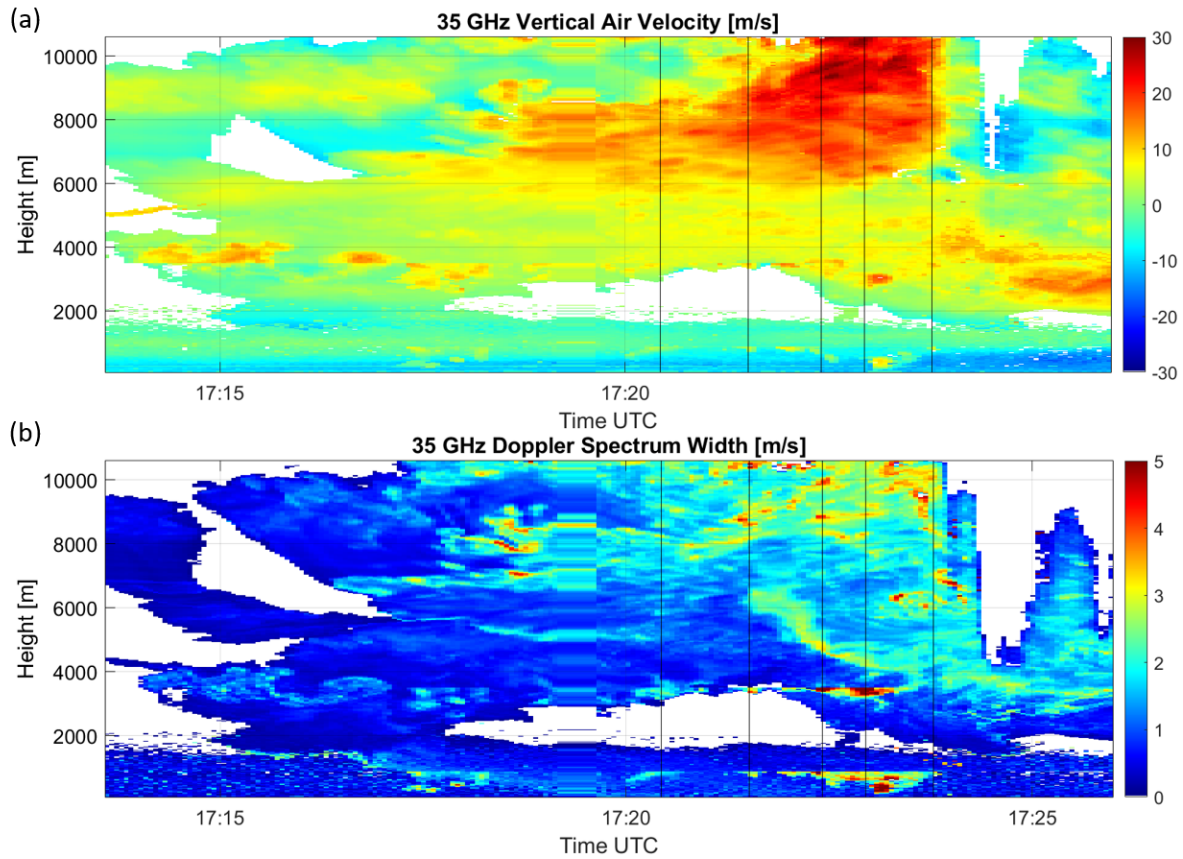


Figure 8.13: (a) Vertical air velocity and (b) Doppler spectrum width at 35 GHz of the fourth thunderstorm cloud on 2021-06-18 from 17:14 to 17:26 UTC. Vertical black lines indicate time instants 17:20:26, 17:21:31, 17:22:25, 17:22:57 and 17:23:47 UTC

8.2.1. Evidence of graupel

According to Figure 8.12(a), from around 17:22 UTC, a region with large negative differential reflectivity appears at around 4000 m to 6000 m. From Figure 8.12(c) and (d), this region has enhanced slanted linear depolarisation ratio and reduced co-polar correlation coefficient. Inspecting the spectograms during this period, it is found that from 17:21:24 UTC, a separate particle mode negative Z_{DR} is observed on the left side of the Doppler spectrum at around 6000 m as shown in Figure 8.16(a). The reflectivity of this mode grew with time and it descended to around 4300 m near 17:24 UTC. The spectral reflectivity and Z_{DR} of one instant where this mode is present is shown in Figure 8.14(a) and (b). When negative Z_{DR} appears on the left part of the spectrum, Z_{DR} of the right part of the spectrum is close to zero. Since small particles are more easily aligned by an electric field and they are not aligned in this case, the negative Z_{DR} in the left part of the spectrum might be due to the presence of conical graupel [37].

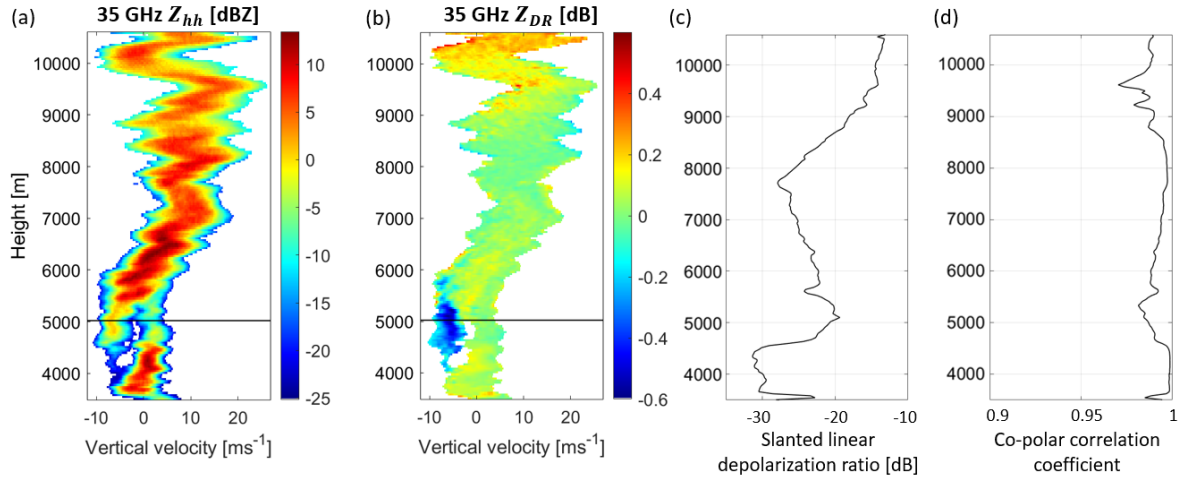


Figure 8.14: Spectrograms of (a) equivalent reflectivity, (b) differential reflectivity, (c) slanted linear depolarisation ratio and (d) co-polar correlation coefficient at 35 GHz at 17:22:25 UTC. Spectra at 5021 m indicated by black horizontal line in (a) and (b) are shown in Figure 8.15(d-f)

The Doppler spectra of reflectivity, Z_{DR} and Ψ_{DP} at 5021 m at the instant shown in Figure 8.14 are shown in Figure 8.15(d-f). The spectral differential phase shift deviates from the Rayleigh plateau at about -2 m s^{-1} , signifying Mie scattering. To ensure correct interpretation of Z_{DR} , scattering simulation is carried out using typical parameters of conical graupel. From the literature, the theoretical axis ratio of conical graupel is 1.05 and the density is 0.55 g cm^{-3} [41], which is equivalent to an ice fraction of 0.6. The diameter of conical graupel is typically 2 to 8 mm [11]. The canting angle follows a Gaussian distribution with a zero mean and a standard deviation of 30° [35]. Conical shape is not supported by the simulation code used, thus the shape is assumed to be spheroidal. The simulated Z_{DR} and δ_{co} are shown in Figure 8.15(b-c). In Rayleigh scattering regime, the differential reflectivity of conical graupel is negative. Both Z_{DR} and δ_{co} decrease when the Mie scattering regime is reached. δ_{co} reaches a minimum earlier than Z_{DR} . As particle size increases further, δ_{co} increases sharply and becomes positive, during which Z_{DR} reaches its minimum. Afterwards, δ_{co} reaches a local maximum and decreases slightly before increasing again. Z_{DR} increases and continues to oscillate. Similar behaviours are observed in the Doppler spectra at 5021 m at 17:22:25 UTC (Figure 8.15(e-f)). Ψ_{DP} reaches a minimum at -3.9 m s^{-1} and increases sharply as particle size further increases. Z_{DR} reaches a minimum at -5.0 m s^{-1} while Ψ_{DP} is still increasing. Afterwards, Ψ_{DP} reaches a maximum and decreases slightly, while Z_{DR} continues to increase. The minimum of reflectivity in Figure 8.15(d) is not located at the Mie minimum according to the simulation (Figure 8.15(a)). This suggests that the two peaks in spectral reflectivity represent two particle populations. Comparing the simulation results and the observed spectra, the conical graupel present is about 3 to 5.2 mm in diameter.

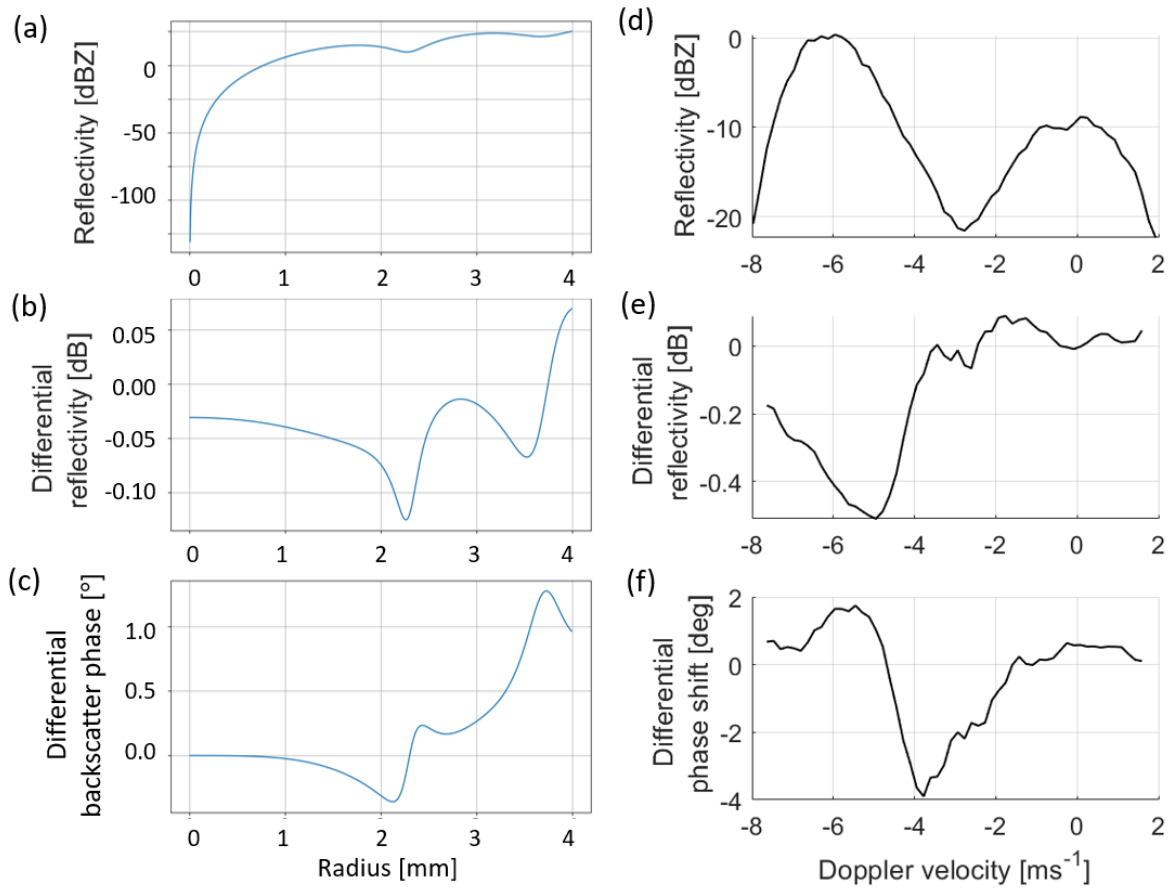


Figure 8.15: (a-c) Simulated reflectivity, differential reflectivity and differential backscatter phase of conical graupel. (d-f) Spectral reflectivity, differential reflectivity and differential phase shift at 5021 m at 17:22:25 UTC

From 4400 m to 5600 m where the negative Z_{DR} signature of graupel is the most prominent, SL_{DR} increases and ρ_{hv} decreases as shown in Figure 8.14(c) and (d). This is likely because the radar resolution volume contains a variety of hydrometeors, including conical graupel and other small ice particles. Unfortunately, it is challenging to look for supercooled liquid water in this case since there is liquid water at the bottom of the cloud below the 0°C level at around 4000 m, which means it is impossible to identify supercooled liquid water using liquid water path. It is worth noting from Figure 8.14(a) and (b) that the population of graupel ends at around 4000 m. Since the radar is looking at an elevation angle of 45° , this suggests that graupel is not present closer than 4000 m from the radar, which means the region with graupel is localised in the thunderstorm cloud.

In Figure 8.14(a) and (b), the spectrograms are plotted with vertical velocity instead of Doppler velocity as in other spectrograms in this report. The vertical velocity is estimated by assuming uniform horizontal wind predicted by the ECMWF model. By plotting with vertical velocity, it is clear that the graupel are falling, while smaller ice particles on the right with positive vertical velocities are brought upwards by updrafts. As the falling graupel collide with the rising ice particles, charges can be produced. From the literature, if temperature is below -10°C , graupel will become negatively charged and vice versa [9]. From the temperature profile measured by the weather station attached to the cloud radar, the temperature is -10°C at around 5550 m. This means that above 5550 m, falling graupel that collides with rising ice particles becomes negatively charged, forming a negative charge region in the cloud. Meanwhile, small ice particles that gained positive charges due to collisions are brought upwards by updrafts, so the upper part of the cloud is positively charged. Below 5550 m where temperature is above -10°C , falling graupel acquires positive charge, causing the cloud base to become positively charged. This could result in the typical tripolar structure of thunderstorm clouds. Nonetheless, the temperature profile inside the thunderstorm cloud may be different from the temperature profile measured by the weather

station looking towards the zenith, so the actual charge distribution in the cloud may be different.

8.2.2. Alignment of particles

At 17:21:32 UTC, a lightning of 5 kA occurred around 8.5 km away on the line of sight of the radar (stroke number 7 in Figure 6 in Appendix B). This is a cloud-to-cloud lightning with medium strength. One second before that, negative Z_{DR} values are observed for large and small particles from 8000 m to 9000 m as shown in Figure 8.16(a). The minimum value is around -0.40 dB on the left side of the spectrum and -0.36 dB on the right side of the spectrum. Negative Z_{DR} values disappeared at 17:21:38 UTC. Note that the timestamp of the cloud radar correspond to the end of the measurement after all chirp sequences have been transmitted, therefore the spectrum at 17:21:34 UTC may contain backscattered signals before the lightning, which could explain why negative Z_{DR} is still observed. Since the location and time of negative Z_{DR} agree well with that of the lightning stroke and there are no other strokes close to this one in time and space, what is observed here is likely the vertical alignment and relaxation of particles right before and after a lightning stroke.

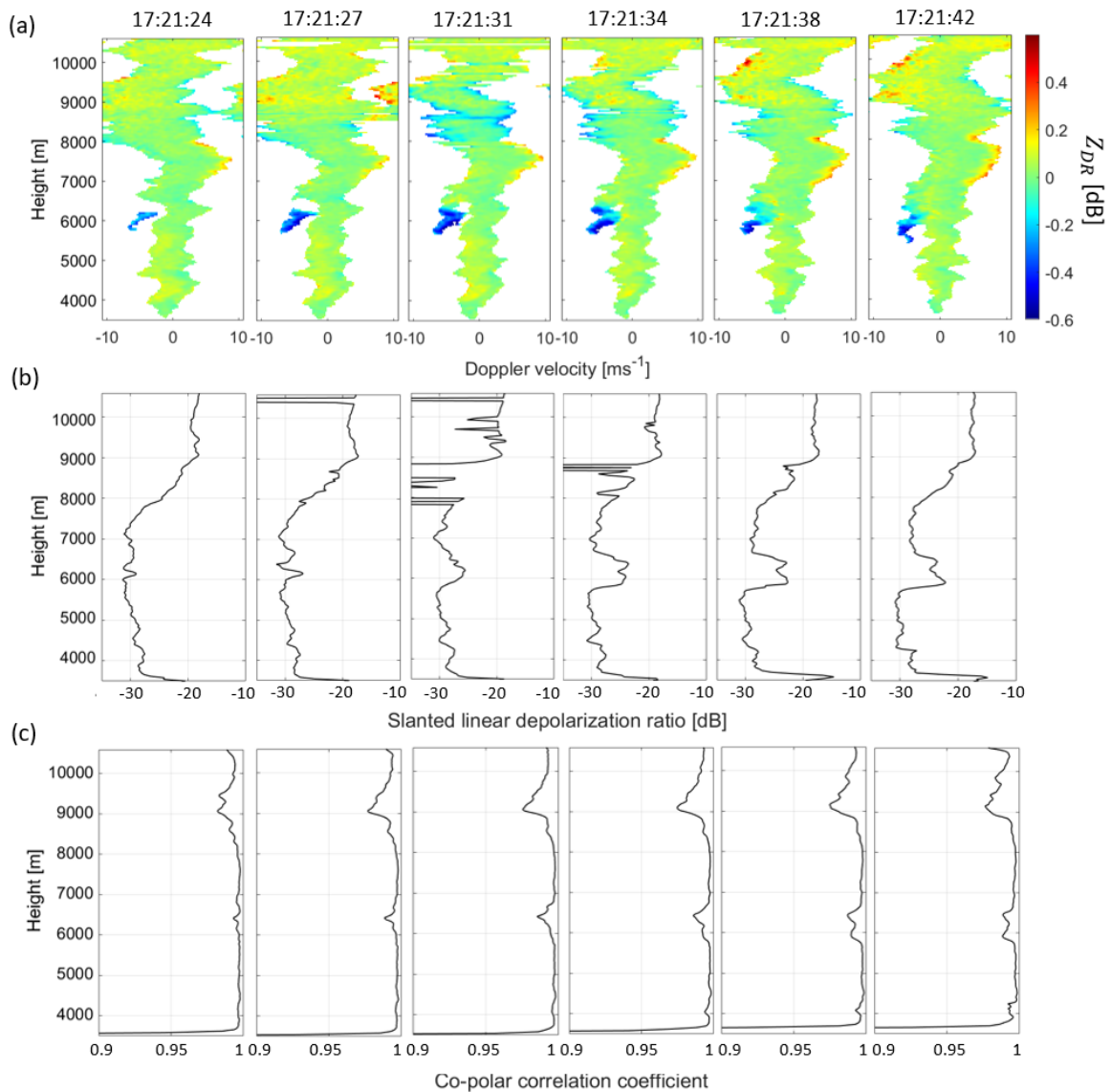


Figure 8.16: (a) Differential reflectivity (b) slanted linear depolarisation ratio and (c) co-polar correlation coefficient before and after lightning stroke (5 kA) at 17:21:32 UTC (stroke number 7 in Figure 6 in Appendix B)

The SL_{DR} across this lightning stroke also shows interesting signature. As shown in Figure 8.16(b),

at 17:21:31 UTC, SL_{DR} from 8000 m to 9000 m suddenly decreases significantly to -100 dB and only recovered at 17:21:38 UTC. During this period, ρ_{hv} does not change significantly and is high (Figure 8.16(c)), which means that the decrease in SL_{DR} is not due to low SNR. One possible cause is that almost all crystals are aligned right before the lightning close to the location of lightning, which leads to low canting variance. As a result, there is a sudden decrease in SL_{DR} . Nonetheless, the SL_{DR} values taken from Level 1 data are not verified. While it is possible that values of -100 dB are due to slanted linear depolarisation ratio close to zero in linear scale, which could represent low canting variance, it is still uncertain whether they could be due to errors in measurement or data processing.

At 17:20:27 UTC, a strong cloud-to-cloud lightning of -18 kA occurred at a perpendicular distance of around 3 km away from the radar (stroke number 92 in Figure 7 in Appendix B), but it is about 5.5 km away from the line of sight of the radar. Despite being quite distant from the line of sight of the radar, negative Z_{DR} values are observed for small particles from 5200 m to 5700 m before the lightning as shown in Figure 8.17, which is probably due to the large magnitude of the electric field that generated the strong lightning. The minimum Z_{DR} observed is around -0.36 dB, which is similar to that observed in the previous case. Also similar to the previous case is that Z_{DR} values returned to the level before the lightning about 4 seconds after the lightning from 17:20:31 UTC onward. However, unlike the previous case, negative Z_{DR} is only found for small particles, which may be because electric field strength reduces with distance from the lightning, thus it is not strong enough to align larger and heavier particles vertically. It is difficult to pinpoint when negative Z_{DR} first emerged due to this particular lightning stroke. Slightly negative Z_{DR} of about -0.16 dB can be found for light particles as early as 17:19:39 UTC, which could be due to other lightning in the same cloud. Although the same part of the spectrum shows positive Z_{DR} instead one timestamp before at 17:19:09 UTC, a closer inspection reveals that it may be due to a different population of particles.

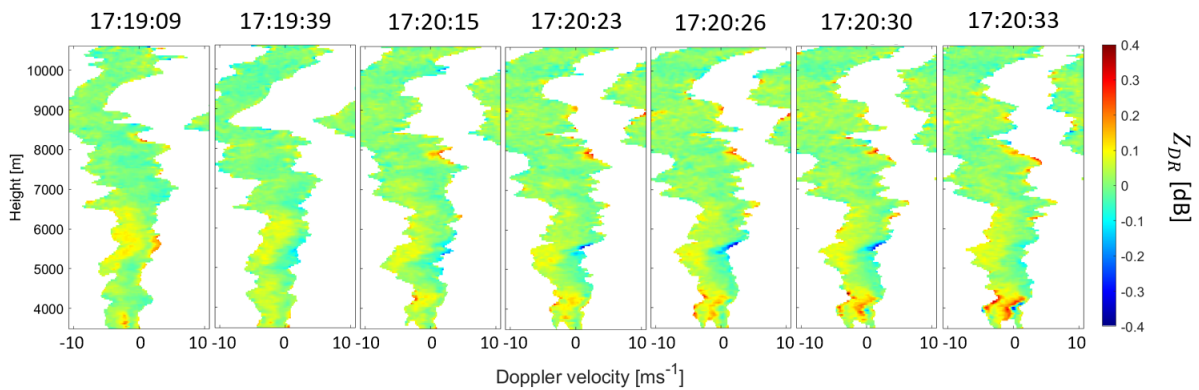


Figure 8.17: Spectral differential reflectivity before and after a strong lightning stroke (-18 kA) at 17:20:27 UTC (stroke number 92 in Figure 7 in Appendix B)

Comparing the spectral reflectivity at 17:19:09 and 17:19:39 UTC in Figure 8.18 with the spectral differential reflectivity in Figure 8.17, negative Z_{DR} from 5000 m to 6000 m at 17:19:39 UTC likely belongs to particles associated with the upper part of the spectrum, while positive Z_{DR} at the same height at 17:19:09 UTC belongs to particles associated with the lower part of the spectrum. Since the two populations of particles may overlap, small negative Z_{DR} values may be masked by positive values. Therefore, it is not possible to conclude that no negative Z_{DR} values or no vertical alignment of particles are found before 17:19:39 UTC.

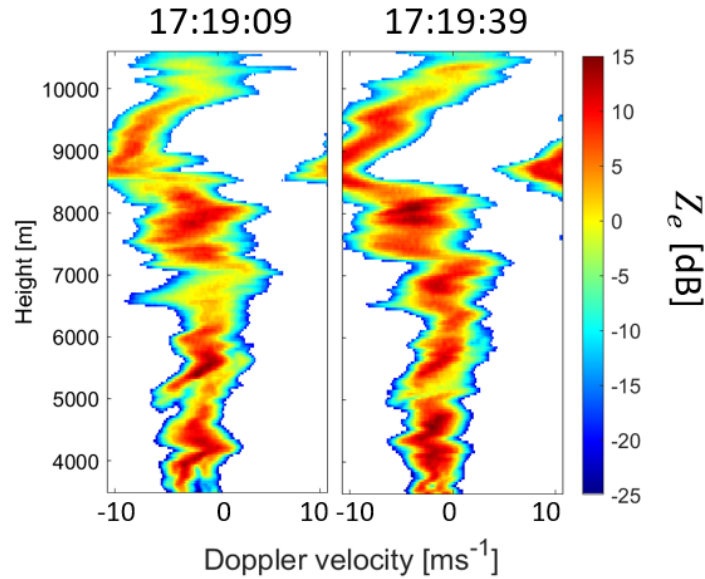


Figure 8.18: Spectral reflectivity at 17:19:09 and 17:19:39 UTC

Also, unlike the previous case, right before the lightning at 17:20:27 UTC, SL_{DR} does not show a sudden decrease. This could be because the lightning occurred some distance away from the line of sight of the radar. Therefore, not all particles are aligned, thus SL_{DR} did not decrease significantly.

From 17:23:40 UTC, differential reflectivity becomes negative for the entire Doppler spectrum above 7000 m, such as the spectrum at 17:23:47 UTC shown in Figure 8.20(b). This could be due to vertical alignment of all particles by strong cloud electric field. However, from Figure 4.1, most of the thunderstorm cloud above 4000 m from 17:24 to 17:29 UTC is not visible to the radar due to large attenuation. There is also significant amount of liquid water below the cloud, leading to differential attenuation of horizontal and vertical polarizations, which may cause Z_{DR} values to be negatively biased. An evidence of differential attenuation is that Z_{DR} values become more negative as the thickness of the layer that contains liquid water increases. Also, many lightnings occur close to each other in time during this period, so it is impossible to isolate each lightning stroke and analyse the changes before and after each stroke. These limit the investigation on the period with the most intense lightning activities.

8.2.3. Strong updraft and turbulence

As shown in Figure 8.13(a), from 17:18 to 17:24 UTC, vertical air velocity is large and positive ($15\text{--}30\text{ m s}^{-1}$) above 7000 m, indicating strong updraft in the cloud. From Figure 8.13(b), the top of the cloud above 6000 m has large Doppler spectrum width of 3 to 4 m s^{-1} . In stratiform rain, the cloud top usually has low spectrum width since small and light particles have a small range of fall velocities. The large spectrum width observed here might be due to strong turbulence in the thunderstorm cloud. Slanted linear depolarisation ratio is high and co-polar correlation coefficient is low in this region, which could be the result of large canting variance of particles due to strong turbulence.

From 17:22:30 to 17:24:00 UTC from 5000 m to 7000 m, there are three co-locating peaks of SL_{DR} and troughs of ρ_{hv} . The lowest peak at around 5000 m is located just above the graupel layer, such as in the example shown in Figure 8.19 where the peak is found at 5060 m. From Figure 8.19(h), the vertical air velocity does not vary much near this height, so the sudden increase in SL_{DR} and decrease in ρ_{hv} may not due to increased canting variance due to turbulence. Meanwhile, the spectral Z_{DR} where the peak of SL_{DR} and ρ_{hv} is located shows multiple peaks (Figure 8.19(d)). This could be due to a variety of hydrometeors with different axis ratios that are the seeds for forming graupel. Therefore, the high SL_{DR} and low ρ_{hv} in this case are likely due to co-existence of different types of particles.

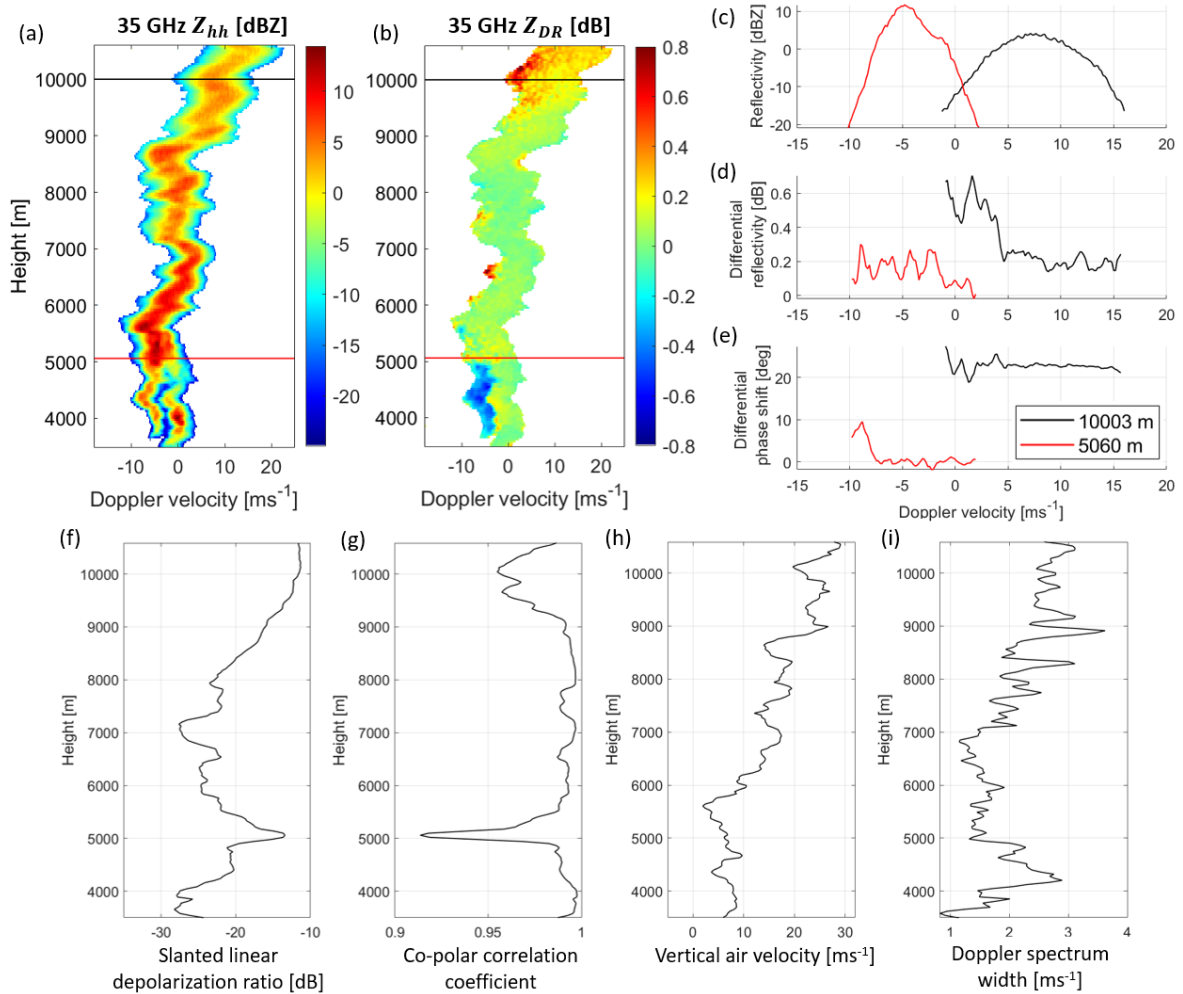


Figure 8.19: 2021-06-18 17:22:57 UTC where the lowest peak of SL_{DR} and ρ_{hv} is observed (a-b) Spectrograms of reflectivity and differential reflectivity (c-e) spectra of reflectivity, Z_{DR} and Ψ_{DP} at 5060 m (f-i) profiles of SL_{DR} , ρ_{hv} , vertical air velocity and Doppler spectrum width

The middle and highest peaks of SL_{DR} and ρ_{hv} are found at around 5900 m and 6400 m, such as in the example shown in Figure 8.20. From Figure 8.20(h), vertical air velocity changes sharply at these heights, which can produce strong turbulence. Therefore, the sudden increase in SL_{DR} and decrease in ρ_{hv} may be due to increased canting variance under turbulence. With strong turbulence, the Doppler spectra is no longer ordered with small particles on the right and large particles on the left because particles with different sizes are mixed.

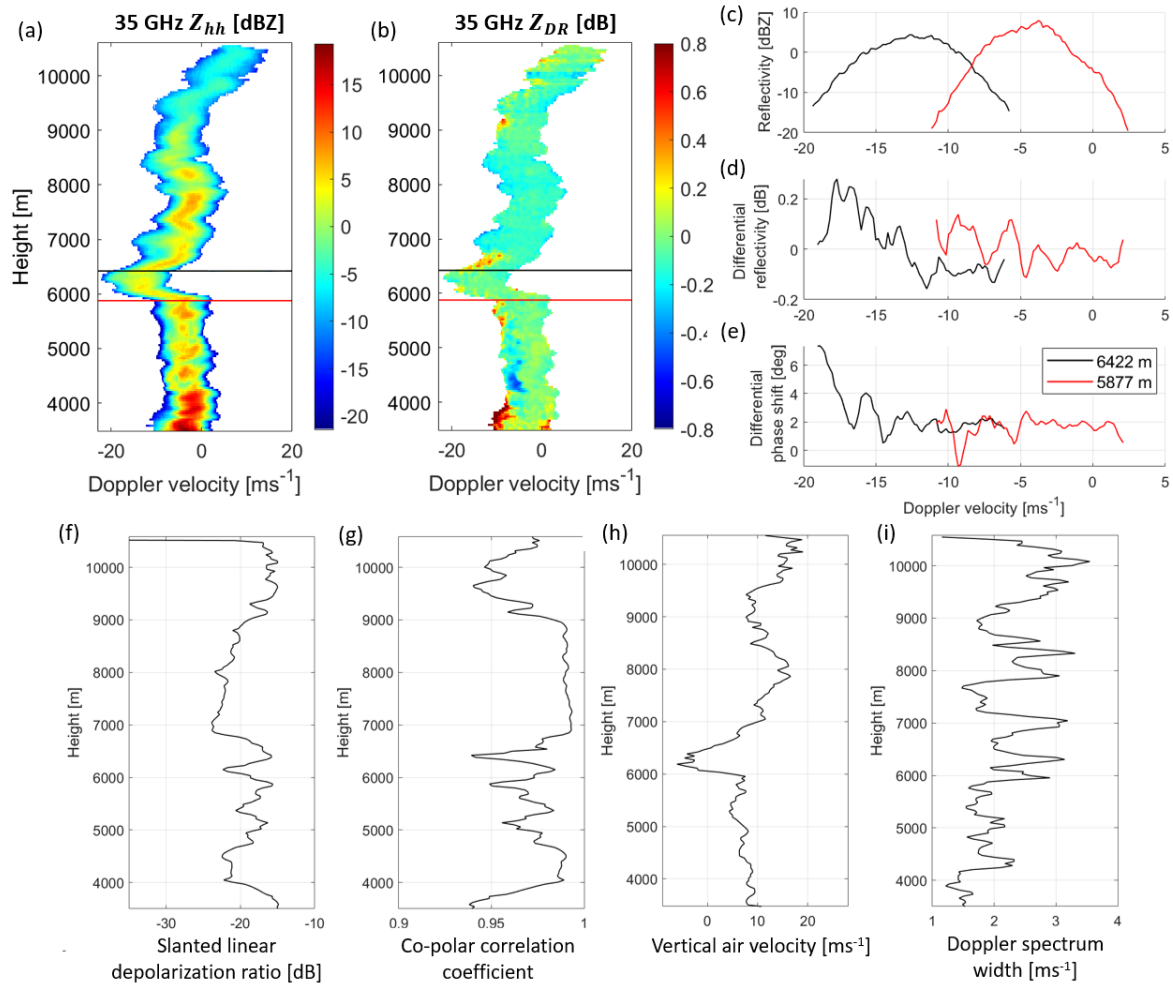


Figure 8.20: 2021-06-18 17:23:47 UTC where the three peaks of SL_{DR} and ρ_{hv} are observed (a-b) Spectrograms of reflectivity and differential reflectivity (c-e) spectra of reflectivity, Z_{DR} and Ψ_{DP} at 5877 m (middle peak) and 6422 m (highest peak) (f-i) profiles of SL_{DR} , ρ_{hv} , vertical air velocity and Doppler spectrum width

8.2.4. Possibility of chains

From Figure 8.12(a), high Z_{DR} is observed at the top of the cloud from 17:22 UTC onward. The Doppler spectra at 10003 m at 2021-06-18 17:22:57 UTC is shown in Figure 8.21(d-f). The differential reflectivity of the Rayleigh plateau (Doppler velocity $> 5 \text{ m s}^{-1}$) is around 0.2 dB, and the entire spectrum of Z_{DR} is positive. One hypothesis is that the large particles with positive Z_{DR} are chain-like aggregates that formed under cloud electric field. From the literature, chains can be observed when the temperature is lower than -40°C [17]. In the case being studied, temperature is lower than -40°C above 9600 m, which backs up the hypothesis that chains might be present. Mie scattering occurs at around 5 m s^{-1} as Z_{DR} increases and Ψ_{DP} begins to fluctuate. Scattering simulation is carried out to estimate the size of the particles based on the trend of Mie scattering. In the simulation, chains are modelled as prolate particles. From the literature, chain-like aggregates can be up to several tens of particles long [18] and individual crystals in the chains are aligned with their maximum dimension along the length of the chain [17]. The individual particles can be plates, with typical axis ratio of less than 0.3 [41], or quasi-spherical frozen droplets with diameters of 15-20 μm [18]. Based on these, the axis ratio of chains (ratio of long axis to short axis) should be much larger than 1. However, the simulation code used cannot converge when particle size increases when the axis ratio is too large, thus the maximum possible axis ratio that can be used to allow Mie scattering regime to be reached is 7. Since chains are a type of aggregates, ice fraction of typical aggregates is used, which is 0.3. The chains are assumed to be oriented with their long axis parallel to the horizontal, thus the Euler angle $\beta = 90^\circ$. The orientation follows a Gaussian distribution with a standard deviation of 0.1° .

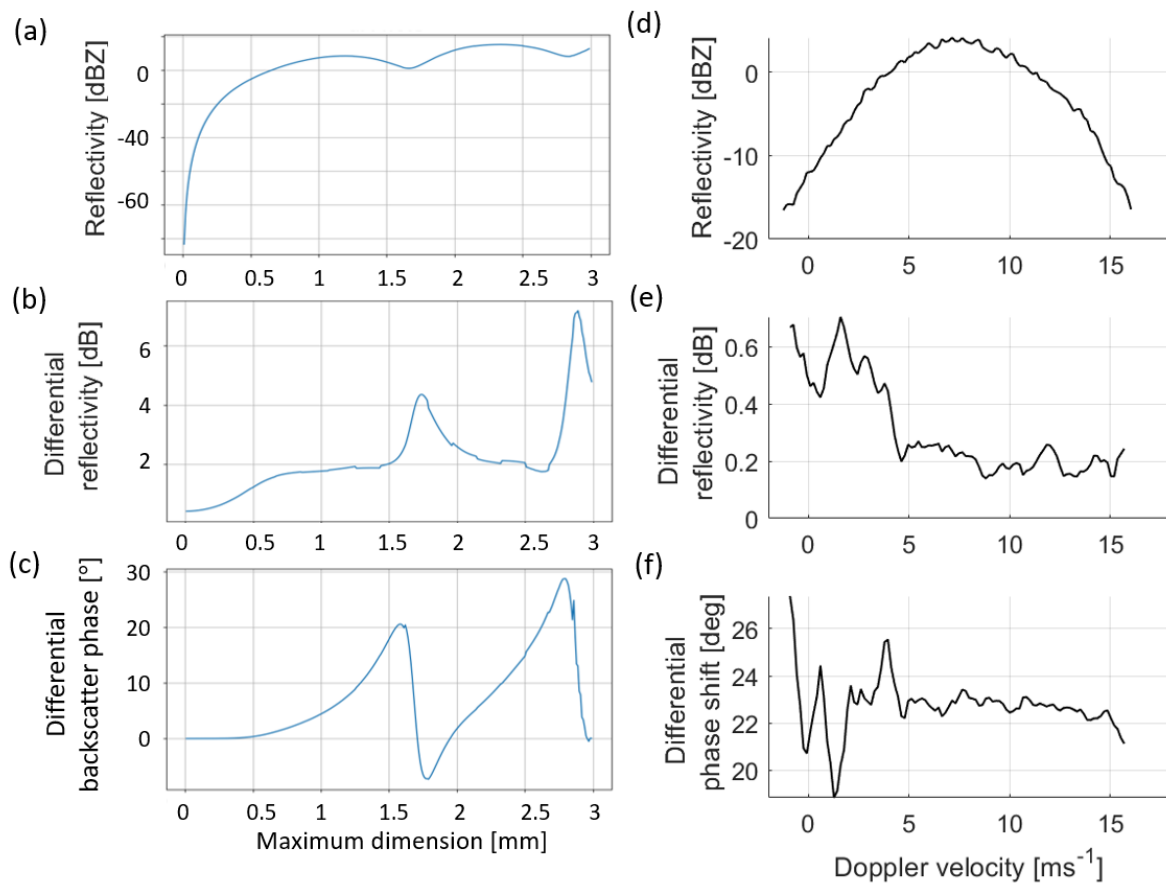


Figure 8.21: (a-c) Simulated reflectivity, differential reflectivity and differential backscatter phase of chains with axis ratio 7 and ice fraction 0.3 oriented with long axis parallel to the horizontal. (d-f) Spectral reflectivity, differential reflectivity and differential phase shift at 10003 m at 17:22:57 UTC

The simulated scattering behaviour of chains are shown in Figure 8.21(a-c). The maximum dimension refers to the length of the long axis of the spheroid. Similar to the observed spectral differential phase shift in Figure 8.21(f), the simulated differential backscatter phase Figure 8.21(c) shows a peak followed by a trough, while spectral differential reflectivity shows a peak. This occurs when scatterers have a maximum dimension of around 1.5 mm, which suggests that the observed particles have sizes reaching around 1.5 mm. However, from the literature, chains collected in thunderstorm clouds have lengths of at most 0.8 mm [17]. There are several reasons for the discrepancy between results based on simulation and the literature. For instance, the axis ratio used in the simulation may not be large enough for chains, and a spheroid model may not be sufficient to describe the shape of chains. According to Figure 2.4, chains can be irregular in shape, and the effect of the irregularities could increase as their sizes become more comparable to the radar wavelength.

Other than using scattering simulations, the presence of chain-like aggregates could also be supported by checking whether the region concerned fulfils the conditions described in the literature for the enhancement of aggregation by electric fields to occur, which are an electric field of 50-150 kV/m and ice particle number concentration of at least 2 cm^{-3} . Unfortunately, these data are not available in this study.

9

Conclusion

In this study, two major thunderstorm clouds on 2021-06-18 from 16:10 to 17:45 UTC near Cabauw were studied in depth to explore how cloud radar data can be used to help understand processes in thunderstorm clouds. Section 9.1 first summarises the polarimetric calibration method developed in this study. The following sections summarise the findings with reference to the research questions introduced in Section 1.1. At the end, some recommendations for further investigation are given.

9.1. Polarimetric calibration

Calibration of differential reflectivity was carried out by assuming multiplicative bias in linear differential reflectivity. The total expected error of the calibration curve is 0.051 dB at both 35 and 94 GHz, which is smaller than the error of the instrument (0.1 dB). Calibration of differential phase shift was carried out by assuming additive bias. The total expected error of the calibration curve is 0.57° at 35 GHz and 0.49° at 94 GHz. The method of calibration detailed in Section 5.2 could become the standard procedure to pre-process polarimetric data in future studies.

9.2. Hydrometeors in thunderstorm clouds

Several types of hydrometeors are observed in clouds that produced lightning. In the first cloud, super-cooled water is found at the edge of the cloud at around 6000 m, which is supported by the increased liquid water path and near zero differential reflectivity of a separate mode of particles on the right of the Doppler spectra.

In the fourth cloud, comparison between scattering simulation and observations supports the presence of conical graupel with maximum dimension of 3-5.2 mm. The falling graupel coexist with ice particles that are brought upwards by updrafts, which could lead to non-inductive charging. The temperature at the corresponding heights could give rise to a tripolar structure of the thunderstorm cloud.

In the first and fourth clouds, there is a possibility that chain-like aggregates of small ice particles are present in the top of the cloud, which is reflected by large magnitudes of Z_{DR} on the left side of the Doppler spectrum. Nonetheless, no realistic scattering simulation could be carried out to confirm the size and characteristics of the chains.

9.3. Alignment of ice crystals in thunderstorm clouds

Vertical alignment of ice particles can be observed right before lightning, which is reflected by negative Z_{DR} values as low as -0.4 dB. When the lightning is close to the line of sight of the radar, particles of all sizes are vertically aligned. Near a lightning stroke, most particles are aligned in the same way, resulting in low canting variance as reflected by low SL_{DR} . When the lightning is far away, only small particles on the right side of the Doppler spectra are vertically aligned. However, there are also some situations where negative Z_{DR} is observed that suggests vertical alignment of particles by the electric field, yet there are no lightning strokes measured nearby in space and time. This could be because

the electric field is not strong enough to trigger lightning, or that some lightning strokes are not being recorded.

9.4. Updraft and downdraft pattern in thunderstorm clouds

Updrafts and downdrafts can be observed at different parts of the thunderstorm cloud. Near the edge of the first cloud, downdrafts can be observed. At the top and near the core of the fourth cloud, strong updrafts of up to 30 m s^{-1} can be observed. In general, vertical air velocity is not uniform in thunderstorm clouds, which suggests that there is strong turbulence. This is also supported by large Doppler spectrum width of up to $3\text{--}4 \text{ m s}^{-1}$. When strong turbulence is present, slanted linear depolarisation ratio increases and co-polar correlation coefficient decreases, which suggest that canting variance of particles within a radar resolution volume increases.

9.5. Time and distance of detectable signatures

Negative Z_{DR} can be observed up to 4 seconds before lightning and disappears within 3 seconds after the lightning. Such signatures are detectable if the lightning is close to the line of sight of the radar or is far (up to 5.5 km) but strong. Sudden decrease in SL_{DR} can be observed if the lightning is close but not when it is far.

9.6. Appropriate measurement modes for studying thunderstorms

In the case being studied, only measurements with constant elevation and azimuth and zenith observation were available, but their drawback is that only a small part of the thunderstorm cloud along the radar's line of sight could be measured, which leads to a low number of thunderstorm events recorded by the radar. In addition, it is not possible to look at the whole thunderstorm cloud at the same time to analyse the spatial variations within the cloud. Also, each part of the thunderstorm cloud only passes over the line of sight of the radar once, thus it is impossible to analyse the evolution of different parts of the cloud. A more appropriate radar measurement mode for studying thunderstorms would be azimuth scan with constant elevation (PPI). With PPI mode, thunderstorm clouds in all directions can be measured by the radar, so there can be more cases to choose from for in-depth study or statistical analysis. Moreover, it may become possible to analyse differences between different parts of the thunderstorm cloud with different levels of lightning activities, as well as how the cloud evolves with time.

Regarding the wavelength of the radar, 35 GHz is preferred over 94 GHz. The first reason is that there is less attenuation at 35 GHz, so the radar can penetrate more into the cloud when there is precipitation. Another reason is that Mie scattering occurs for larger particle sizes at 35 GHz. Since Mie scattering can result in fluctuations in differential reflectivity and differential phase shift that can be difficult to interpret, Doppler spectra at 35 GHz with less Mie scattering are easier to analyse than at 94 GHz. In addition, the Nyquist velocity at 35 GHz is three times larger than at 94 GHz. This can prevent aliasing, which could cause overlapping of true and aliased spectra especially when spectra width is large in thunderstorms.

The final suggestion would be to increase the range of the radar. In the case studied, the thunderstorm cloud is taller than the maximum range of the radar, which resulted in the top of the cloud being folded into the second chirp. Since thunderstorm clouds can extend above 10 km, it is advisable to increase the range of the radar so that it can reach a height of for instance 15 km, but this would reduce the range resolution at the same time.

9.7. Recommendations

There are a number of aspects that can be further explored in this research, but was not possible due to their challenging nature or data limitations. Recommendations for further investigation are summarised below.

Improve quality of existing data

- Level 1 SL_{DR} and ρ_{hv} data could be verified using Level 0 data to strengthen confidence in interpretations.
- Spectral SL_{DR} when vertical alignment of particles is observed can be analysed.
- Φ_{DP} can be extracted by removing δ_{co} from Ψ_{DP} using techniques such as automatic Rayleigh plateau detection to obtain true K_{DP} .
- Relationship between differential attenuation and rainfall rate for thunderstorms at millimeter wavelengths can be investigated. If differential attenuation during precipitation can be corrected, it may become possible to analyse polarimetric signals when lightning is the most active, such as the case in Appendix C.

Other simulations

- More advanced scattering simulation codes could be used to verify the hydrometeors present in thunderstorm clouds. For example, the open-source code ADDA which utilises discrete dipole approximation could simulate scatterers of arbitrary shape and composition [42]. More realistic simulations of conical graupel and chain aggregates could be performed to estimate their size and shape.
- More sophisticated models that are capable of simulating backscatter radar signals from a mixture of hydrometeors can be used. For example, the Passive and Active Microwave TRAnsfer model (PAMTRA) [43] can take hydrometeor properties and size distributions as input, and give radar reflectivity, Z_{DR} , L_{DR} and Doppler spectrum as outputs. By prescribing the types and size distributions of ice particles, simulation results could support the interpretation of the observations. In addition, PAMTRA can make use of the atmospheric state variable and then account for attenuation. The second and fourth cloud where there are significant attenuation could be simulated to understand the cause of the negative Z_{DR} values. PAMTRA can take into account radar limitations like noise and poser sensitivity as well.
- The whole thunderstorm event can be simulated using a numerical cloud model that include microphysical schemes for the growth of hydrometeors, such as the Bryan cloud model (CM1) [44], together with lightning parameterization that models the electrical evolution of the cloud, such as the numerical thunderstorm model by Mansell et al. [45]. The model output could be used as the input of PAMTRA to simulate radar variables. The results could be used to support the interpretation of the observations.
- Ice microphysics models such as McSnow [46] that allow tracking of the particle history coupled with an electrification model may help investigate the response of ice particles to the presence of an electric field.

Additional data on thunderstorms

- More comprehensive lightning data, for instance the height of lightning initiation, could be obtained to strengthen links between observed polarimetric signatures and lightning events. One possibility is to set up a lightning mapping array (LMA) around the radar similar to the Thunderstorm Electrification and Lightning Experiment (TELEX) field program in Oklahoma [47], which would be able to map lightning activities in 3D space as a function of time.
- Electric field strength and charge distribution in thunderstorm clouds could be measured or estimated to understand the magnitude of the electric field needed to produce observable polarimetric signatures, relate the electric field strength with sizes of aligned ice crystals, and support the presence of chain-like aggregates due to electric field enhanced aggregations. One possibility is to use lightning activities mapped by LMA to estimate the charged regions in thunderstorm clouds [47]. Another possibility is to launch balloons carrying an electric-field meter into thunderstorm clouds to obtain in-situ measurements of cloud electric field strength.

Finally, other thunderstorm cases could be studied to see whether consistent signatures can be observed. When more cases are studied, statistical analysis may be carried out to identify features that can help predict lightning.

Bibliography

- [1] S. E. Reynolds, M. Brook, and M. F. Gourley, "Thunderstorm charge separation," *Journal of Atmospheric Sciences*, vol. 14, no. 5, pp. 426–436, 1957.
- [2] E. Workman and S. Reynolds, "Electrical activity as related to thunderstorm cell growth," *Bulletin of the American Meteorological Society*, vol. 30, no. 4, pp. 142–144, 1949.
- [3] R. Lhermitte, "A 94-gHz doppler radar for cloud observations," *Journal of Atmospheric and Oceanic Technology*, vol. 4, no. 1, pp. 36–48, 1987.
- [4] Z. Sokol, J. Minářová, and O. Fišer, "Hydrometeor distribution and linear depolarization ratio in thunderstorms," *Remote Sensing*, vol. 12, no. 13, p. 2144, 2020.
- [5] P. K. Wang, *Physics and dynamics of clouds and precipitation*. Cambridge University Press, 2013.
- [6] R. Gunn, "Electric-field regeneration in thunderstorms," *Journal of Atmospheric Sciences*, vol. 11, no. 2, pp. 130–138, 1954.
- [7] T. C. Marshall and W. P. Winn, "Measurements of charged precipitation in a new Mexico thunderstorm: Lower positive charge centers," *Journal of Geophysical Research: Oceans*, vol. 87, no. C9, pp. 7141–7157, 1982.
- [8] F. J. Merceret, J. G. Ward, D. M. Mach, M. G. Bateman, and J. E. Dye, "On the magnitude of the electric field near thunderstorm-associated clouds," *Journal of Applied Meteorology and Climatology*, vol. 47, no. 1, pp. 240–248, 2008.
- [9] T. Takahashi, "Riming electrification as a charge generation mechanism in thunderstorms," *Journal of Atmospheric Sciences*, vol. 35, no. 8, pp. 1536–1548, 1978.
- [10] M. P. Bailey and J. Hallett, "A comprehensive habit diagram for atmospheric ice crystals: Confirmation from the laboratory, air, and other field studies," *Journal of the Atmospheric Sciences*, vol. 66, no. 9, pp. 2888–2899, 2009.
- [11] H. R. Pruppacher and J. D. Klett, *Microphysics of clouds and precipitation*. Springer, 1980.
- [12] D. Lamb and J. Verlinde, *Physics and chemistry of clouds*. Cambridge University Press, 2011.
- [13] G. Tang, P. Yang, P. G. Stegmann, R. L. Panetta, L. Tsang, and B. Johnson, "Effect of particle shape, density, and inhomogeneity on the microwave optical properties of graupel and hailstones," *IEEE Transactions on Geoscience and Remote Sensing*, vol. 55, no. 11, pp. 6366–6378, 2017.
- [14] M. Oue, M. R. Kumjian, Y. Lu, Z. Jiang, E. E. Clothiaux, J. Verlinde, and K. Aydin, "X-band polarimetric and ka-band doppler spectral radar observations of a graupel-producing arctic mixed-phase cloud," *Journal of Applied Meteorology and Climatology*, vol. 54, no. 6, pp. 1335–1351, 2015.
- [15] Y. Lu, Z. Jiang, K. Aydin, J. Verlinde, E. E. Clothiaux, and G. Botta, "A polarimetric scattering database for non-spherical ice particles at microwave wavelengths," *Atmospheric Measurement Techniques*, vol. 9, no. 10, pp. 5119–5134, 2016.
- [16] S. G. Cober and R. List, "Measurements of the heat and mass transfer parameters characterizing conical graupel growth," *Journal of Atmospheric Sciences*, vol. 50, no. 11, pp. 1591–1609, 1993.
- [17] P. Connolly, C. Saunders, M. Gallagher, K. Bower, M. Flynn, T. Choularton, J. Whiteway, and R. Lawson, "Aircraft observations of the influence of electric fields on the aggregation of ice crystals," *Quarterly Journal of the Royal Meteorological Society: A journal of the atmospheric sciences, applied meteorology and physical oceanography*, vol. 131, no. 608, pp. 1695–1712, 2005.

- [18] J.-F. Gayet, G. Mioche, L. Bugliaro, A. Protat, A. Minikin, M. Wirth, A. Dörnbrack, V. Shcherbakov, B. Mayer, A. Garnier, *et al.*, "On the observation of unusual high concentration of small chain-like aggregate ice crystals and large ice water contents near the top of a deep convective cloud during the circle-2 experiment," *Atmospheric Chemistry and Physics*, vol. 12, no. 2, pp. 727–744, 2012.
- [19] N. M. A. Wahab, *Ice crystal interactions in electric fields*. PhD thesis, UMIST, 1974.
- [20] E. V. Mattos, L. A. T. Machado, E. R. Williams, and R. I. Albrecht, "Polarimetric radar characteristics of storms with and without lightning activity," *Journal of Geophysical Research: Atmospheres*, vol. 121, no. 23, pp. 14–201, 2016.
- [21] B. Vonnegut, "Orientation of ice crystals in the electric field of a thunderstorm," *Weather*, vol. 20, no. 10, pp. 310–312, 1965.
- [22] A. J. Weinheimer and A. A. Few, "The electric field alignment of ice particles in thunderstorms," *Journal of Geophysical Research: Atmospheres*, vol. 92, no. D12, pp. 14833–14844, 1987.
- [23] N. R. Lund, D. R. MacGorman, T. J. Schuur, M. I. Biggerstaff, and W. D. Rust, "Relationships between lightning location and polarimetric radar signatures in a small mesoscale convective system," *Monthly Weather Review*, vol. 137, no. 12, pp. 4151–4170, 2009.
- [24] V. Melnikov, D. S. Zrnić, M. E. Weber, A. O. Fierro, and D. R. MacGorman, "Electrified cloud areas observed in the shv and ldr radar modes," *Journal of Atmospheric and Oceanic Technology*, vol. 36, no. 1, pp. 151–159, 2019.
- [25] H. Cho, J. Iribarne, and W. Richards, "On the orientation of ice crystals in a cumulonimbus cloud," *Journal of the Atmospheric Sciences*, vol. 38, no. 5, pp. 1111–1114, 1981.
- [26] G. Brussaard, "A meteorological model for rain-induced cross polarization," *IEEE Transactions on Antennas and Propagation*, vol. 24, no. 1, pp. 5–11, 1976.
- [27] M. B. Baker, H. J. Christian, and J. Latham, "A computational study of the relationships linking lightning frequency and other thundercloud parameters," *Quarterly Journal of the Royal Meteorological Society*, vol. 121, no. 527, pp. 1525–1548, 1995.
- [28] E. J. Zipser and K. R. Lutz, "The vertical profile of radar reflectivity of convective cells: A strong indicator of storm intensity and lightning probability?," *Monthly Weather Review*, vol. 122, no. 8, pp. 1751–1759, 1994.
- [29] J. L. Stiith, B. Basarab, S. A. Rutledge, and A. Weinheimer, "Anvil microphysical signatures associated with lightning-produced no x," *Atmospheric Chemistry and Physics*, vol. 16, no. 4, pp. 2243–2254, 2016.
- [30] T. C. Marshall, W. D. Rust, and M. Stolzenburg, "Electrical structure and updraft speeds in thunderstorms over the southern great plains," *Journal of Geophysical Research: Atmospheres*, vol. 100, no. D1, pp. 1001–1015, 1995.
- [31] W. Deierling, W. A. Petersen, J. Latham, S. Ellis, and H. J. Christian, "The relationship between lightning activity and ice fluxes in thunderstorms," *Journal of Geophysical Research: Atmospheres*, vol. 113, no. D15, 2008.
- [32] W. Deierling and W. A. Petersen, "Total lightning activity as an indicator of updraft characteristics," *Journal of Geophysical Research: Atmospheres*, vol. 113, no. D16, 2008.
- [33] E. O'Connor, "Model data from cabauw on 18 june 2021," 04 2022.
- [34] K. GmbH, "Lightning and radar utrecht." <https://meteologix.com/nl/stormradar/utrecht/20210618-1615z.html>. Accessed: 2023-05-12.
- [35] V. N. Bringi and V. Chandrasekar, *Polarimetric Doppler weather radar: principles and applications*. Cambridge university press, 2001.

- [36] P. Wang, "Dealiasing of doppler spectra for cloud radar at 94 ghz," Master's thesis, Delft University of Technology, 2023.
- [37] Y. Lu, Z. Jiang, K. Aydin, J. Verlinde, E. E. Clothiaux, and G. Botta, "A polarimetric scattering database for non-spherical ice particles at microwave wavelengths," *Atmospheric Measurement Techniques*, vol. 9, no. 10, pp. 5119–5134, 2016.
- [38] J. Leinonen, "High-level interface to t-matrix scattering calculations: architecture, capabilities and limitations," *Optics express*, vol. 22, no. 2, pp. 1655–1660, 2014.
- [39] S. G. Warren, "Optical constants of ice from the ultraviolet to the microwave," *Applied optics*, vol. 23, no. 8, pp. 1206–1225, 1984.
- [40] Y. Wang, T.-Y. Yu, A. V. Ryzhkov, and M. R. Kumjian, "Application of spectral polarimetry to a hailstorm at low elevation angle," *Journal of Atmospheric and Oceanic Technology*, vol. 36, no. 4, pp. 567–583, 2019.
- [41] A. Spek, C. Unal, D. Moisseev, H. Russchenberg, V. Chandrasekar, and Y. Dufournet, "A new technique to categorize and retrieve the microphysical properties of ice particles above the melting layer using radar dual-polarization spectral analysis," *Journal of atmospheric and oceanic technology*, vol. 25, no. 3, pp. 482–497, 2008.
- [42] M. A. Yurkin and A. G. Hoekstra, "The discrete-dipole-approximation code adda: capabilities and known limitations," *Journal of Quantitative Spectroscopy and Radiative Transfer*, vol. 112, no. 13, pp. 2234–2247, 2011.
- [43] M. Mech, M. Maahn, S. Kneifel, D. Ori, E. Orlandi, P. Kollias, V. Schemann, and S. Crewell, "Pamtra 1.0: the passive and active microwave radiative transfer tool for simulating radiometer and radar measurements of the cloudy atmosphere," *Geoscientific Model Development*, vol. 13, no. 9, pp. 4229–4251, 2020.
- [44] G. H. Bryan and J. M. Fritsch, "A benchmark simulation for moist nonhydrostatic numerical models," *Monthly Weather Review*, vol. 130, no. 12, pp. 2917–2928, 2002.
- [45] E. R. Mansell, D. R. MacGorman, C. L. Ziegler, and J. M. Straka, "Simulated three-dimensional branched lightning in a numerical thunderstorm model," *Journal of Geophysical Research: Atmospheres*, vol. 107, no. D9, pp. ACL–2, 2002.
- [46] S. Brdar and A. Seifert, "Mcsnow: A monte-carlo particle model for riming and aggregation of ice particles in a multidimensional microphysical phase space," *Journal of advances in modeling earth systems*, vol. 10, no. 1, pp. 187–206, 2018.
- [47] D. R. MacGorman, W. D. Rust, T. J. Schuur, M. I. Biggerstaff, J. M. Straka, C. L. Ziegler, E. R. Mansell, E. C. Bruning, K. M. Kuhlman, N. R. Lund, *et al.*, "Telex the thunderstorm electrification and lightning experiment," *Bulletin of the American Meteorological Society*, vol. 89, no. 7, pp. 997–1014, 2008.

Appendix

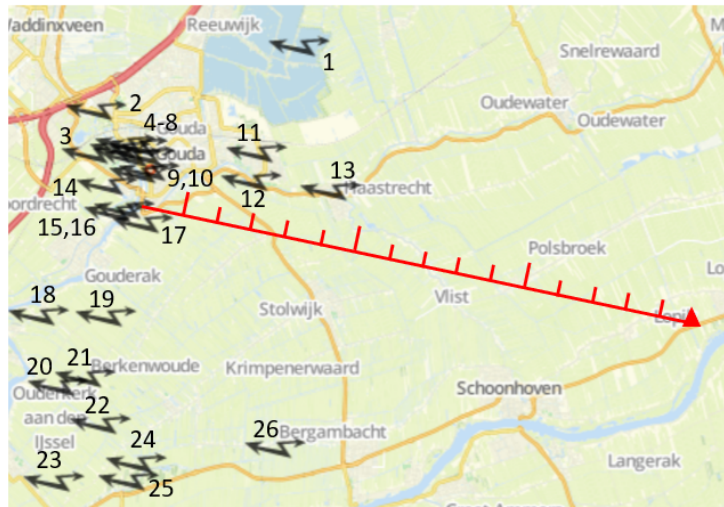
A. Thunderstorm event list

Date	Start	End	Location	Mode	Azimuth	Elevation	Frequency	Remarks
2021-05-09	09:25	10:00	Cabauw	ZEN	0	90	35,94	
				ZEN	0	90	94	by Delft radar
2021-05-19	11:40	12:00	Cabauw	ZEN	0	90	35,94	
				ZEN	0	90	94	by Delft radar
2021-06-18	16:45	17:40	Cabauw	CEL	102	135	35,94	
				ZEN	0	90	94	by Delft radar
2021-06-19	21:50	22:25	Cabauw	CEL	102	135	35,94	
				ZEN	0	90	94	by Delft radar; no data from 21:35
2021-07-25	15:55	15:45	Cabauw	CEL	102	135	35,94	
				ZEN	0	90	94	by Delft radar; too much attenuation, can't see cloud
2022-05-19	11:00	12:15	Cabauw	PPI	0-360	75	35,94	
2022-06-24	00:30	01:25	Cabauw				35,94	no data
2022-09-06	20:45	22:20	Cabauw				35,94	no data
2022-09-28	12:45	12:55	Cabauw				35,94	no data
2021-05-09	07:35	07:55	Delft				94	located at Cabauw
2021-05-09	10:55	11:10	Delft				94	located at Cabauw
2021-05-09	11:50	11:55	Delft				94	located at Cabauw
2021-05-09	19:10	19:40	Delft				94	located at Cabauw
2021-05-24	15:55	16:30	Delft				94	located at Cabauw; no data
2021-05-25	22:40	23:10	Delft				94	located at Cabauw
2021-06-18	14:00	16:45	Delft				94	located at Cabauw
2021-06-19	22:20	22:40	Delft				94	located at Cabauw
2021-07-26	12:10	13:30	Delft				94	located at Cabauw
2021-08-07	14:55	15:20	Delft				94	located at Cabauw
2021-11-28	19:20	20:00	Delft				94	no data
2022-06-27	12:15	12:50	Delft		0	90	94	
2022-08-15	16:30	17:45	Delft				94	located at Rotterdam
2022-09-06	21:00	21:50	Delft				94	located at Rotterdam
2021-06-18	18:40	19:55	Lutjewad	ZEN	0	90	94	
2021-08-07	18:25	18:55	Lutjewad	ZEN	0	90	94	
2022-05-19	12:45	13:15	Lutjewad	ZEN	0	90	94	
2022-06-19	03:35	03:40	Lutjewad	ZEN	0	90	94	
2022-06-30	21:30	21:35	Lutjewad	ZEN	0	90	94	
2021-05-09	10:35	11:10	Rotterdam				94	located at Cabauw
2021-05-23	02:45	02:55	Rotterdam				94	located at Cabauw
2021-06-18	14:15	16:25	Rotterdam				94	located at Cabauw
2021-07-24	13:10	14:35	Rotterdam				94	located at Cabauw
2021-07-25	14:00	14:35	Rotterdam				94	located at Cabauw
2021-07-26	12:05	13:20	Rotterdam				94	located at Cabauw
2021-10-20	15:30	15:55	Rotterdam				94	located at Cabauw
2022-09-06	21:00	21:55	Rotterdam	ZEN,CEL,CEL,PPI	0,2,3,65,0-360	90,45,30,85	94	

Figure 1: List of thunderstorm events from 2021 to 2022

B. Lightning maps

2021-06-18 16:20 UTC

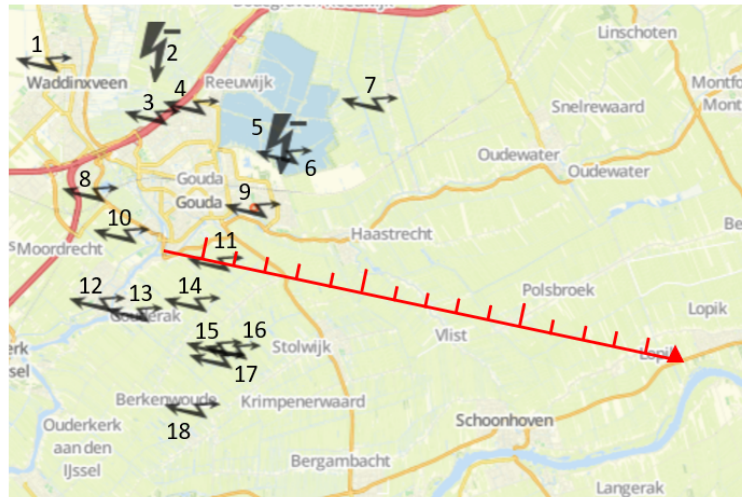


	UTC	kA		UTC	kA
1	16:18:33	-4	14	16:17:10	-6
2	16:19:01	-5	15	16:19:53	-3
3	16:18:12	-3	16	16:17:10	-7
4	16:18:33	-4	17	16:17:11	-6
5	16:18:12	-4	18	16:18:44	-5
6	16:18:12	-3	19	16:16:42	-5
7	16:18:12	-4	20	16:15:12	-4
8	16:18:12	-3	21	16:16:01	-15
9	16:17:41	-5	22	16:15:12	-3
10	16:19:00	-4	23	16:18:05	-3
11	16:19:29	-3	24	16:17:29	-4
12	16:17:10	-3	25	16:17:29	-4
13	16:17:30	-4	26	16:17:30	-5

1 to 3 kA Sissy mutterer
 3 to 7 kA Medium roller
 > 7 kA Strong slammer

Figure 2: Location, time and power of lightning strokes from 2021-06-18 16:15 to 16:20 UTC. Red triangle shows radar location, red ruler shows line of sight of radar with each mark equal to 1 km

2021-06-18 16:25 UTC



	UTC	kA		UTC	kA
1	16:23:50	2	10	16:23:07	-3
2	16:21:14	-13	11	16:20:17	2
3	16:20:17	5	12	16:21:51	2
4	16:20:40	-8	13	16:20:17	4
5	16:21:09	-3	14	16:20:17	-3
6	16:20:40	-4	15	16:22:20	8
7	16:21:50	-3	16	16:21:50	4
8	16:21:00	4	17	16:22:20	-5
9	16:21:50	-3	18	16:20:37	-5

Figure 3: Location, time and power of lightning strokes from 2021-06-18 16:20 to 16:25 UTC. Legend same as Figure 2. Cloud-to-ground lightning in bold

2021-06-18 16:30 UTC

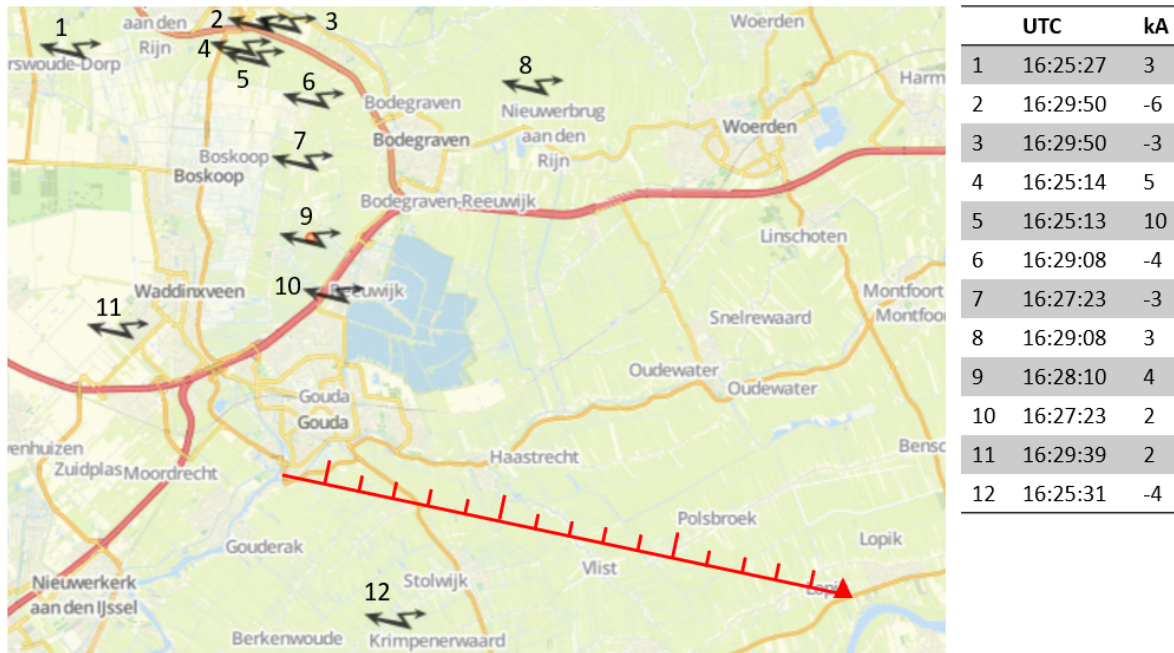


Figure 4: Location, time and power of lightning strokes from 2021-06-18 16:25 to 16:30 UTC. Legend same as Figure 2

2021-06-18 17:20 UTC

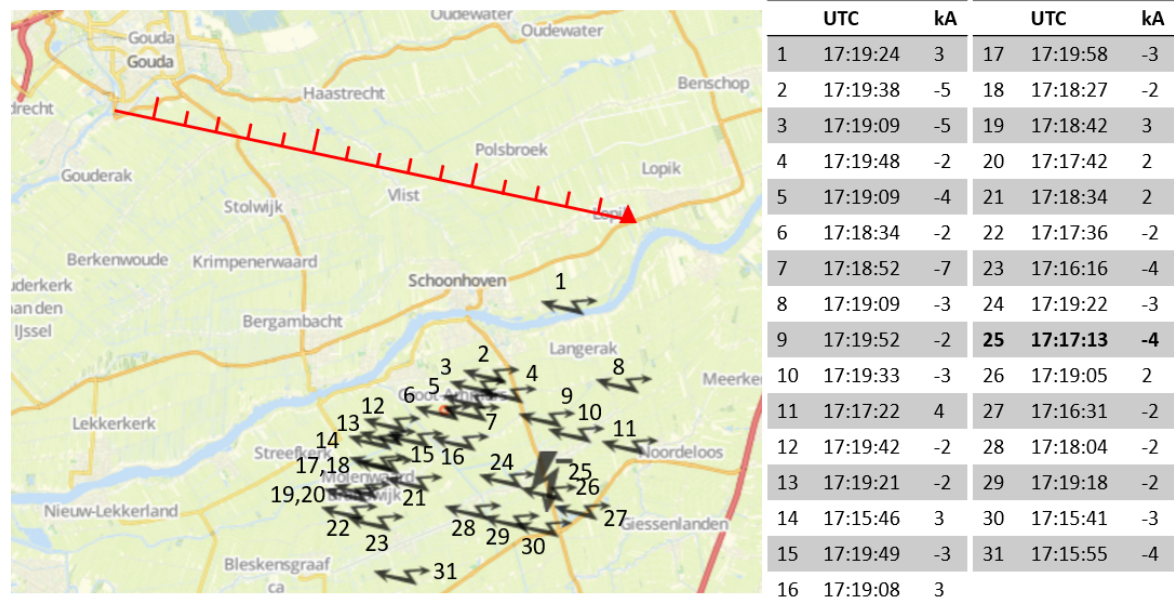
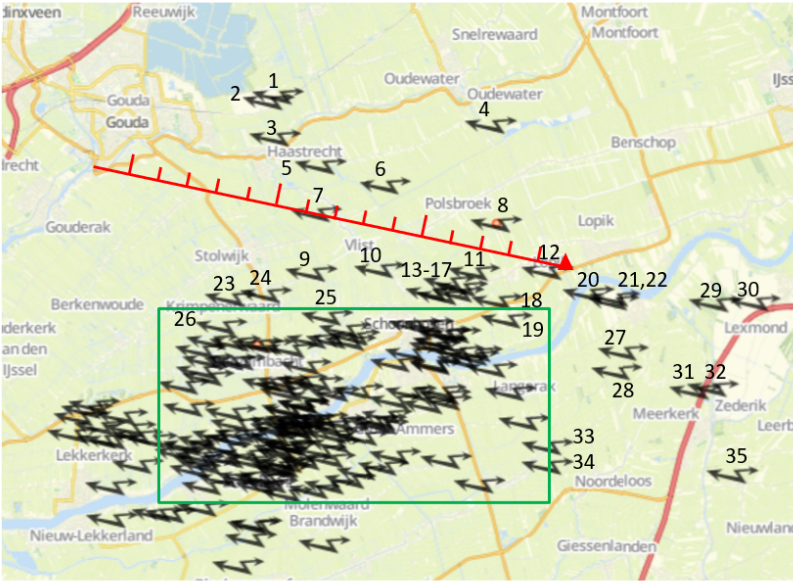


Figure 5: Location, time and power of lightning strokes from 2021-06-18 17:15 to 17:20 UTC. Legend same as Figure 2. Cloud-to-ground lightning in bold

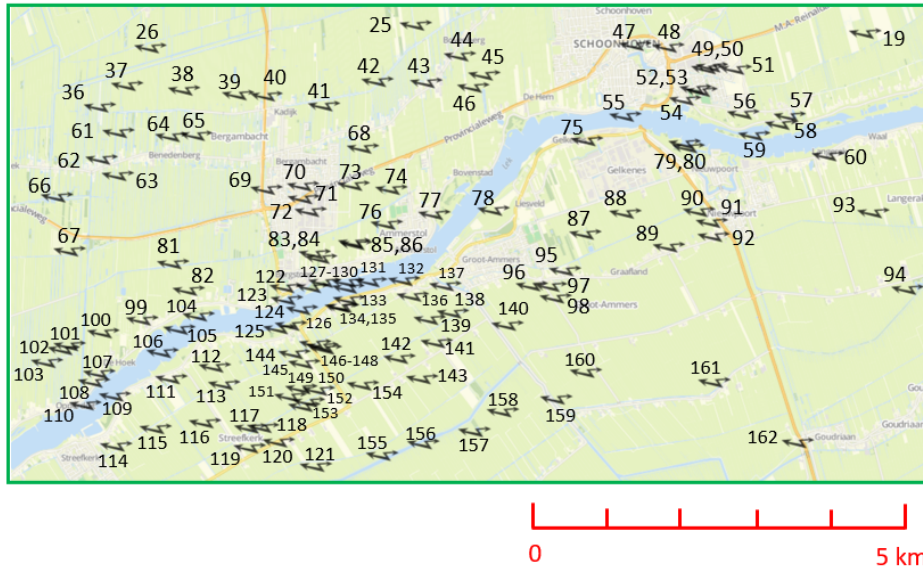
2021-06-18 17:25 UTC



	UTC	kA	UTC	kA	
1	17:21:05	-3	19	17:23:37	2
2	17:21:32	5	20	17:24:37	-3
3	17:23:36	-2	21	17:23:47	-4
4	17:24:51	4	22	17:23:47	-4
5	17:24:16	-5	23	17:24:28	-4
6	17:21:33	6	24	17:23:50	-7
7	17:21:32	5	25	17:23:23	-3
8	17:21:58	-5	26	17:24:18	-5
9	17:24:51	5	27	17:23:07	-2
10	17:20:01	-5	28	17:22:20	-2
11	17:24:27	-8	29	17:23:33	-4
12	17:22:58	-2	30	17:23:23	-2
13	17:23:50	4	31	17:24:35	-4
14	17:24:37	-3	32	17:24:35	-4
15	17:24:37	-6	33	17:22:18	-2
16	17:24:47	-3	34	17:21:31	-1
17	17:22:58	-5	35	17:20:47	-3
18	17:24:56	-2			

Figure 6: Location, time and power of lightning strokes from 2021-06-18 17:20 to 17:25 UTC. See Figure 7 for lightning in green rectangle. Legend same as Figure 2

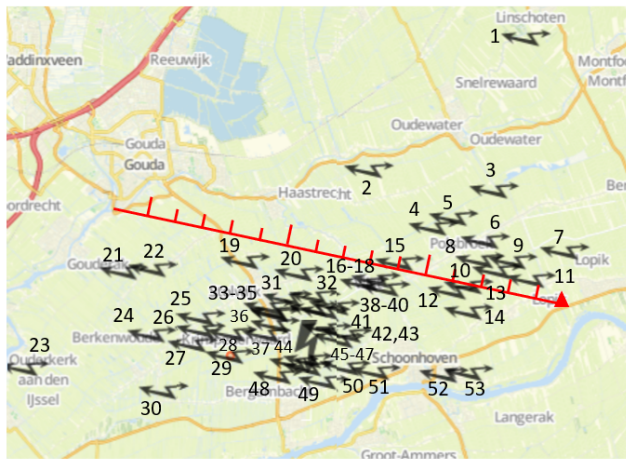
2021-06-18 17:25 UTC



UTC	kA	UTC	kA	UTC	kA	UTC	kA	UTC	kA	UTC	kA	UTC	kA	
36	17:21:28	-3	55	17:21:58	3	74	17:24:35	-4	93	17:20:27	-3	112	17:21:29	-2
37	17:21:28	-6	56	17:21:37	-6	75	17:21:15	-3	94	17:20:10	-3	113	17:20:30	-3
38	17:24:41	-3	57	17:23:15	2	76	17:23:43	-2	95	17:23:55	-3	114	17:21:35	-2
39	17:21:37	-3	58	17:21:37	-4	77	17:21:03	-5	96	17:20:27	-3	115	17:21:17	-6
40	17:24:41	-2	59	17:21:48	-2	78	17:20:27	-3	97	17:21:49	-3	116	17:21:42	-3
41	17:24:23	-4	60	17:23:07	-3	79	17:21:05	-3	98	17:23:55	-2	117	17:21:52	-4
42	17:24:03	4	61	17:23:15	-3	80	17:20:01	-3	99	17:20:18	-6	118	17:22:04	-6
43	17:20:18	-5	62	17:21:01	-6	81	17:22:30	-7	100	17:24:35	-3	119	17:21:45	-6
44	17:24:18	-2	63	17:22:30	-3	82	17:21:15	-2	101	17:21:01	-2	120	17:22:04	-4
45	17:22:58	4	64	17:23:30	-4	83	17:22:20	-4	102	17:21:08	-3	121	17:22:04	-3
46	17:23:16	-5	65	17:23:18	-5	84	17:22:20	7	103	17:22:07	-2	122	17:21:02	-3
47	17:24:16	-4	66	17:23:30	-4	85	17:23:25	-6	104	17:21:33	-3	123	17:23:01	-4
48	17:24:16	-9	67	17:23:43	-3	86	17:23:55	-4	105	17:20:37	-3	124	17:22:55	-2
49	17:22:49	-4	68	17:24:08	-4	87	17:22:20	-3	106	17:23:18	-2	125	17:21:01	-3
50	17:22:49	-4	69	17:20:56	-2	88	17:22:22	-3	107	17:20:25	-2	126	17:21:26	7
51	17:21:37	-4	70	17:24:47	-4	89	17:21:57	-3	108	17:20:30	-7	127	17:23:18	-7
52	17:21:37	-2	71	17:21:15	3	90	17:21:05	-7	109	17:21:08	-2	128	17:23:50	3
53	17:23:07	-13	72	17:20:24	-4	91	17:22:55	-4	110	17:20:30	-8	129	17:23:18	-6
54	17:23:07	-5	73	17:23:50	-8	92	17:20:27	-18	111	17:22:49	-3	130	17:23:25	-8
												131	17:23:36	-5
												132	17:21:02	-5
												133	17:23:25	-5
												134	17:22:27	-12
												135	17:21:49	-4
												136	17:21:14	-3
												137	17:22:41	-2
												138	17:22:01	-4
												139	17:21:21	-2
												140	17:20:49	-4
												141	17:22:33	-4
												142	17:21:11	6
												143	17:20:04	-3
												144	17:21:15	-3
												145	17:21:29	-4
												146	17:20:11	-2
												147	17:21:49	-8
												148	17:21:49	-5
												149	17:24:35	-4

Figure 7: Location, time and power of lightning strokes in green rectangle in Figure 6. Legend same as Figure 2

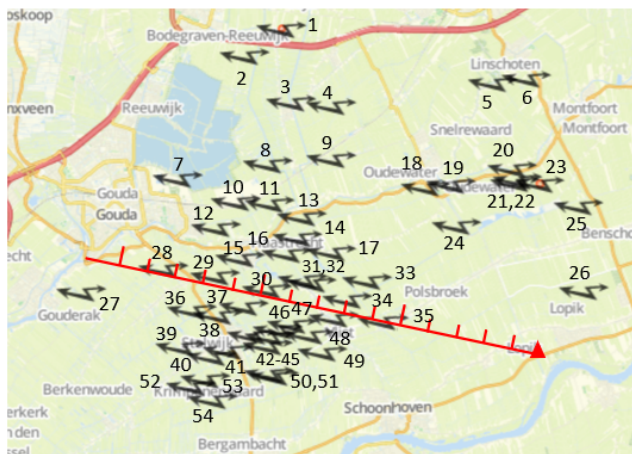
2021-06-18 17:30 UTC



	UTC	kA	UTC	kA	UTC	kA		
1	17:27:39	-6	19	17:27:45	7	37	17:28:23	-3
2	17:28:33	-3	20	17:28:00	-4	38	17:27:02	-10
3	17:26:58	-8	21	17:25:05	-4	39	17:28:53	-12
4	17:26:24	-4	22	17:27:12	3	40	17:27:02	-4
5	17:27:39	-12	23	17:29:26	-2	41	17:27:53	-7
6	17:26:57	-5	24	17:29:26	-4	42	17:27:53	-8
7	17:26:43	2	25	17:25:28	-2	43	17:27:53	-3
8	17:25:28	-8	26	17:29:41	-2	44	17:25:31	-5
9	17:25:11	-5	27	17:27:53	-3	45	17:25:05	-4
10	17:25:38	-3	28	17:26:52	-2	46	17:25:05	-5
11	17:29:36	-3	29	17:26:00	-5	47	17:25:05	-4
12	17:28:06	-2	30	17:26:00	-3	48	17:27:45	-3
13	17:26:58	-4	31	17:27:53	5	49	17:25:31	-2
14	17:25:21	-4	32	17:29:57	-2	50	17:25:05	-6
15	17:28:44	4	33	17:25:35	-3	51	17:27:45	-3
16	17:27:53	-3	34	17:29:57	-4	52	17:25:11	-3
17	17:26:57	-2	35	17:29:57	-2	53	17:25:31	2
18	17:25:38	-3	36	17:29:41	-3			

Figure 8: Location, time and power of lightning strokes from 2021-06-18 17:25 to 17:30 UTC. Legend same as Figure 2. Cloud-to-ground lightning in bold

2021-06-18 17:35 UTC



	UTC	kA	UTC	kA	UTC	kA		
1	17:30:08	6	19	17:32:01	-5	37	17:31:48	-3
2	17:31:36	-3	20	17:32:55	-4	38	17:31:23	-3
3	17:30:07	2	21	17:32:55	-12	39	17:31:48	-4
4	17:31:36	-3	22	17:32:55	-4	40	17:31:04	-3
5	17:31:36	-3	23	17:31:23	5	41	17:30:08	9
6	17:31:36	-3	24	17:34:15	-3	42	17:32:02	-3
7	17:30:19	-2	25	17:32:02	3	43	17:31:48	-8
8	17:30:19	-3	26	17:32:50	-3	44	17:31:04	-7
9	17:30:19	-4	27	17:31:10	3	45	17:31:23	-3
10	17:31:04	3	28	17:34:15	-3	46	17:31:23	-4
11	17:32:55	-2	29	17:33:48	-2	47	17:32:50	-4
12	17:31:23	-4	30	17:34:07	-3	48	17:32:17	-4
13	17:32:01	-5	31	17:33:23	3	49	17:30:39	-6
14	17:34:15	-3	32	17:32:43	-6	50	17:30:45	-3
15	17:34:15	-3	33	17:31:23	-6	51	17:31:23	-3
16	17:33:48	-3	34	17:32:43	-8	52	17:30:25	-3
17	17:34:15	-4	35	17:30:50	-3	53	17:30:07	-3
18	17:32:01	-3	36	17:30:03	2	54	17:30:08	4

Figure 9: Location, time and power of lightning strokes from 2021-06-18 17:30 to 17:35 UTC. Legend same as Figure 2

C. Other notable cases

Some interesting cases were not included in the main text of the report since they are not fully understood yet. They are described here to prompt further investigations.

C.1. Second cloud

From 16:43 to 16:48 UTC, negative Z_{DR} and K_{DP} are observed in the cloud. Figure 10(f-h) show the vertical profiles of Z_{hh} , SL_{DR} and ρ_{hv} at 16:43:51 UTC. SL_{DR} increases with height and ρ_{hv} decreases with height. However, one should be cautious when interpreting the values near 4000 m and above since the SNR is low. Figure 10(b) shows the spectrogram of Z_{DR} at this instant. The left part of the spectrum shows large positive Z_{DR} , while the right part of the spectrum shows negative Z_{DR} , with small positive Z_{DR} at the right edge. Positive Z_{DR} on the right edge may also be present above 3900 m, but it is not shown in the spectrogram because it may be filtered out by the 10 dB SNR threshold. In the graph of $s\Psi_{DP}$ in Figure 10(e), the Rayleigh plateau occurs at Doppler velocity larger than 4 m s^{-1} , and the differential phase shift increases on the left of the spectrum, thus the Mie scattering regime is the part of the spectrum with Doppler velocity smaller than 4 m s^{-1} , corresponding to particle radius of about 1.5 mm.

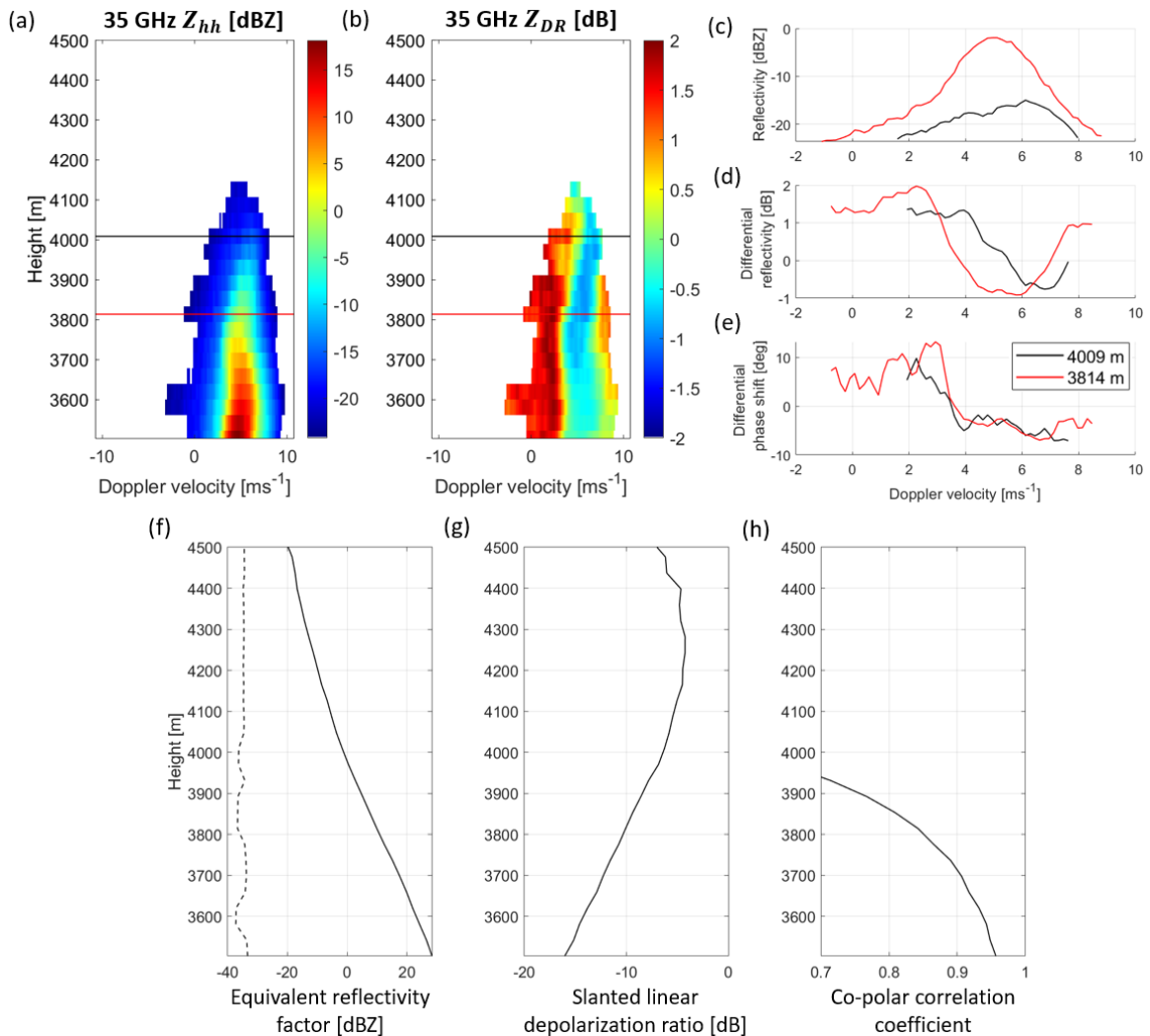


Figure 10: 2021-06-18 16:43:51 UTC where strong negative Z_{DR} is observed (a-b) Spectrograms of reflectivity and differential reflectivity (c-e) spectra of reflectivity, Z_{DR} and Ψ_{DP} at 3814 m and 4009 m (f-h) profiles of Z_{hh} , SL_{DR} and ρ_{hv}

If negative Z_{DR} values correspond to the vertical alignment of small particles and positive values on the left part of the spectrum indicates large particles not aligned by the electric field, it would be difficult to explain why the smallest particles on the right edge of the spectrum has positive Z_{DR} , which suggests that they are not vertically aligned. One possibility is that differential attenuation due to liquid water at the bottom of the cloud has introduced a negative bias to the Z_{DR} values. It could be the case that the whole Z_{DR} spectrum is in fact positive, having small particles with small positive Z_{DR} , medium-sized particles with more spherical shape with lower Z_{DR} , and large oblate particles with large positive Z_{DR} .

To estimate the differential attenuation due to liquid water, simulation is carried out with different drop size distributions using a gamma distribution defined as [35]

$$N(D) = N_w f(\mu) \left(\frac{D}{D_0} \right)^\mu \exp \left[(-3.67 + \mu) \frac{D}{D_0} \right] \quad (1)$$

with

$$f(\mu) = \frac{6}{(3.67)^4} \frac{(3.67 + \mu)^{\mu+4}}{\Gamma(\mu + 4)}, \quad (2)$$

where $N(D)$ is the drop size distribution in $\text{mm}^{-1}\text{m}^{-3}$, D is the drop diameter in mm, N_w is the intercept parameter in $\text{mm}^{-1}\text{m}^{-3}$, D_0 is the median volume diameter in mm, μ is the shape parameter and Γ is the gamma function. To represent typical convective precipitation in mid-latitudes, combinations of N_w , μ and D_0 are taken from the following ranges:

$$\begin{aligned} N_w &= 10^k \text{ where } 2.75 \leq k \leq 4.5 && [\text{mm}^{-1}\text{m}^{-3}] \\ -2 &\leq \mu \leq 2.5 \\ 1.2 &\leq D_0 \leq 2.5 && [\text{mm}] \end{aligned}$$

Figure 11 shows the simulated one-way differential attenuation for rainfall rate below 20 mm/h at 35 GHz at 45° elevation at 20°C. In the second cloud, the rainfall rate is less than 2 mm/h, which corresponds to 1-way differential attenuation of less than 0.05 dB/km. The 0°C layer is at about 4 km, so the two-way attenuation should be less than $0.05 \times 4 \times 2 = 0.4$ dB. If the measured differential reflectivity is corrected by adding 0.4 dB, the negative part of the spectrum in Figure 10(d) still retains significant negative value of around 0.5 dB.

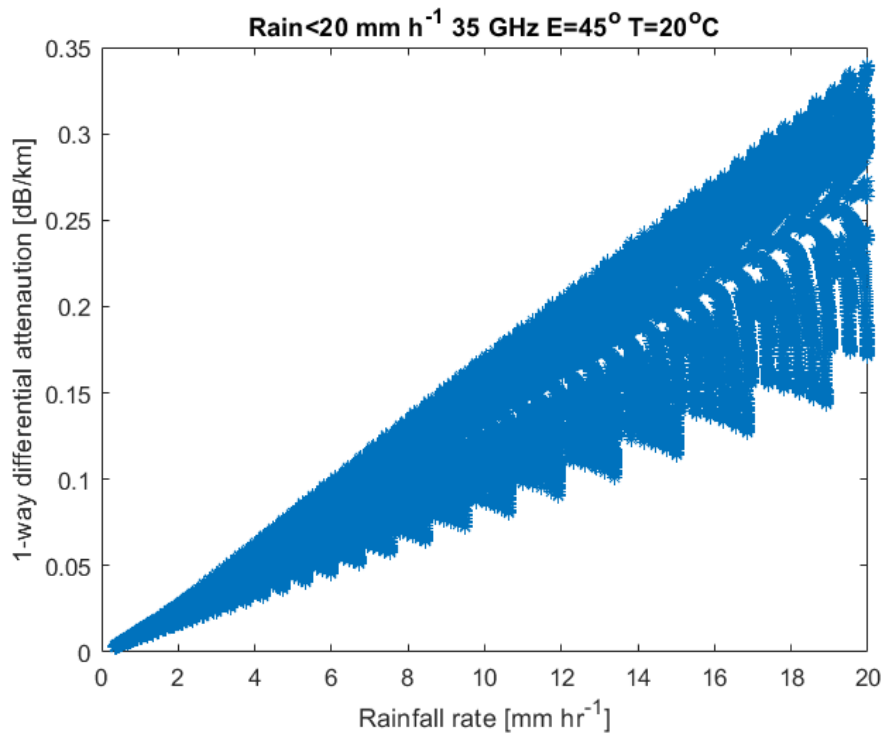


Figure 11: One-way differential attenuation as a function of rainfall rate at 35 GHz at 45° elevation at 20°C for drop size distributions of convective precipitation in mid-latitudes

One possible explanation for this negative Z_{DR} could be the presence of conical graupel, while the positive Z_{DR} at the right edge of the spectrum corresponds to small oblate particles. It is worth noting, however, that the minimum Z_{DR} of conical graupel with axis ratio of 1.05 is about -0.12 dB, which is less negative than -0.5 dB. The more negative Z_{DR} observed may be due to different cone angles of the conical graupel.